



THESIS  
3  
2001



This is to certify that the

dissertation entitled

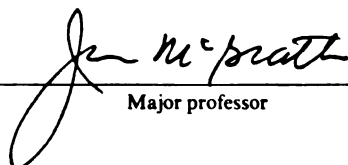
EXPERIMENTAL STUDY OF HEAT TRANSFER AND PHASE CHANGE CONDENSATION IN A  
DEVELOPING, TWO-DIMENSIONAL WALL JET FLOW FIELD WITH AN ISOTHERMAL  
BOUNDARY CONDITION

presented by

Paul Bryan Hoke

has been accepted towards fulfillment  
of the requirements for

Ph.D. degree in Mechanical Engineering

  
Major professor

Date 7/25/01



PLACE IN RETURN BOX to remove this checkout from your record.  
 TO AVOID FINES return on or before date due.  
 MAY BE RECALLED with earlier due date if requested.

DATE DUE	DATE DUE	DATE DUE
MAY 05 2003		
OCT 26 2003		
APR 17 2004		
SEP 09 2004		



**EXPERIMENTAL STUDY OF HEAT TRANSFER AND PHASE CHANGE CONDENSATION  
IN A DEVELOPING, TWO-DIMENSIONAL WALL JET FLOW FIELD  
WITH AN ISOTHERMAL BOUNDARY CONDITION**

**By**

**Paul Bryan Hoke**

**A DISSERTATION**

**Submitted to  
Michigan State University  
in partial fulfillment of the requirements  
for the degree of**

**DOCTOR OF PHILOSOPHY**

**Department of Mechanical Engineering**

**2001**

Exp  
Deve

means

defros

was u

of the

conde

a two

profile

with n

comp

at the

much

predi

10%

## **ABSTRACT**

### **Experimental Study of Heat Transfer and Phase Change Condensation in a Developing, Two-dimensional Wall Jet Flow Field with an Isothermal Boundary Condition**

**By**

**Paul Bryan Hoke**

**Benchmark data were obtained in a developing wall jet flow field as a means to validate computational models utilized for automotive defroster/demister flow design. A non-impinging, two-dimensional wall jet flow was utilized due to the relatively simplicity of the flow geometry and the similarity of the boundary conditions to the actual defroster flow field.**

**Isothermal, non-isothermal, non-condensing and non-isothermal, condensing flow regimes were measured and compared to results obtained from a two-dimensional computational model. The experimental, mean velocity profiles at streamwise locations greater than 7.62 slot widths downstream agreed with results in the literature to within 1% [Launder and Rodi, 1981]. The computational models tended to over-predict velocity and temperature gradients at the wall surface and over-predicted growth of the inner shear region by as much as 60% while under-predicting the jet-spreading rate. The model predictions of the mean velocity and the streamwise-normal stress agree within 10% and 20% respectively throughout the developing region investigated here.**

utilizing

measur

accura

techniq

that is

provide

other m

conden

to 8-12

thickne

with a

target

ensem

calibra

was ut

the wa

coeffic

sensiti

coeffici

measur

differen



**A new technique was developed to measure small aliquots of water utilizing headspace gas chromatography with a flame ionization detector. This measurement technique provided measurements of water from 0 to 3 mg with an accuracy of  $\pm 0.038$  mg at a 95% confidence level for the regression model. This technique is more robust and exceeds the capability of gravimetric equipment that is readily available. The development of this technique was essential to provide an accurate measure of condensate in the required range and to meet other requirements, such as specimen isolation, of the experimental program.**

**A novel optical technique was developed to measure transient, local condensate thickness on reflective surfaces. Surface reflectance measurements to 8-12  $\mu\text{m}$  wavelengths (infrared) were correlated with  $\text{H}_2\text{O}$  condensate thickness present on the surface. This technique proved to be highly sensitive with a dynamic range from 0 to 5  $\mu\text{m}$ . Measurement accuracy depends on the target utilized. Accuracy of  $\pm 0.17$   $\mu\text{m}$  at a 95% confidence level was attained for ensemble surface calibrations (multiple target average). It appears that a single calibrated target would provide greater measurement accuracy. This technique was utilized to provide measurements of transient condensation development in the wall jet flow and estimates of the local, instantaneous mass transfer coefficient were calculated. Results indicated that the technique is an extremely sensitive condensate thickness indicator but that uncertainty in the mass transfer coefficient can be of the same order of magnitude or larger than the measurement due to the potential error in determining the concentration difference in the flow field.**

**Copyright by  
Paul Bryan Hoke  
2001**

**To Carol, Madeleine, and Isabelle**

and s

good

helpin

has hi

have l

his tim

often n

perspe

commi

time to

Basha

make t

has be

Locont

possibi

technic

and ma

F

support

## **ACKNOWLEDGMENTS**

**I could never have accomplished this body of work without the assistance and support of my family, mentors, friends and colleagues. I promised my very good friend Alptekin Aksan that he would be first in this list once when he was helping me out of a jam and indeed his assistance has been beyond measure, as has his friendship. Scott Morris was also invaluable as a resource and a friend. I have learned more in discussions with Scott than I ever did in class.**

**Dr. John McGrath, my advisor and mentor, gave me support, advice and his time. I thank him for that; he was always available. Dr. Craig Somerton was often my moral support and my listening ear. He often helped me keep perspective during this process. I'd also like to thank the other members of my committee, Dr. Ahmed Naguib and Dr. Dennis Gilliland. They always took the time to answer my questions and share their experience and knowledge. Dr. Bashar AbdulNour had the confidence in me to supply us with the funding to make this project possible. Dr. AbdulNour is a wonderful advocate and his input has been invaluable.**

**Others here at MSU offered assistance, input and advice. Dr. Paul Loconto and Yan Pan made the analytical chemistry portions of this thesis possible. Arno Kinnen was a joy to work with, I will always remember our technical discussions with a smile. Doug Neal, Damien Fron, Molly Desjardins and many, many others have made this a wonderful place to work and learn.**

**Finally, I'd like to thank my family, immediate and extended. Their undying support kept me going and gave me confidence in myself.**

## TABLE OF CONTENTS

List of Tables .....	ix
List of Figures .....	x
Nomenclature .....	xvii
Introduction .....	1
Chapter 1. Statement of problem and review of literature.....	4
1.1 STATEMENT OF PROBLEM .....	4
1.2 REVIEW OF LITERATURE .....	9
Chapter 2. Facility development and characterization .....	17
2.1 FACILITY DESCRIPTION.....	19
2.2 EXPERIMENTAL CAPABILITIES.....	23
2.3 DATA ACQUISITION AND MOTION CONTROL .....	25
2.4 MEASUREMENT PARAMETERS AND CONTROL .....	26
2.4.1 PRESSURE MEASUREMENT .....	26
2.4.2 VELOCITY MEASUREMENTS.....	27
2.4.3 TEMPERATURE MEASUREMENT .....	30
2.4.4 HUMIDITY MEASUREMENT AND CONTROL .....	31
2.4.5 CONDENSATION VISUALIZATION.....	32
2.5 THERMALLY ACTIVE TEST SECTION .....	33
2.6 CALIBRATION AND CHARACTERIZATION EXPERIMENTS .....	36
2.6.1 TEST CONTRACTION MEASUREMENTS.....	36
2.6.2 SPATIAL FLOW UNIFORMITY MEASUREMENTS.....	38
2.6.3 TEMPORAL STABILITY OF THE FMTF TEMPERATURE AND HUMIDITY .....	41
Chapter 3. Isothermal flow .....	44
3.1 EXPERIMENTAL RESULTS.....	45
3.2 COMPUTED RESULTS AND COMPARISON TO EXPERIMENTAL DATA.....	52
3.3 DISCUSSION OF RESULTS .....	56
Chapter 4. Steady state, non-isothermal, non-condensing flow.....	60
4.1 EXPERIMENTAL METHODS.....	60
4.2 EXPERIMENTAL UNCERTAINTY.....	63
4.3 EXPERIMENTAL RESULTS OF THE NON-ISOTHERMAL, NON-CONDENSING EXPERIMENTAL REGIME .....	65
4.3.1 NON-ISOTHERMAL VELOCITY PROFILES.....	68
4.3.2 NON-ISOTHERMAL TEMPERATURE PROFILES .....	72
4.4 SUMMARY OF EXPERIMENTAL RESULTS.....	77
4.5 COMPARISON OF EXPERIMENTAL DATA TO CFD RESULTS .....	79



Ch  
5.1  
5.2

Ch  
the  
6.1  
6.1  
6.1  
The  
6.1

6.2  
6.2

Cha  
in t  
7.1  
7.2  
7.3  
7.4  
7.5  
7.6  
REF

Cha  
8.1

App

App  
for F

App

App  
with

App  
obta.

App  
with t

App

<b>Chapter 5. Steady state, non-isothermal, condensing flow .....</b>	<b>83</b>
<b>5.1 TEMPERATURE AND VELOCITY MEASUREMENTS.....</b>	<b>83</b>
<b>5.2 STEADY STATE MASS TRANSFER MEASUREMENTS.....</b>	<b>88</b>
 <b>Chapter 6. Optical, transient mass transfer measurement utilizing infrared thermography.....</b>	 <b>100</b>
<b>6.1 EXPERIMENTAL METHODS .....</b>	<b>106</b>
<b>6.1.1 MEASUREMENT OF TRACE CONDENSATE.....</b>	<b>107</b>
<b>6.1.2 CALIBRATION OF THE SURFACE REFLECTIVITY AS A FUNCTION OF CONDENSATE THICKNESS .....</b>	<b>116</b>
<b>6.1.3 EFFECT OF DISTANCE AND ANGLE ON THE IR-H<sub>2</sub>O OPTICAL CALIBRATION .....</b>	<b>123</b>
 <b>6.2. VALIDATION OF THE OPTICAL MEASUREMENT CALIBRATION WITH A NON-HOMOGENEOUS CONDENSATE FIELD.. .....</b>	 <b>124</b>
<b>6.2.1. NON-HOMOGENEOUS EXPERIMENTAL PROCEDURE AND RESULTS.....</b>	<b>130</b>
 <b>Chapter 7. Optical, transient mass transfer measurements in the developing wall jet.....</b>	 <b>135</b>
<b>7.1 INTRODUCTION.....</b>	<b>135</b>
<b>7.2 EXPERIMENTAL CONFIGURATION .....</b>	<b>135</b>
<b>7.3 TRANSIENT OPTICAL DATA .....</b>	<b>138</b>
<b>7.4 RESULTS OF THE TRANSIENT CONDENSATION EXPERIMENTS IN THE FMTF .....</b>	<b>142</b>
<b>7.5 SHERWOOD NUMBER DEPENDENCE ON JET REYNOLDS NUMBER.....</b>	<b>152</b>
<b>7.6 UNCERTAINTY ESTIMATES FOR THE OPTICAL INFRARED REFLECTANCE TECHNIQUE.....</b>	<b>154</b>
 <b>Chapter 8. Summary.....</b>	 <b>159</b>
<b>8.1 FUTURE WORK.....</b>	<b>163</b>
 <b>Appendix A. Cold wire calibration device and methodology.....</b>	 <b>168</b>
 <b>Appendix B. Equipment and Settings Utilized for Reflectance Calibration Experiments .....</b>	 <b>175</b>
 <b>Appendix C. Control settings utilized for GC-FID with Automated Sampler .....</b>	 <b>177</b>
 <b>Appendix D. Comparison of the heat transfer associated with the phase change event compared to the sensible heat transfer .....</b>	 <b>179</b>
 <b>Appendix E. Catalog of condensation and mass transfer measurements obtained with the optical infrared reflectance technique .....</b>	 <b>183</b>
 <b>Appendix F. Error analysis in the Sherwood number determined with the optical infrared reflectance technique .....</b>	 <b>195</b>
 <b>Appendix G. Publications related to this work.....</b>	 <b>205</b>

LIS

Cha

Tab

FMT

Chap

Tabl

at the

Tabl

at the

Chap

Table

in the

Table

Appen

Table

docun

## **LIST OF TABLES**

### **Chapter 2**

<b>Table 2.1. Experimental parameter control and measurement capabilities of the FMTF .....</b>	<b>24</b>
---	-----------

### **Chapter 5**

<b>Table 5.1. Comparison of experimental and computed velocity gradients at the thermally active surface .....</b>	<b>98</b>
<b>Table 5.2. Comparison of experimental and computed temperature gradients at the thermally active surface .....</b>	<b>98</b>

### **Chapter 7**

<b>Table 7.1. Variables and uncertainties utilized to calculate the uncertainty in the Sherwood number .....</b>	<b>155</b>
<b>Table 7.2. Contribution of the experimental variables to the total uncertainty ..</b>	<b>157</b>

### **Appendix F**

<b>Table F.1. Mathematica<sup>®</sup> variable names and corresponding variables in document .....</b>	<b>204</b>
--	------------

Cha

Figur

in air

Chap

Figur

Figur

Figur

Figur

Figur

Figur

(Flow

Figur

Figur

Figur

Figur

test s

Figur

meas

Figur

Figur

Figur

Chapt

Figur

wall je

Figur

Figur

Figur

## LIST OF FIGURES

### Chapter 1

<b>Figure 1.1. Ratio of latent heat transfer to sensible heat transfer for water vapor in air .....</b>	<b>8</b>
---	----------

### Chapter 2

<b>Figure 2.1. Schematic of the wall jet flow field in the FMTF. ....</b>	<b>18</b>
<b>Figure 2.2. The Ford MSU Test Facility (FMTF).....</b>	<b>19</b>
<b>Figure 2.3. Photograph of the Ford MSU Test Facility. ....</b>	<b>20</b>
<b>Figure 2.4. Thermally active test section – aluminum heat exchanger.....</b>	<b>22</b>
<b>Figure 2.5. Schematic of the data acquisition and motion control systems. ....</b>	<b>25</b>
<b>Figure 2.6. Hot-wire configuration for two wire probe technique; top view; (Flow direction in x-direction, into the page). ....</b>	<b>28</b>
<b>Figure 2.7. Temperature reference and thermocouple calibration equipment. ..</b>	<b>31</b>
<b>Figure 2.8. Interior flow pattern of the thermally active test section. ....</b>	<b>34</b>
<b>Figure 2.9. Bypass loop schematic for transient thermal tests .....</b>	<b>35</b>
<b>Figure 2.10. Transient temperature history of the thermally active test section.....</b>	<b>35</b>
<b>Figure 2.11. Comparison of test contraction velocity (from pressure tap measurements) and Pitot tube measured velocity .....</b>	<b>38</b>
<b>Figure 2.12. Z-direction (transverse) velocity profile; <math>y/w = 0.5</math> .....</b>	<b>40</b>
<b>Figure 2.13. Jet temperature and humidity uniformity study (<math>w = 2</math> cm). ....</b>	<b>41</b>
<b>Figure 2.14. Typical transient response data for the wall jet flow in the FMTF. ..</b>	<b>43</b>

### Chapter 3

<b>Figure 3.1. Definitions of features and zones in the two-dimensional wall jet flow.....</b>	<b>45</b>
<b>Figure 3.2. Non-dimensional velocity profile at <math>x/w = 0.0</math>. ....</b>	<b>47</b>
<b>Figure 3.3. Non-dimensional velocity profile at <math>x/w = 1.59</math>. ....</b>	<b>48</b>
<b>Figure 3.4. Non-dimensional velocity profile at <math>x/w = 3.18</math>. ....</b>	<b>48</b>



F  
F  
F  
F  
F  
R  
Fi  
at  
Fi  
at  
Fig  
Fig  
to l

Cha  
Fig  
Fig  
con  
Fig  
coc  
Fig  
Fig  
Fig  
Fig  
Fig  
Fig  
Fig  
Fig  
Fig  
at x

<b>Figure 3.5. Non-dimensional velocity profile at <math>x/w = 4.45</math>.</b>	<b>49</b>
<b>Figure 3.6. Non-dimensional velocity profile at <math>x/w = 7.62</math></b>	<b>49</b>
<b>Figure 3.7. Non-dimensional velocity profile at <math>x/w = 10.8</math></b>	<b>50</b>
<b>Figure 3.8. Comparison of experimental data to results from the literature.</b>	<b>51</b>
<b>Figure 3.9. Computed velocity results for the wall jet flow field.</b>	
<b>Reynolds stress model utilized</b>	<b>53</b>
<b>Figure 3.10. Comparison of experimental and computed velocity results at <math>x/w = 0.0</math></b>	<b>54</b>
<b>Figure 3.11. Comparison of experimental and computed velocity results at <math>x/w = 10.8</math>.</b>	<b>54</b>
<b>Figure 3.12. Comparison of jet spreading rates (location of <math>\delta_2</math>)</b>	<b>55</b>
<b>Figure 3.13. Boundary layer profiles at <math>x/w = 0.0</math> compared to the Blasius laminar profile</b>	<b>56</b>
 <b>Chapter 4</b>	
<b>Figure 4.1. Schematic of the hot-wire/cold-wire dual probe sensing head.</b>	<b>63</b>
<b>Figure 4.2. Comparison of velocity profiles in the non-isothermal, non-condensing and isothermal experimental regimes; <math>x/w = 10.8</math>.</b>	<b>66</b>
<b>Figure 4.3. Comparison of the self preserving momentum profile in inner coordinates to data from Wygnanski et al. [1992]; <math>x/w = 10.8</math>.</b>	<b>67</b>
<b>Figure 4.4. Velocity profile at <math>x/w = 0.0</math>; non-isothermal; <math>T_s = 4^\circ\text{C}</math>; <math>n = 1</math>.</b>	<b>69</b>
<b>Figure 4.5. Velocity profile at <math>x/w = 1.59</math>; non-isothermal; <math>T_s = 4^\circ\text{C}</math>; <math>n = 2</math>.</b>	<b>70</b>
<b>Figure 4.6. Velocity profile at <math>x/w = 4.45</math>; non-isothermal; <math>T_s = 4^\circ\text{C}</math>; <math>n = 1</math></b>	<b>70</b>
<b>Figure 4.7. Velocity profile at <math>x/w = 7.62</math>; non-isothermal; <math>T_s = 4^\circ\text{C}</math>; <math>n = 4</math></b>	<b>71</b>
<b>Figure 4.8. Velocity profile at <math>x/w = 10.8</math>; non-isothermal; <math>T_s = 4^\circ\text{C}</math>; <math>n = 3</math>.</b>	<b>71</b>
<b>Figure 4.9. Non-dimensional temperature profile at <math>x/w = 1.59</math>; <math>T_s = 4^\circ\text{C}</math>.</b>	<b>75</b>
<b>Figure 4.10. Non-dimensional temperature profile at <math>x/w = 4.45</math>; <math>T_s = 4^\circ\text{C}</math>.</b>	<b>75</b>
<b>Figure 4.11. Temperature profile at <math>x/w = 7.62</math>; <math>T_s = 4^\circ\text{C}</math></b>	<b>76</b>
<b>Figure 4.12. Temperature profile at <math>x/w = 10.8</math>; <math>T_s = 4^\circ\text{C}</math>.</b>	<b>76</b>
<b>Figure 4.13. Comparison of the experimental and computed temperature profiles at <math>x/w = 1.59</math>; <math>T_s = 4^\circ\text{C}</math></b>	<b>80</b>

Figur

at  $x/v$

Figur

at  $x/v$

Chap

Figur

and is

Figur

conde

Figur

Figur

conde

Figur

consta

Figur

exper

Chap

Figur

Figur

Figur

section

Figur

calibr

Figur

volum

Figur

Figur

Figur

of con

<b>Figure 4.14.</b> Comparison of the experimental and computed temperature profiles at $x/w = 4.45$ ; $T_s = 4\text{ }^{\circ}\text{C}$ .	80
<b>Figure 4.15.</b> Comparison of the experimental and computed temperature profiles at $x/w = 10.8$ ; $T_s = 4\text{ }^{\circ}\text{C}$	81

## Chapter 5

<b>Figure 5.1.</b> Comparison of velocity profiles in the non-isothermal, condensing and isothermal experimental regimes.	85
<b>Figure 5.2.</b> Comparison of temperature profiles in the condensing and non-condensing, non-isothermal experimental regimes; $T_s = 4\text{ }^{\circ}\text{C}$	86
<b>Figure 5.3.</b> Steady state condensation - collection and measurement system...	89
<b>Figure 5.4.</b> Comparison of the experimental and computed steady-state condensation results	91
<b>Figure 5.5.</b> Temperature variation on the thermally active test section for a constant temperature circulating bath temperature of $34\text{ }^{\circ}\text{C}$	94
<b>Figure 5.6.</b> Average, steady-state Sherwood number comparison between the experimental, computational, and published results	96

## Chapter 6

<b>Figure 6.1.</b> Thin film absorption model.	101
<b>Figure 6.2.</b> Thin film model results of the Inframetrics 600L sensitivity	104
<b>Figure 6.3.</b> Structure of the condensate formation on the thermally active test section	105
<b>Figure 6.4.</b> Typical chromatogram obtained during HS-C-GC-FID calibration	111
<b>Figure 6.5.</b> Typical calibration result for GC-FID system response to the volume of water added. ( $n = 11$ calibration samples)	113
<b>Figure 6.6.</b> Schematic of the IR-H <sub>2</sub> O calibration experiment	117
<b>Figure 6.7.</b> Photograph of the IR-H <sub>2</sub> O calibration experiment	118
<b>Figure 6.8.</b> Ensemble correlation of reflectance ratio to estimated thickness of condensate present	120

Fig  
pre  
Fig  
one  
Fig  
from  
Fig  
resu  
Fig  
befo  
Fig  
non-  
Figu  
the h  
each

Chap  
Figu  
Figu  
dunn  
Figu  
trans  
Figu  
test s  
Figu  
test s  
Figu  
surfa  
Figu  
and th  
exper

<b>Figure 6.9. Correlation of reflectance ratio to estimated thickness of condensate present for each aluminum target utilized .....</b>	<b>122</b>
<b>Figure 6.11. Temperature distribution in aluminum target derived from a one-dimensional fin analysis.....</b>	<b>127</b>
<b>Figure 6.12. Temperature distribution in 0.8 mm thick, aluminum target derived from a one-dimensional fin analysis.....</b>	<b>128</b>
<b>Figure 6.13. Concentration gradient distribution along the aluminum target resulting from the fin temperature distribution.....</b>	<b>129</b>
<b>Figure 6.14. Non-homogeneous concentration field on an aluminum target before and after a portion was dried with nitrogen gas .....</b>	<b>131</b>
<b>Figure 6.15. Measured thickness results on aluminum target #4 during a non-homogeneous condensation field test .....</b>	<b>132</b>
<b>Figure 6.16. Results of the non-homogeneous concentration field tests utilizing the HS-C-GC-FID technique as the reference standard. Coefficient of variation in each non-uniform image presented .....</b>	<b>133</b>

## Chapter 7

<b>Figure 7.1. Experimental setup in the Ford-MSU test facility. ....</b>	<b>136</b>
<b>Figure 7.2. Surface temperature history of the thermally active test section during a typical transient condensation experiment .....</b>	<b>137</b>
<b>Figure 7.3. Typical infrared images of the thermally active test surface during transient condensation experiment and the resulting surface reflectance.....</b>	<b>139</b>
<b>Figure 7.4. Reflectance measurements at <math>t = 0s</math> and <math>t = 69s</math> of thermally active test surface .....</b>	<b>140</b>
<b>Figure 7.5. Typical condensate thickness measurements on the thermally active test surface during transient condensation (<math>T_j = 24.1\text{ }^{\circ}\text{C}</math>, <math>\%Rh_j = 51.1</math>) .....</b>	<b>141</b>
<b>Figure 7.6. Typical temperature profile at <math>t = 59s</math> on the thermally active test surface during transient condensation (<math>T_j = 24.1\text{ }^{\circ}\text{C}</math>, <math>\%Rh_j = 51.1</math>).....</b>	<b>144</b>
<b>Figure 7.7. Typical concentration difference at <math>t = 59s</math> between the wall jet flow and the thermally active test surface during transient condensation experiment.....</b>	<b>145</b>



<b>Figure 7.8.</b> Typical Sherwood number results on the thermally active test surface during transient condensation experiment ( $T_j = 24.1\text{ }^{\circ}\text{C}$ , $\%Rh_j = 51.1$ ) .....	147
<b>Figure 7.9.</b> Compiled Sherwood number results on the thermally active test surface ( $Re_w=13300$ ).....	148
<b>Figure 7.10.</b> Comparison of experimental and published [Mabuchi and Kumada, 1972] Sherwood number results .....	149
<b>Figure 7.11.</b> Experimental Sherwood number results fitted with a fifth order curve.....	151
<b>Figure 7.12.</b> Experimental Sherwood number results as a function of the jet Reynolds number .....	153
<b>Figure 7.13.</b> Uncertainty of the experimental Sherwood number results as a function of the temperature of the thermally active wall surface ( $T_s$ ). $T_{\text{dew-point}} \sim 283\text{ K}$ .....	156
 <b>Appendix A</b>	
<b>Figure A.1.</b> Schematic of a cold-wire probe .....	168
<b>Figure A.2.</b> Schematic of the cold-wire calibration device.....	170
<b>Figure A.3.</b> Temperature conditioning section of the cold-wire calibrator.....	171
<b>Figure A.4.</b> Cold-wire calibration device.....	171
<b>Figure A.5.</b> Temperature profiles at the exit plane of the four calibration nozzles .....	172
<b>Figure A.6</b> Time-averaged mean temperature and standard deviation of the cold wire measurement as a function of time .....	173
 <b>Appendix C</b>	
<b>Figure C.1.</b> Analytical syringe and 22 mL headspace vial and crimp cap utilized for chromatography experiments .....	178
 <b>Appendix E</b>	
<b>Figure E.1.</b> Condensate thickness results for $Re_w = 6560$ test (11 June 2001. Experiment #2).....	184

Figure

(11 J.

Figure

Expe

Figure

(15 J.

Figure

(15 J.

Figure

Expe

Figure

(15 J.

Figure

#3)...

Figure

Expe

Figure

(15 J.

Figure

(15 J.

Figure

Expe

Figure

(5 Ju

Figure

(5 Ju

Figure

Expe

Figure

(20 J.

<b>Figure E.2. Temperature log for <math>Re_w = 6560</math> test</b>	
(11 June 2001. Experiment #2).....	184
<b>Figure E.3. Sherwood number results for <math>Re_w = 6560</math> test (11 June 2001.</b>	
Experiment #2).....	185
<b>Figure E.4. Condensate thickness results for <math>Re_w = 8400</math> test</b>	
(15 June 2001. Experiment #4).....	185
<b>Figure E.5. Temperature log for <math>Re_w = 8400</math> test</b>	
(15 June 2001. Experiment #4).....	186
<b>Figure E.6. Sherwood number results for <math>Re_w = 8400</math> test (15 June 2001.</b>	
Experiment #4).....	186
<b>Figure E.7. Condensate thickness results for <math>Re_w = 10200</math> test</b>	
(15 June 2001. Experiment #3).....	187
<b>Figure E.8. Temperature log for <math>Re_w = 10200</math> test (15 June 2001. Experiment</b>	
#3).....	187
<b>Figure E.9. Sherwood number results for <math>Re_w = 10200</math> test (15 June 2001.</b>	
Experiment #3).....	188
<b>Figure E.10. Condensate thickness results for <math>Re_w = 13300</math> test</b>	
(15 June 2001. Experiment #2).....	188
<b>Figure E.11. Temperature log for <math>Re_w = 13000</math> test</b>	
(15 June 2001. Experiment #2).....	189
<b>Figure E.12. Sherwood number results for <math>Re_w = 13300</math> test (15 June 2001.</b>	
Experiment #2).....	189
<b>Figure E.13. Condensate thickness results for <math>Re_w = 13300</math> test</b>	
(5 June 2001. Experiment #1).....	190
<b>Figure E.14. Temperature log for <math>Re_w = 13000</math> test</b>	
(5 June 2001. Experiment #1).....	190
<b>Figure E.15. Sherwood number results for <math>Re_w = 13300</math> test (5 June 2001.</b>	
Experiment #1).....	191
<b>Figure E.16. Condensate thickness results for <math>Re_w = 13300</math> test</b>	
(20 June 2001. Experiment #1).....	191

<b>Figure E.17. Temperature log for <math>Re_w = 13300</math> test (20 June 2001.</b>	
<b>Experiment #1).....</b>	<b>192</b>
<b>Figure E.18. Sherwood number results for <math>Re_w = 13300</math> test (20 June 2001.</b>	
<b>Experiment #1).....</b>	<b>192</b>
<b>Figure E.19. Condensate thickness results for <math>Re_w = 13300</math> test</b>	
<b>(20 June 2001. Experiment #2).....</b>	<b>193</b>
<b>Figure E.20. Temperature log for <math>Re_w = 13300</math> test (20 June 2001.</b>	
<b>Experiment #2).....</b>	<b>193</b>
<b>Figure E.21. Sherwood number results for <math>Re_w = 13300</math> test (20 June 2001.</b>	
<b>Experiment #2).....</b>	<b>194</b>

## NOMENCLATURE

A	Area ( $\text{m}^2$ )
A/D	Analog to digital conversion
D	Diffusion coefficient ( $\text{m}^2/\text{s}$ )
D/A	Digital to analog conversion
C	Concentration ( $\text{kg}/\text{m}^3$ )
CFD	Computational fluid dynamics
$c_p$	Specific heat at constant pressure ( $\text{J kg}^{-1} \text{K}^{-1}$ )
E	Voltage (V)
f	Frequency (Hz)
FID	Flame ionization detector
FMTF	Ford-MSU test facility
HS	Headspace
h	Heat transfer coefficient ( $\text{W m}^{-2} \text{K}^{-1}$ )
$h_m$	Mass transfer coefficient (m/s)
IR	Infrared
k	Thermal conductivity ( $\text{W m}^{-1} \text{K}^{-1}$ )
k- $\epsilon$	k- $\epsilon$ turbulence model
g	Gravitational acceleration ( $\text{m}/\text{s}^2$ )
$G_o$	Incident radiation ( $\text{W}/\text{m}^2$ )
GC	Gas chromatography
J	Radiosity ( $\text{W}/\text{m}^2$ )
$j''$	Mass flux ( $\text{kg m}^{-2} \text{s}^{-1}$ )
L	Latent heat ( $\text{KJ}/\text{kg}$ )
L	Jet slot length (m)
L	Thermally active test section length (m)
Le	Lewis Number ( $\alpha/D$ )
m	mass (kg)
MTBE	Methyl tert-butyl ether
n	Number of data sets
P	Pressure (kPa)
ppm	Parts per million
$q''$	Heat flux ( $\text{W}/\text{m}^2$ )
$q_m''$	Heat flux associated with mass transfer ( $\text{W}/\text{m}^2$ )
R	Gas Constant ( $\text{kJ kg}^{-1} \text{K}^{-1}$ )
$Re_x$	Reynolds Number ( $U x/\nu$ )
RSM	Reynolds stress turbulence model
$Sh_x$	Sherwood number ( $h_m x/D$ )
SNS	Streamwise normal stress ( $100 (u'^2/U_{\max}^2)$ )
St	Strouhal number ( $f \theta/U$ )
T	Temperature ( $^{\circ}\text{C}$ or K)
T	Thickness(m)
t	Time (s)
U	Streamwise velocity (m/s)

U\* .....  
u' .....  
V .....  
V .....  
W .....  
w .....  
X (or x) .....  
Ä .....  
Y (or y) .....  
y\* .....  
Z (or z) .....  
%Rh .....

# Greek

α .....  
ε .....  
Δ .....  
δ .....  
μ .....  
ρ .....  
ρ .....  
ν .....  
σ .....  
σ .....  
θ .....  
θ .....  
θ' .....  
ω .....

# SUBS

cal .....  
cw .....  
f .....  
hw .....  
j .....  
jet .....  
m .....  
max .....  
o .....  
ref .....  
s .....  
sat .....

$U^+$ .....	Shear velocity (m/s)
$u'$ .....	Root mean square streamwise velocity (m/s)
$V$ .....	Velocity normal to test surface (m/s)
$V$ .....	Velocity (m/s)
$W$ .....	Spanwise velocity (m/s)
$w$ .....	Wall jet slot width (m)
$X$ (or $x$ ) .....	Streamwise direction/location (m)
$\bar{A}$ .....	Mean value of $A$
$Y$ (or $y$ ) .....	Normal to test surface direction/location (m)
$y^+$ .....	Wall coordinates (m)
$Z$ (or $z$ ) .....	Spanwise direction/location (m)
%Rh .....	Relative humidity

### Greek

$\alpha$ .....	Absorptivity ( $m^{-1}$ )
$\epsilon$ .....	Emissivity
$\Delta$ .....	Delta (e.g. $X_{i+1} - X_i$ )
$\delta_2$ .....	Distance from test surface where $U = 0.5 U_{max}$
$\mu$ .....	True mean value
$\rho$ .....	Density ( $kg/m^3$ )
$\rho$ .....	Reflectance
$\nu$ .....	Kinematic viscosity ( $m^2/s$ )
$\sigma$ .....	Stephan Boltzmann constant ( $5.67 \times 10^{-8} W m^{-2} K^{-4}$ )
$\sigma$ .....	Standard deviation
$\theta$ .....	Non-dimensional temperature
$\theta$ .....	Momentum thickness (m)
$\theta'$ .....	root mean square Non-dimensional temperature
$\omega$ .....	Specific humidity ( $kg H_2O/kg$ air)

### SUBSCRIPTS

cal .....	Calibration
cw .....	Cold-wire
f .....	Final
hw .....	Hot-wire
j .....	Jet conditions
jet .....	Jet conditions
m .....	Mirror
max .....	Maximum
o .....	Initial ( $t=0$ )
ref .....	Reference conditions
s .....	Surface
sat .....	Saturation

<b>t</b> .....	<b>Target</b>
<b>tot</b> .....	<b>Total</b>
<b>w</b> .....	<b>Water</b>
<b>w</b> .....	<b>Wire</b>
<b>∞</b> .....	<b>Far field conditions</b>



database

of defr

Defros

minimu

govern

capab.

CFD s

before

develop

improve

A

Compar

mass tra

facility g

atmosph

tempera

occurs a

Three bo

develop

experime

## **INTRODUCTION**

**The primary objective of this investigation is to establish an experimental database to be used to enhance computational fluid dynamics (CFD) simulations of defrosting/demisting on the interior surfaces of automotive windshields. Defroster/demisting performance is a key factor in customer satisfaction and minimum performance standards have been mandated by the federal government to ensure passenger safety. To develop accurate computational capabilities, comprehensive flow and condensation investigations are necessary. CFD simulation models require experimental data for calibration and verification before they can be declared valid for the engineer's use in design and development. One of the primary goals of this effort was to contribute to the improvements of these analytical tools at Ford Motor Company.**

**A flow facility has been constructed as a joint venture between Ford Motor Company and Michigan State University to investigate the momentum, heat, and mass transfer in a developing region of a two-dimensional wall jet flow. The facility generates a wall jet flow on a thermally active test section inside a sub-atmospheric chamber. The humidity and velocity of the wall jet as well as the temperature of the thermally active test section can be controlled. Phase change occurs as the humid jet flows across the cooled thermally active test section. Three boundary layers (momentum, temperature, and water concentration) develop along the length of the test surface. These are interrogated experimentally.**

profile

non-is

regime

comput

location

jet res

tended

over-pr

model

next. T

and we

spatially

computa

transfer

this pre

tempera

A

thicknes

capable

desired t

measure

The first objective of this research is to obtain velocity and temperature profile measurements in three different experimental regimes. Isothermal flow, non-isothermal, non-condensing flow, and non-isothermal, condensing flow regimes were measured and compared to results from a two-dimensional computational model. The experimental, mean velocity profiles at streamwise locations greater than 7.62 slot widths downstream agreed to within 1% with wall jet results in the literature [Launder and Rodi, 1981]. The computational models tended to over-predict velocity and temperature gradients at the wall surface and over-predicted growth of the inner shear region by up to 60%. The computational model tended to under-predict the jet spreading rate by approximately 30%.

The mass transfer to the thermally active test section was investigated next. The steady state mass transfer to the surface was measured by collecting and weighing the condensate run off. These results provide a measure of the spatially averaged, steady state mass transfer coefficient of 0.0407 m/s. The computational model over-predicted the spatially averaged, steady state mass transfer coefficient by approximately 50%. A zonal turbulence model corrected this prediction but did not address the over estimation of the velocity and temperature gradients at the wall surface.

A novel optical technique was developed to measure condensate thickness on reflective surfaces in the final phase of the project. The technique capable of obtaining quantitative measurements of the condensation onset was desired to study the windshield fogging phenomenon. Surface reflectance measurements in the 8-12  $\mu\text{m}$  wavelength range (infrared) were correlated to

H<sub>2</sub>

pro

thi

0.1

ca

att

tra

ma

an

unc

ma

det

the

stat

con

ther

test

bee

**H<sub>2</sub>O condensate thickness present on the surface of test targets. The technique proved to be highly sensitive with a dynamic range of 0 to 5  $\mu\text{m}$  of condensate thickness. Measurement accuracy depends the target utilized. Accuracy of  $\pm 0.17 \mu\text{m}$  at a 95% confidence level was attained for ensemble surface calibrations (multiple target average). It appears that greater accuracy would be attainable with a single calibrated target. This technique was utilized to measure transient condensation development in the wall jet flow and estimates of the mass transfer coefficient were calculated. Results indicate that the technique is an extremely sensitive method to measure condensate thickness but that the uncertainty in the mass transfer coefficient can be of the same order of magnitude or larger than the measurement. This is due to the potential error in determining the concentration gradient in the flow field. The results obtained with the optical infrared reflectance technique agree with the results of the steady state mass transfer experiments. The order of magnitude of both results are consistent with the literature but the mass transfer coefficient distribution on the thermally active test surface appears to be strongly influenced by the Ford-MSU test facility.**

**Note that this thesis contains color images. Symbols or shading have been used to differentiate between results where possible.**

## **Chapter 1**

### **STATEMENT OF PROBLEM AND REVIEW OF LITERATURE**

#### **1.1 STATEMENT OF PROBLEM**

The motivation for this project developed from a model study of an automotive defroster/demister system. Experimental benchmark data in a model flow with geometrical similarity to an automotive defroster was desired. These data provide the means to calibrate and validate the computational fluid dynamics (CFD) software models utilized for defroster design. Turbulence closure models used in the CFD software, such as the  $k-\epsilon$  model, have parameters that are typically calibrated to agree with flat plate boundary layer data and/or other canonical flows. The defroster flow field differs significantly from the calibration flow fields. The model results are therefore suspect in the application flow. The intent of the research was to provide a benchmark data set in a model flow field that more closely resembles an automotive defroster/demister system. These data could then be utilized to calibrate the turbulence model or, at the very least, to offer insights on how the CFD model might differ from the actual flow field.

Examples of important technological processes combining heat, mass and momentum transfer include vehicle windscreen defrosting/defogging, heating and air conditioning, accumulation on control or flight surfaces on aircraft, refrigeration processes, boilers, and heat exchangers. Mass transfer can cause other secondary effects beyond the enhancement of the heat transfer. For

example, visibility can become a critical safety factor if phase change occurs on a windshield during vehicle operation. Similarly, control surface icing in aircraft can create a significant hazard. Defogger and defroster design is also of critical importance to customer satisfaction in automotive applications [AbdulNour, 1999]. Investigation of automotive defroster/demister performance motivated this project.

The approach adopted here was to start with the simplest case to be followed by later development of the experimental investigation into more complicated flow regimes. Initially, the isothermal flow field was studied. Thermal effects were then introduced into the flow field by lowering the temperature of the thermally active test section by circulating chilled water through its interior. Finally, mass transfer and phase change (condensation) were then incorporated into the experiment by suppressing the temperature of the thermally active test section below the dew-point temperature of the air in the flow.

The isothermal flow field data obtained provides validation for the computational fluid dynamics code and the turbulence model(s) utilized. The conjugate momentum and heat transfer problem was then investigated by creating a thermal boundary layer in the flow. The validity of using a decoupled (velocity solution independent of the temperature solution) solution scheme for the momentum and energy equations was evaluated experimentally using these data. Finally, the flow with momentum, heat and mass transfer was interrogated experimentally and the data obtained utilized for comparison and validation of the CFD models.



Heat transfer can be enhanced by an order of magnitude by the introduction of a phase change at a surface [Legay-Desesquelles and Prunet-Foch, 1986]. Thus thermal system performance and energy exchanges can be improved by orders of magnitude. It is important to note that the energy or heat transfer associated with the mass transfer, even if the total amount of mass is small, is typically greater than the sensible heat transfer. This is due to the large latent energy release or absorption required to effect the change of phase.

The following derivation demonstrates the relative importance of the energy transfer associated with mass transfer as part of the overall heat transfer in a convective condensation phenomenon. Mass transfer and heat transfer can be modeled in an analogous fashion [Bejan, 1995]. Specifically, the heat transfer and mass transfer coefficients can be related as shown in Equation 1.1 [Incorpera and DeWitt, 1990]

$$\frac{h}{h_m} = \frac{k}{D Le^n} = \rho c_p Le^{1-n}, \quad n \sim \frac{1}{3} \quad (1.1)$$

For a condensation processes consisting of water vapor in air, the ratio of  $h/h_m$  is equal to approximately 1000. If the heat fluxes associated with the sensible heat transfer and the heat transfer associated with the phase change are considered however, the contribution from the latent heat ( $L$ ) must also be accounted for. The latent heat for water vapor at 283 K is 2477 kJ/kg [Çengel and Boles, 1989]. The sensible heat flux ( $q''$ ) and the heat flux associated with the latent heat ( $q_m''$ ) are presented in Equations (1.2) and (1.3) respectively.

$$q'' = h\Delta T \quad (1.2)$$

$$q_m'' = Lh_m\Delta C \quad (1.3)$$

The latent heat transfer is a function of the concentration gradient in the flow field. The concentration gradient in the flow is a function of the temperature gradient. Thermodynamic equilibrium is assumed to exist everywhere in the flow and specifically at the chilled surface. The concentration gradient can then be written in terms of the temperature gradient utilizing the Clausius-Clapeyron equation [Çengel and Boles, 1989] if the temperature and humidity of the free stream (ambient) air and temperature of the chilled surface are known. The ratio of the latent heat transfer (Equation (1.3)) to the sensible heat transfer (Equation (1.2)) can be expressed as shown in Equation (1.4).

$$\frac{q_m''}{q''} = \frac{\frac{Lh_m P_{ref}}{h(T_j - T_s)R_w} \left[ \frac{\%Rh_j e^{\frac{L}{R_w} \left( \frac{1}{T_{ref}} - \frac{1}{T_j} \right)} \left( P_{Tot} - P_{ref} e^{\frac{L}{R_w} \left( \frac{1}{T_{ref}} - \frac{1}{T_j} \right)} \right)}{T_j \left( P_{Tot} - P_{ref} \%Rh_j e^{\frac{L}{R_w} \left( \frac{1}{T_{ref}} - \frac{1}{T_j} \right)} \right)} - \frac{e^{\frac{L}{R_w} \left( \frac{1}{T_{ref}} - \frac{1}{T_s} \right)}}{T_s} \right]}{1} \quad (1.4)$$

Equation (1.4) incorporates three assumptions: that the density of the liquid water is much greater than water vapor; the relative humidity (%Rh<sub>s</sub>) at the chilled surface is 100%; and that the water vapor/air mixture can be treated as an ideal gas. The complete derivation of Equation (1.4) is presented in Appendix D. Figure 1.1 displays the ratio of the latent heat transfer to the sensible heat transfer as a function of free stream temperature (T<sub>f</sub>) with a surface temperature of 277 K and a jet humidity (%Rh<sub>j</sub>) of 70%. These conditions are typical of the tests that were conducted and of appropriate scale for the windshield condensation problem. Note that the plot starts at the dew-point temperature for the conditions specified (283.6 K). Clearly, the heat transfer associated with the latent heat release is at least as important as the sensible heat transfer in this regime.

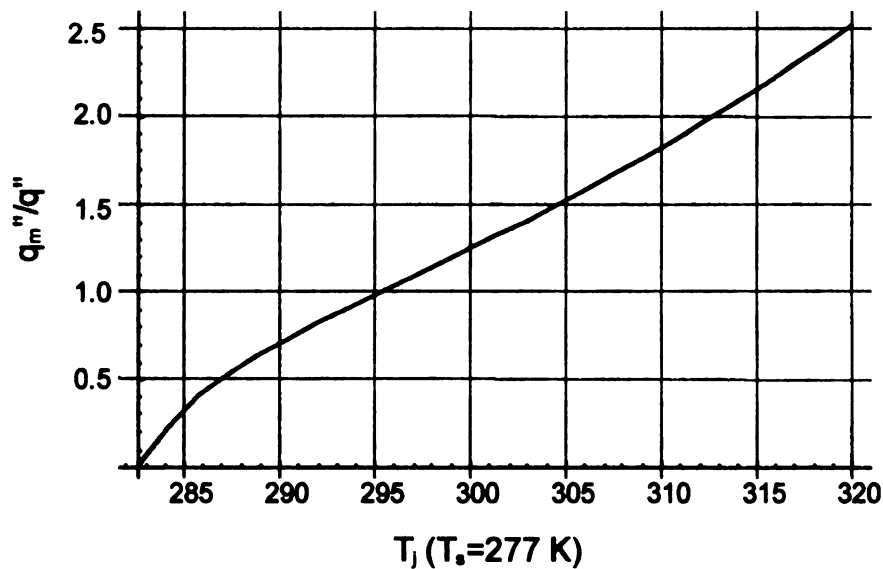


**Figure 1.1.** Ratio of latent heat transfer to sensible heat transfer for condensing water vapor in air.

Slow fog build up and flash fogging on the windscreen can occur if conditions are correct [Peters, 1972]. Both conditions can severely effect passenger safety and vehicle operation. Specifically, the initiation of condensate formation is critical to vehicular applications since small quantities of liquid can cause drastic changes in windshield clarity. If the conditions necessary for condensation can be avoided or altered in such a way as to make it more difficult for condensation to develop, the possibility of a safety hazard can be delayed, minimized or avoided altogether. Therefore understanding the onset of condensate development is critical and tools appropriate for experimental analysis are necessary.

## 1.2 REVIEW OF LITERATURE

The two-dimensional wall jet has been studied rigorously. The first experimental publication in the literature dates back to 1934 [Förthmann, 1934]. The fluid mechanics of this flow configuration were thoroughly investigated in the 1960's and 1970's by researchers such as Bradshaw and Gee [1960], Patel [1962], Tailland[1970], and many others. The developed velocity profile, the development of the turbulence signature in the flow, and the jet growth in the wall jet were well categorized in this body of literature. Recent studies of the wall jet have been conducted with new types of equipment such as laser Doppler velocimetry (LDV) and particle image velocimetry (PIV), because this flow has been so well documented previously [Eriksson et al., 1997]. The two-dimensional wall jet has been studied over flat surfaces and surfaces with a

variety of profiles, with pressure gradients (favorable and unfavorable), and with various free stream velocities and initial jet turbulence intensities. The results of these works are well summarized in *The Turbulent Wall Jet* [Launder and Rodi, 1981]. The bulk of the work reviewed by Launder and Rodi [1981] focuses on the fully developed (turbulent) wall jet with the comparison of studies performed at streamwise positions of 20-100 slot widths from the jet orifice (this eliminates effects of the jet orifice on the flow). This literature serves as a reference base and allows for comparison of the computational model at distances further downstream than were studied in the present work. Experimental evaluation of the developing region is essential to evaluating the computational model since the developing region of the flow is strongly influenced by the configuration of the facility [Mabuchi and Kumada, 1972]. The defroster/demister flow on the windshield is also a developing flow field. Finally, this flow field will then establish the environment for a study of the heat and mass transfer phenomena relevant to the motivation for this project, the automotive defroster/demister. The experimental tools currently available to measure mass transfer will be reviewed next.

Mass transfer to surfaces has been well studied as a steady state phenomenon as a means to enhance the heat transfer [Incorpera and DeWitt, 1990, Bejan, 1995]. This enhanced energy transfer associated with the phase change event is the basis of utilizing a fluid undergoing phase change in a vapor compression refrigeration cycle. However, in many vehicular applications, the process is inherently transient with respect to the boundary conditions and flow

properties, especially the flow humidity. The desire to study this phenomenon in these applications led to developing new technology to capture transient measurements of condensate thickness on the order of micrometers.

Several techniques exist for the measurement of mass transfer coefficients. In particular, sublimating surfaces such as naphthalene or benzoic acid have been used to measure the mass transfer rate from surfaces subjected to various flow fields [Goldstein, 1995, Mabuchi and Kumada, 1972, Alenezi and Abdo, 1991]. Optical measurement and detection of water and ice on surfaces have been documented by Anderson et al. [1996], Bearman et al. [1998], Utton and Sheppard [1985], and Pekdemir [1994]. Electroplating and electrode reduction measurements have also been used to obtain local measurements of mass transfer rates [Noui-Mehidi et al. 1999, DeBecker et al. 1995, Zhao and Trass, 1997, and others]. These techniques will be discussed next.

The naphthalene sublimation method is capable of obtaining accurate measurements of time averaged local mass transfer coefficients or time and spatially averaged mass transfer coefficients [Goldstein and Cho, 1995]. This technique has been widely used since the 1950's. It cannot be utilized in certain flows such as high velocity flows due to aerodynamic heating. Natural convective (or very low velocity) flows are also problematic since temperature fluctuations over long experimental runs create substantial error in the measurements [Goldstein and Cho, 1995]. It also cannot measure mass transfer coefficient changes that occur temporally such as the mass transfer coefficient evolving during a transient flow event. The technique requires a measurable

amount of naphthalene to be removed over a period of time, thus providing a temporal integration of the mass transfer coefficient at a specific location.

Goldstein and Cho [1995] estimate that the methodology produces measurements of the Sherwood number with a 7% uncertainty at a 95% confidence level ( $\pm 2\sigma$ ). The properties of the naphthalene, most notably the vapor pressure, are the largest contributors to the experimental uncertainty.

Electrode reduction methods utilized liquid chemicals as the flow medium. These techniques allow for time series information to be obtained experimentally, but do not provide local information as a function of time. This is because the electrode must have a reasonable surface area exposed to the flow to function properly. Typically, a wire is utilized as the electrode so that data are obtained along a line on the surface of interest [Debecker et al., 1995]. Thus this method is capable of providing area averaged mass transfer coefficients as a function of time or time-averaged, local mass transfer coefficient measurements. The local mass transfer as a function of time can be deduced from an iso-flux line in a two-dimensional flow field with this technique.

The method developed by Bearman et al. [1998] is capable of optical measurements of ice and liquid water thickness over a range of 500  $\mu\text{m}$  to 2000  $\mu\text{m}$ . The method utilizes images of the surface and a reference standard acquired over narrow (10 nm) wavelength bands. A ratiometric reflectance calculation in each wavelength band is used to measure water thickness on the surface. The reflectance profile in the wavelengths tested is then compared to a calibration database to obtain a thickness measurement. The authors did not

present measurements above 2000  $\mu\text{m}$  or below 500  $\mu\text{m}$ . The absorptivity of water over the wavelengths utilized (0.850  $\mu\text{m}$  to 1.050  $\mu\text{m}$ ) only varies from 0.0433  $\text{cm}^{-1}$  to 0.363  $\text{cm}^{-1}$  which would result in less than 2% absorption of the incident light at a film thickness of 500  $\mu\text{m}$ . This relatively small change in the signal appears to limit the minimum measurement range. There is an absorption peak at the 980  $\mu\text{m}$  wavelength due to the resonance of the hydrogen-oxygen bond, so it may be possible to utilize this specific wavelength to expand the capabilities of the method to a lower limit by increasing the absorbed light. The authors specify long exposure times (up to 40 seconds) and 21 images of the same condition to obtain a thickness measurement. Therefore, this technique is not capable of rapid thickness e.g. it would not be suitable for automotive fogging where  $\tau \sim 10^2$  seconds. A similar technique is described by Mao et. al. [1992] for the measurement of frost on a surface, the measurement range presented is from 1 to 4 mm with an accuracy of  $\pm 3\%$ , the authors do not specify the confidence interval of the uncertainty estimate.

An optically based, photo-evaporative technique was developed by Utton and Sheppard [1985], Davies et al. [1990, 1991], and summarized by Pekdemir and Davies [1999]. The technique utilizes a calibrated paper soaked in solvent attached to the test surface. This technique is based on measuring the reflectivity and transmissivity of a calibrated filter paper. Pekdemir [1994] calibrated the target filter paper in the same flow field that experimental measurements were obtained. Applicability of the calibration to other flows of interest was not discussed explicitly. Furthermore, the calibration values of the



target paper vary by over 100% in the same calibration experiments and can change drastically with the adhesive utilized to attach the paper to the test surface. The surface roughness of the target paper can also effect the measurement results, thus potentially adding artifacts to the data obtained. The need to attach the calibrated paper limits the size and geometry of the surface of interest that was studied [Pekdemir, 1994].

The photo-evaporative technique can only be effectively utilized in quasi-steady state flows as the technique can not measure quickly changing mass transfer rates. Solvent migration in the filter paper also limits the maximum mass transfer rates that can be studied [Pekdemir and Davies, 1999]. The calibration and experimental data show initial transient and potentially non-reproducible measurements. This is further complicated by drift in the paper calibration with time and the fact that the paper requires several experimental runs prior to calibrating to insure calibration stability. The evaporating solvent utilized for this technique is also toxic. Temperature variations between the calibration and the experimental conditions contribute to the measurement error. Pekdemir and Davies [1999] estimate the accuracy of this technique to be  $\pm 12\%$ , but do not state the confidence level of this estimate. The variation in the calibration results is overcome in the Pekdemir [1994] publication by calibrating against known results (from other experimental methods) in the actual test flow, which severely limits the potential applications of this technique to flows that have already been studied by other techniques. Utton and Sheppard [1994] also indicates that the technique would have only limited applications in natural convective flows

because the density of the solvent vapor would strongly influence the natural convective flow field.

The current state of the art indicates that an opportunity exists to develop and implement a technique capable of transient mass transfer measurements of the water condensation phenomena. The initial onset of the condensate is of critical importance to automotive defroster/demisters. Currently, defroster/demister performance is measured in an arbitrary fashion that is highly dependent on human input and error. Defroster/demister testing is performed to meet Federal Motor Vehicle Safety Standard 103 (FMVSS 103). The FMVSS 103 requires defroster testing as outlined in SAE Recommended Practice J902 [SAE, 2000]. This document defines the defrosted area as the region of the windshield that is "dry, covered with partially melted ice or wet" [SAE, 2000, p.34.19]. It further elaborates that an observer inside the vehicle should mark an outline of the defrosted region at 5 minute intervals for engineering purposes [SAE, 2000]. Clearly, this testing procedure and the data acquired are of limited use and prone to human influence. An experimental technique with PC based data acquisition would obviously provide a more objective measure of defroster/demister performance. The technique, which will be discussed next, developed as part of this project presents a potential solution to obtain quantitative data to address these issues.

The final phase of this project investigated transient mass transfer. A new optically based technique based on the scatter and absorption of infrared illumination on a reflective surface was developed. Although this technique was

not extended to automotive glass in more than a preliminary fashion, the technique was successfully applied to an aluminum test surface in the model wall jet flow. The transient measurements obtained with the method developed in this document are capable of condensate thickness measurements between 0 and 5 micrometers at a measurement rate of 0.2 Hz with the equipment utilized. The accuracy of the technique depends on whether calibrated targets are utilized for the measurements or if a similar surface technique is employed (e.g. that is, calibration is conducted on surfaces similar to the test surface). The most accurate measurement results are obtained with calibrated targets in the flow of interest; it is estimated that condensation thickness measurements can be obtained with an uncertainty of  $\pm 0.10 \mu\text{m}$  under these conditions.

## **Chapter 2**

### **FACILITY DEVELOPMENT AND CHARACTERIZATION**

**A facility was designed and constructed to provide a model flow field to obtain the benchmark data required for the project. A two-dimensional wall jet flow field with controlled velocity, wall surface temperature and inlet humidity was selected as the model flow. A schematic of a two-dimensional wall jet flow field is presented in Figure 2.1. The wall jet flow field was selected as the model flow because it has some geometric similarity to a defroster/demister system but is simple enough to avoid complications such as fan turbulence, windshield curvature or jet impingement. The design required temperature control of the wall surface to add thermal and mass transfer effects to the flow. Mass transfer is induced when the wall temperature is below the dew-point of the flow and condensation develops. The use of a wall jet flow field also allows the experimental data to be compared with other studies in the literature.**

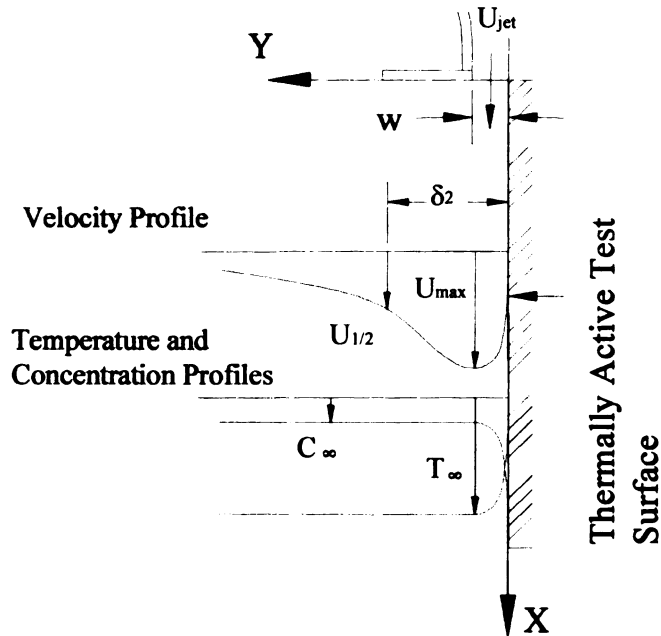


**Figure 2.1.** Schematic of the wall jet flow field in the FMTF.

The following sections outline the design of the Ford-MSU test facility (FMTF) and the functionality of the complete system. The data acquisition, motion control, and the capabilities of specific measurement transducers and devices utilized are also included. The measurement accuracy and resolution of each component are defined as well as how each measurement device contributes to the experimental project objectives. Finally, the results of the characterization experiments are presented.

## 2.1 FACILITY DESCRIPTION

A flow facility was designed and constructed to meet the goals and experimental goals of the project. The flow facility is presented in Figures 2.2 and 2.3. The system was built with a modular design so that components or configurations could be modified with minimal down time. The major system components will be described in the order that the airflow proceeds through the system.

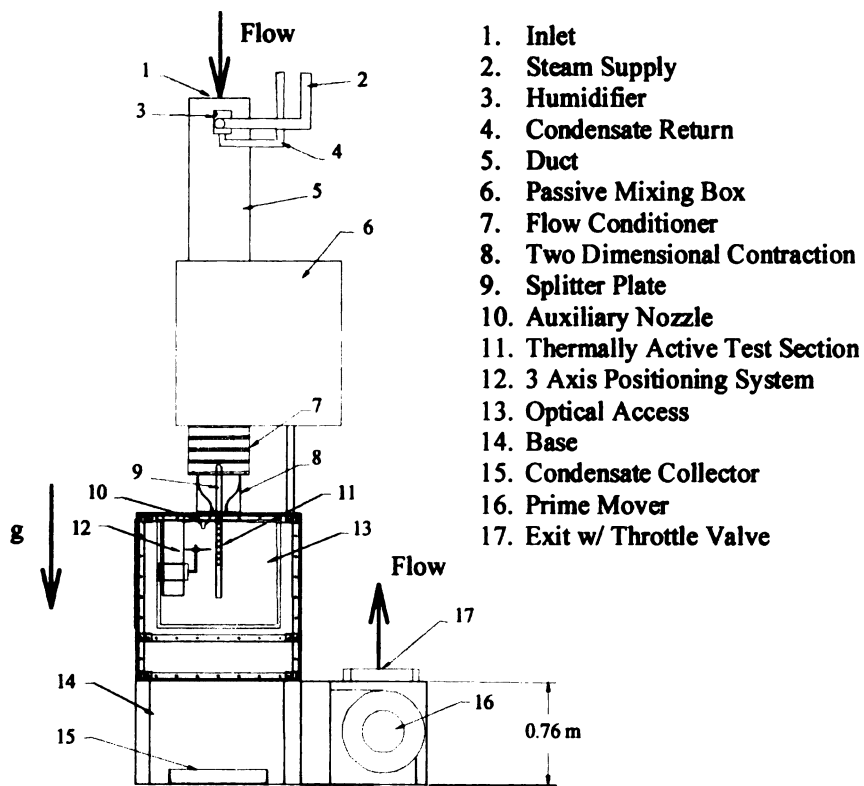


**Figure 2.2. The Ford MSU Test Facility (FMTF).**



**Figure 2.3.** Photograph of the Ford MSU Test Facility.

The steam humidification system, the passive mixing box and the associated ductwork (items 2-6 in Figure 2.2) extend above the flow conditioner and the two-dimensional contraction. This configuration allows the steam humidification to completely mix and thus insures a homogenous flow. Water droplet evaporation or removal is essential for the hot-wire/cold-wire probes to function properly as droplet impact would destroy the sensors immediately. The system is capable of adding 0.0018 kg/s of water vapor to the airflow. This is

enough to raise the humidity of the wall jet from 20% Rh to 75% Rh at a 300 CFM flow rate.

The flow exits the passive mixing box and enters the flow conditioner (item 7 in Figure 2.2). The flow conditioner consists of a one-inch-thick honeycomb structure with 0.20 inch diameter cells. The honeycomb structure removes large scale eddies from the air stream. The flow then proceeds through 3 wire screens placed 3 ½ inches apart. These screens consist of a mesh of 30 by 30 wires per square inch. This system helps break down any further turbulent motions in the flow and provides an airflow with minimal disturbances at the entrance of the two-dimensional contraction.

The two-dimensional contraction is shown as Item 8 in Figure 2.2. The two-dimensional contraction accelerates the flow and ejects it through two 2 cm wide x 35.6 cm long slots (1 on each side of the thermally active section) into the sub atmospheric test chamber. The contraction was designed to provide a jet at the exit plane with a uniform velocity profile [Morel, 1979]. The splitter plate creates a thin momentum boundary layer at the jet exit, but it also allows the thermally active test surface to be mounted in the center of the jet exit.

The thermally active test section (item 11 in Figure 2.2) is shown in Figure 2.4. The test section is essentially an aluminum heat exchanger. The surface is maintained at a constant temperature by pumping a water-glycol solution from a constant temperature circulator bath through the test section. The internal details of the test section will be discussed in section 2.5.



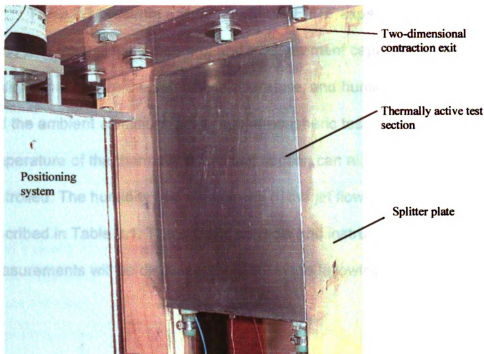


**Figure 2.4.** Thermally active test section – aluminum heat exchanger.

The positioning system and flow measurement sensors (item 12 in Figure 2.2) are also contained in the sub-atmospheric test chamber. The details of the sensors and the motion control system are presented in sections 2.3 and 2.4.

The flow exits the sub-atmospheric test chamber into the base (item 14 in Figure 2.2) of the FMTF. The base houses the prime mover for the flow system, which operates in suction mode to prevent fan turbulence from entering the sub atmospheric test chamber. The airflow rate through the FMTF system is throttled at the exit of the prime mover by a sluice valve (item 17 in Figure 2.2).

## **2.2 EXPERIMENTAL CAPABILITIES**

**Table 2.1 presents a summary of the FMTF experimental parameters along with the associated control and measurement capabilities. In general, the facility can measure the velocity, temperature, and humidity of the wall jet flow and the ambient conditions in the sub atmospheric test chamber. The surface temperature of the thermally active test section can also be measured and controlled. The humidity and the velocity of the jet flow can be controlled as described in Table 2.1. The specific controls and instrumentation used for measurements will be discussed in detail in the following sections.**

**Table 2.1. Experimental parameter control and measurement capabilities of the FMTF.**

<b><i>FMTF Variable</i></b>	<b><i>Range of Control</i></b>	<b><i>Measurement Resolution</i></b>
Humidity	Ambient to ambient + 55%Rh at 300 CFM	$\pm 1.25\%$
Velocity (Bulk Flow)	0 to 13.5 m/s	$\pm 2\%$ reading
Pressure	0 to 0.5 in-H <sub>2</sub> O (0 to 124 Pa)	0.5% full scale
Local Velocity Measurements	1 to 13.5 m/s	$\pm 2\%$
Sensor Positioning (y-axis Traverse)	120 mm of motion with 2.5 $\mu\text{m}$ steps	$< 200 \mu\text{m}$ for full range of motion
Local Temperature Measurements Thermocouple (T/C) and Cold - Wire Probe Measurements	T/C: -20 °C to 100 °C cold-wire: -20 °C to 100 °C	0.2 °C (T/C) 0.2 °C (Cold-wire)
Temperature Reference	-176 °C to 180 °C	0.01 °C (NIST traceable)
Thermally Active Test Surface (Neslab Bath Control Limits)	-20 °C to 100 °C with current working fluid	0.4 °C (stability limited)
Condensation Visualization (CCD Camera - 640 x 480 detector)	Pixel size of 391 $\mu\text{m}$ x 391 $\mu\text{m}$ (if complete test surface is viewed)	Visualization technique only
Condensation Visualization (Infrared Camera)	Pixel size of 1.91 mm x 1.91 mm (if complete test surface is viewed)	0 to 5 $\mu\text{m}$ condensate thickness - $\pm 0.17 \mu\text{m}$ @ 95% confidence level.

### 2.3 DATA ACQUISITION AND MOTION CONTROL

Data acquisition and stepper motor motion are controlled and recorded electronically. The data acquisition and motion control systems are shown schematically in Figure 2.5.

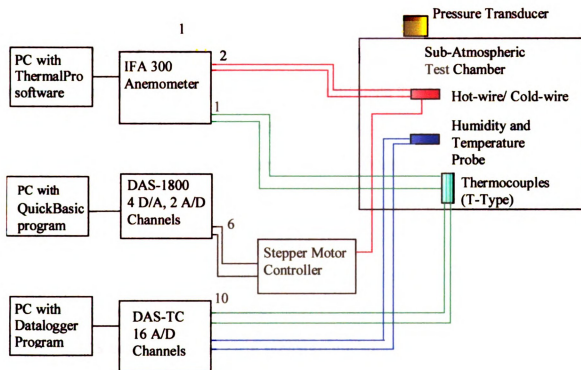


**Figure 2.5.** Schematic of the data acquisition and motion control systems.

The stepper motor positioning system is automated and controlled with software written in Microsoft QuickBasic<sup>®</sup> and implemented on a PC. The software accesses a DAS-1800ST board (Keithley Metrabyte) which provides four, 12 bit D/A output channels and 2 high speed (300 kHz) input channels to

control the stepper motor. The stepper motor (Vexta, Model Ph268M-E1.5B-C7) drives a precision screw (Specialty Motions Inc., Model KB0801-150) in order to move the sensor-positioning traverse. The stepper motor moves the traverse in the y-direction (refer to Figure 2.1) in increments of 2.5  $\mu\text{m}$ . This measurement step is smaller than the hot-wire or cold wire probe diameter (5  $\mu\text{m}$ ) and thus does not limit the spatial measurement resolution obtained.

The DAS-TC board is capable of sampling at 1 Hz per channel when multiple channels are utilized. This sampling rate limits the data inputs to relatively slow frequency sensors and thus the DAS-TC system is utilized exclusively for thermocouple and humidity sensor input.

## 2.4 MEASUREMENT PARAMETERS AND EQUIPMENT

### 2.4.1 PRESSURE MEASUREMENT

A MKS Baratron Model 225A pressure transducer is utilized to monitor a Pitot tube mounted at the exit of the two-dimensional contraction. The pressure transducer has a measurement range of 0 in-H<sub>2</sub>O and 0.5 in-H<sub>2</sub>O, and an uncertainty of 0.0025 in-H<sub>2</sub>O (0.5% of full scale).

Pressure measurements are used to calculate the inviscid core velocity of the wall jet using the Bernoulli equation (without body forces),

$$\frac{P_1}{\rho} + \frac{V_1^2}{2} = \frac{P_2}{\rho} + \frac{V_2^2}{2}. \quad (2.2)$$

$V_1$  is the inlet velocity,  $P_1$  is the inlet pressure,  $V_2$  is the velocity in the Pitot tube (which is equal to zero),  $P_2$  is the stagnation pressure, and  $\rho$  is the density of air. The velocity measured with the Pitot tube is utilized to calibrate the hot-wire sensors and to determine the wall jet velocity. A typical test is performed with a maximum inviscid core velocity of 10 m/s. The pressure transducer is capable of resolving this value to within  $\pm 0.025$  m/s.

#### **2.4.2 VELOCITY MEASUREMENTS**

Velocity measurements are performed with an IFA300 hot-wire anemometer (TSI) using the constant temperature anemometer (CTA) module. The hot-wires are constructed with 5  $\mu\text{m}$  diameter tungsten wire. These wires are heated electrically to maintain a fixed, user-defined resistance value and thus a constant operating temperature. The heat transfer from the wire is proportional to the voltage supplied and to the flow velocity. It is this phenomenon that allows the hot-wires to be calibrated and utilized as a flow velocity measurement tool.

The governing relationship between the hot-wire voltage ( $E$ ) and the velocity ( $V$ ) [Collis and Williams, 1959] is given as

$$E^2 = (A + BV^n)(T_w - T_\infty), \quad (2.4)$$

where  $A$ ,  $B$ , and  $n$  are the calibration coefficients obtained from a 3 parameter ordinary least squares curve-fit of the calibration data;  $T_w$  is the average wire temperature and  $T_\infty$  is the air temperature local to the hot wire.

However, the IFA300 system does not use a physically based equation to fit the calibration data, but rather a fourth order curve fit. Similar accuracy is attainable with either method and limited by the quality of the calibration procedure [TSI Incorporated, 1997]. A hot-wire and a cold-wire probe can be run simultaneously and the experimental configuration utilized is presented in Figure 2.6. This provides local temperature compensation for the hot wire velocity measurements in the thermal boundary layer. Details of this technique are presented in Chapter 4.

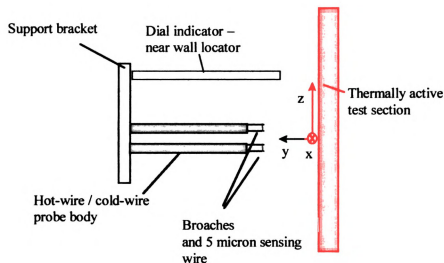


**Figure 2.6.** Hot-wire configuration for two wire probe technique; top view;  
(Flow direction in x-direction, into the page).

A well-calibrated single hot-wire is capable of achieving a velocity measurement accuracy of  $\pm 1\%$  at the turbulence intensity level present in the calibration flow in the Ford-MSU flow facility [Bruun, 1995]. This degree of

accuracy relies on calibrating the hot-wire before and after each experiment and using an average of the two calibrations to process the data. Post-calibration improves measurement accuracy by accounting for hot-wire calibration drift due to wire oxidation, slight ambient temperature or humidity changes, and/or impacts from dust particulate. The measurements presented here were made in a boundary layer near a solid surface. The hot-wire was often destroyed or damaged by contact with the surface, thus eliminating the possibility of post-calibration. Despite this, the experimental standard deviation in the isothermal velocity data was always less than 3% of the peak velocity value (or in absolute units, always less than 0.30 m/s). A single hot-wire is incapable of providing velocity field information. Hot-wires can provide high frequency velocity data, up to 300,000 Hz depending on sensor geometry, [TSI Incorporated, 1997]. Peak frequency of the velocity fluctuations in the wall jet flow were determined from the power spectrum density obtained experimentally. The power spectrum density diminished by three orders of magnitude at approximately 1500 Hz. All hot-wire data were sampled at 8 kHz or above based on these findings to insure the Nyquist criteria was met. The integral length scale of the flow was determined to be approximately 8 mm using an autocorrelation in the inner boundary layer. This clearly scales with the fluctuations in the outer shear layer and not with the inner boundary layer since the boundary layer thickness is less than 2 mm at any point on the thermally active test section. The integral length scale provides insight into the sensor spacing required for hot-wire temperature compensation.



### **2.4.3 TEMPERATURE MEASUREMENT**

Three different methods are currently utilized for temperature measurement in the FMTF. These consist of thermocouples, a thermistor, and the cold-wire probe. The thermocouples are type-T (copper-constantan) and are manufactured on site. These thermocouples have a measurement bead diameter of approximately 800  $\mu\text{m}$  and a time constant of 1 s (for typical experimental flow velocities). Special type-T thermocouples [Omega Inc.] have also been acquired with a measurement bead diameter of 60  $\mu\text{m}$  and an approximate time constant of 0.02 seconds in the flow field. The thermistor is an integral part of the General Eastern M2-Plus dew-point monitoring system utilized to monitor the wall jet temperature and humidity level.

An Omega DP-95 RTD NIST (National Institute of Standards and Technology) calibrated temperature measurement system is utilized as the temperature standard for the laboratory. The thermocouples are calibrated against this standard by placing them in an aluminum cylinder in the Neslab RTE-140 bath with the RTD probe. The calibration equipment is presented in Figure 2.7.

2.4.4 H

Humidit

General Eas

technology

system al

system o

humidity,

T

Model 90

adding O.

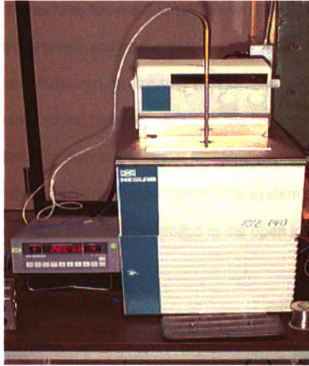


**Figure 2.7.** Temperature reference and thermocouple calibration equipment.

#### *2.4.4 HUMIDITY MEASUREMENT AND CONTROL*

Humidity is measured at the exit of the two-dimensional contraction with a General Eastern M2 Plus dew-point monitor. The system utilizes chilled mirror technology to provide a humidity measurement accurate to  $\pm 1.25\% \text{Rh}$ . The system also provides a temperature output accurate to within  $\pm 0.2^\circ \text{C}$ . The system can adjust to changes in the dew-point temperature (and thus the relative humidity) at a rate of  $1.5^\circ \text{C/s}$  [General Eastern, 1999].

The humidity of the wall jet flow can be increased with the Armstrong Model 90 steam humidifier incorporated into the facility. The system is capable of adding  $0.0018 \text{ kg/s}$  of water vapor to the airflow. This is enough to raise the

humidity from 20% Rh to 75% Rh in a 300 CFM flow. Experiments have produced 95% humidity levels and above at the wall jet exit plane at less than three-quarters of the Armstrong unit capacity with ambient conditions at 50%Rh. The slow time response of the humidity probes in the control circuit caused instability and oscillation in the control circuit provided with the unit. Therefore, the system is controlled in an open loop fashion. The system has a measured variability of less than  $\pm 2\%$  Rh when controlled in the open loop mode during the duration of a typical experiment.

#### ***2.4.5 CONDENSATION VISUALIZATION***

Both a CCD camera and an Inframetrics 600L infrared camera are available for the purpose of condensation visualization and quantification. The image information can be stored on video cassette recording equipment and time marked with a FOR-A video timer (Model VTG-33) to capture transient phenomena. The image information is processed with image processing software (ImagePro Plus v.4.1, Media Cybernetics). This software is capable of multi-functional image analysis.

Measurement resolution is determined in part by the field of view required. A CCD camera with 640 x 480 elements will have pixels that cover a  $391\ \mu\text{m} \times 391\ \mu\text{m}$  square area if the entire thermally active test surface is viewed ( $A_s = 0.0445\ \text{m}^2$ ). The pixel area scales linearly with the area of the surface viewed, i.e. if half the surface is viewed, each pixel will be half as large. Thus the field of

view and the spatial resolution are intimately related and can be adjusted by lenses or physical arrangement of the optical system.

A technique to measure transient condensate development was also desired. At the time of construction of the facility, no such method was decided upon or implemented. Details of the development and implementation of a suitable technique are included in Chapter 6.

## **2.5 THERMALLY ACTIVE TEST SECTION**

Circulation of refrigerated fluid in the interior of the thermally active test section provides temperature control of the experimental surface (Figures 2.4 and 2.8). The interior configuration of the flow channels can be seen in Figure 2.8. Previous tests using the test section in a similar flow field showed that 80% of the test surface temperature varied by less than  $0.3^{\circ}\text{C}$  at wall jet velocities as large as 10 m/s [AbdulNour et al., 1997]. The thermally active test section can be heated or cooled depending on the setting of the temperature bath. The Neslab NTE-140 temperature bath utilized is capable of supplying 500 watts of cooling at  $0^{\circ}\text{C}$  or 800 watts of heating and has a range of  $-40^{\circ}\text{C}$  to  $100^{\circ}\text{C}$ .

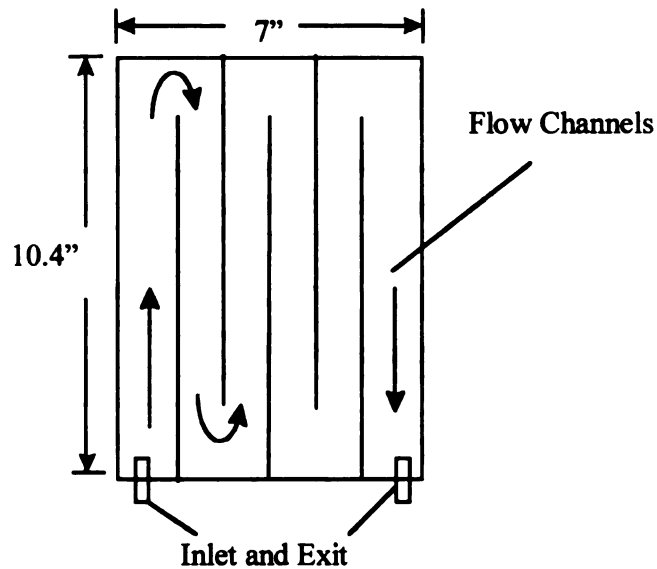


**Figure 2.8.** Interior flow pattern of the thermally active test section.

Transient surface temperature changes are obtained by using a bypass loop in the coolant circuit (Figure 2.9). The bypass loop can be closed and the coolant pumped into the thermally active test section. This results in a transient surface temperature as shown in Figure 2.10. These results show that a rapid change in the surface temperature of the thermally active test section can be obtained in 45 seconds and that the temperature can be monitored and recorded for modeling purposes. This change could be utilized to model transient changes in the automotive environment such as a sudden rain or snow fall (thus changing windshield temperature). While not directly analogous to a specific automotive event, the dynamic modeling capabilities of the software can be verified with the data obtained.

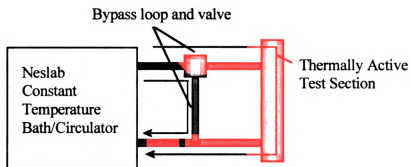


**Figure 2.9.** Bypass loop schematic for transient thermal tests.

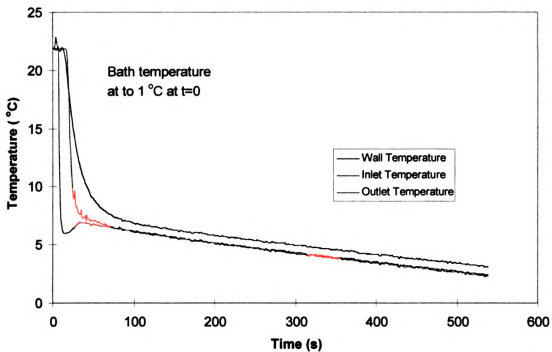


**Figure 2.10.** Transient temperature history of the thermally active test section.

## 2.6 CALIBRATION AND CHARACTERIZATION EXPERIMENTS

Several verification experiments were conducted to insure that certain assumptions regarding the FMTF system were correct. This section will detail the characterization experiments, which include a Pitot tube check of the velocity at the exit plane of the contraction. A spanwise (z - direction) velocity profile was also obtained to verify the two-dimensionality of the jet profile issuing from the two-dimensional contraction. The contraction (nozzle) was designed specifically for this facility. The thermal and humidity stability of the FMTF flow facility was also investigated to define the experimental steady-state and quantify transient response times of the FMTF system.

### 2.6.1 TEST CONTRACTION MEASUREMENTS

The fluid velocity above the contraction is not equal to zero because of flow confinement in the duct. The geometry of the flow is known and the continuity equation is utilized to substitute for  $V_1$  in the Bernoulli equation (2.2) for flow through the two dimensional contraction. The area ratio of  $A_1$  to  $A_2$  for the two-dimensional contraction is 5:1, thus  $V_1$  is equal to 20% of  $V_2$ . Thus the velocity terms in Equation (2.2) can be simplified as

$$V_2^2 - V_1^2 = V_2^2 - \left(\frac{V_2}{5}\right)^2 = (1 - 0.04) V_2^2 = 0.96 V_2^2. \quad (2.3)$$



Substituting this result into Equation (2.2) and solving for the exit velocity from the two-dimensional contraction ( $V_2$ ) yields

$$V_2 = \sqrt{\frac{2(P_1 - P_2)}{0.96 \rho}}. \quad (2.4)$$

The comparison between the Pitot tube measurements and the pressure tap measurements are presented in Figure 2.11 for the two-dimensional contraction. The Pitot tube method and the static pressure tap method yield results that differ by less than 0.5% at the test flow velocity of 10 m/s, thereby verifying that the pressure tap method or the Pitot tube allows for accurate measurement of the inviscid core jet velocity. The velocity measurement of the inviscid core of the jet ( $U_j$ ) will be utilized primarily to present the velocity measurement results in a standard non-dimensionalized format.

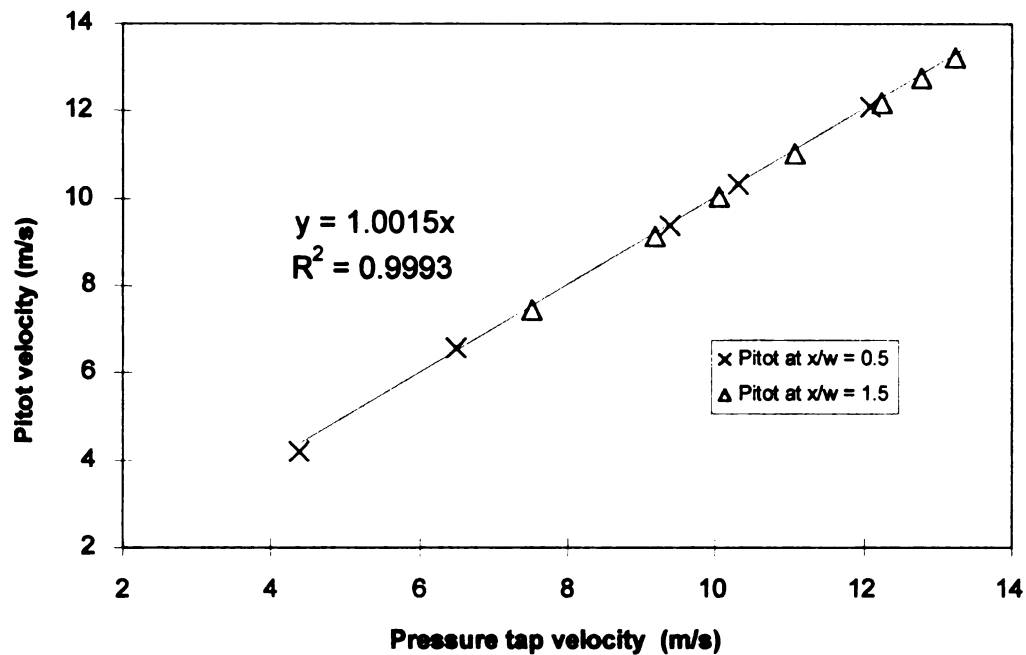


**Figure 2.11.** Comparison of test contraction velocity (from pressure tap measurements) and Pitot tube measured velocity.

### 2.6.2 SPATIAL FLOW UNIFORMITY MEASUREMENTS

The flow characteristics of the wall jet were measured. The goal of the flow conditioning was to provide a wall jet that was spatially uniform with regard to velocity, temperature, and humidity. The characteristics of interest were the free stream turbulence intensity as well as the uniformity and stability of temperature and humidity. These variables are indications of the quality of the flow conditioning and the two-dimensional contraction design.

The free stream turbulence intensity was measured with a single hot-wire probe at the exit plane ( $x/w = 0$ ) of the test contraction. The RMS (root mean square,  $u'$ ) of the velocity measurement is a quantitative measurement of the fluctuation level present in the flow. The measured value of  $u'/U$  was less than 1.5% in the inviscid core of the jet at the  $x/w = 0.0$  position.

A spanwise ( $z$ -direction) traverse of the wall jet was performed with a single hot-wire to verify the two-dimensionality of the jet flow. The  $z$ -direction mean velocity ( $W_z$ ) is assumed to be zero and the root mean square (RMS) is assumed to be very small compared to the  $x$  and  $y$ -directions. If this assumption is valid, the wall jet profile would be variable only in the  $x$  and  $y$ -directions and therefore the  $z$ -direction profile should be flat and independent of  $z$  location near the center of the wall jet. Figure 2.13 presents  $U/U_{\max}$  as a function of  $z/L$ . The variable  $z/L$  is the location in the  $z$ -direction non-dimensionalized by the slot length ( $L = 35.6$  cm). Figure 2.12 shows the sharp increase of the velocity at the outer edge of the slot ( $z/L = -0.5$ ) and the flat profile from the outer edge of the slot past the center of the slot ( $z/L = 0$ ). Note that only one edge of the flow was interrogated due to the symmetric design of the facility.

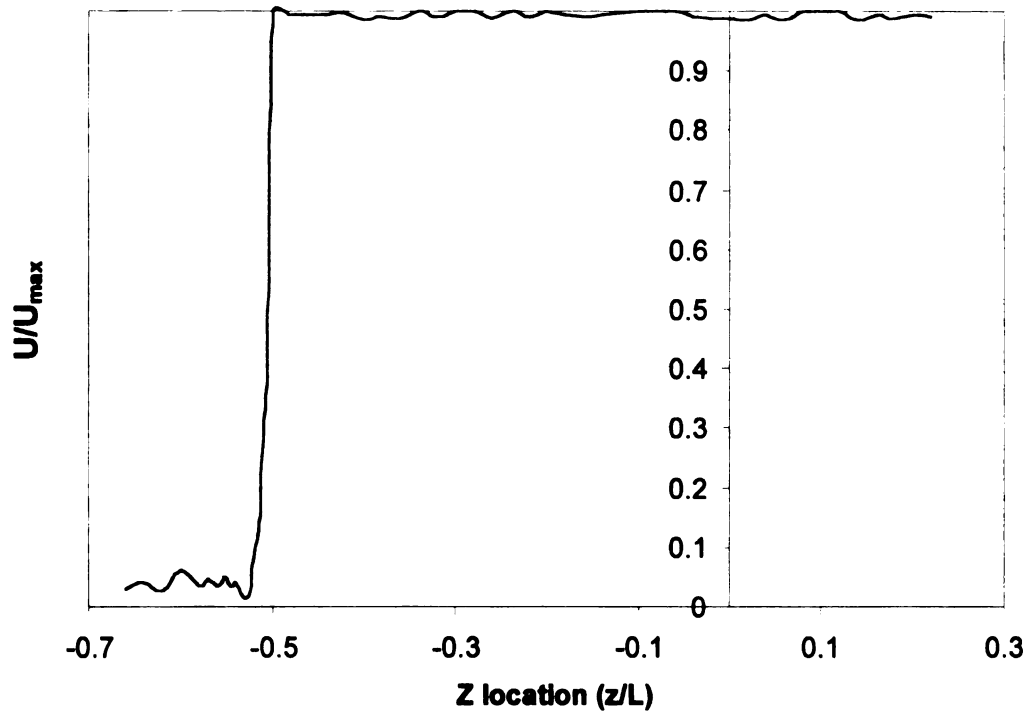


**Figure 2.12. Z-direction (transverse) velocity profile;  $y/w = 0.5$ .**

The temperature field within the jet flow was measured by positioning type-T thermocouples at multiple locations across the exit plane of the jet. These measurements are presented along with the humidity data in Figure 2.13. The temperature and humidity of the flow are spatially uniform within the measurement resolution capabilities. The data presented in Figure 2.13 show a homogeneous temperature and humidity field along the centerline of the thermally active test surface ( $z/L = 0$ ). The gradients near the edges of the thermally active test surface (near  $z/L = -0.5$  and  $z/L = 0.5$ ) are created by the jet mixing with the air in the sub-atmospheric test chamber. All velocity and

temperature measurements presented are taken along the centerline of the thermally active test surface unless specified otherwise. The spatial uniformity along the jet exit is essential to insure the two dimensionality of the flow.

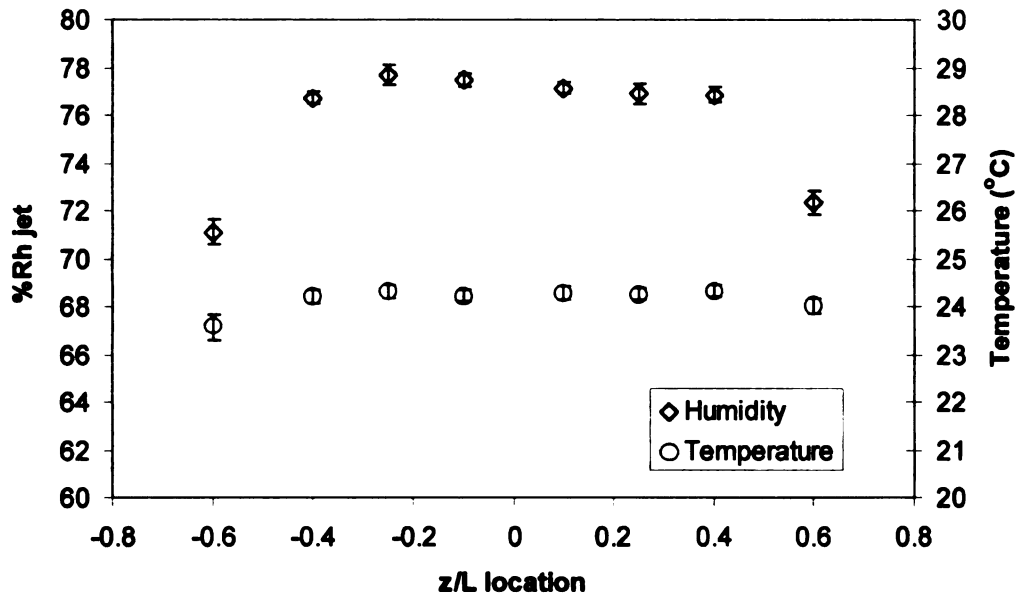


**Figure 2.13.** Jet temperature and humidity uniformity study ( $w = 2$  cm).

### 2.6.3 TEMPORAL STABILITY OF THE FMTF TEMPERATURE AND HUMIDITY

Experiments were conducted to determine the temporal stability of temperature and humidity within the FMTF sub-atmospheric test chamber and within the wall jet flow. These data help define the amount of time the system requires to reach steady-state as well as the stability of the steady-state

condition. These experiments were executed with the Armstrong Model 90 steam humidifier providing flow humidification and with the thermally active test section chilled to the point where condensation was actively occurring (approximately %Rh<sub>j</sub> = 70, T<sub>j</sub> = 22 °C, and T<sub>s</sub> = 12 °C).

The wall jet reacted very quickly ( < 120 s) to steam humidification from the Armstrong Model 90 humidifier. The environment in the sub-atmospheric test chamber was slower to equilibrate (~ 30 min.) due to the low entrainment velocities present and the volume (1.62 m<sup>3</sup>) of the test chamber. The volumetric flow rate through the system for a typical test is 0.14 m<sup>3</sup>/s, but little of the wall jet is dispersed throughout the chamber.

The wall jet temperature is typically several degrees warmer (2 – 3 °C) than the sub-atmospheric test chamber upon system start up due to the location of the intake near the top of the laboratory. The addition of steam humidification also increases the wall jet temperature. Figure 2.14 shows the thermal response of the wall jet. The humidity measured in the wall jet equilibrates much quicker than the temperature and is also included in Figure 2.14. The tests were initiated from the “cold start up” condition where the FMTF had equilibrated with the ambient laboratory conditions. Two different velocities were included to demonstrate the limitation of the humidification system, which can be seen when comparing the two tests. Note that ambient humidity was approximately 11%Rh for both tests. The overshoot and settling time of the General Eastern M2-Plus sensor is also clearly evident in Figure 2.14.

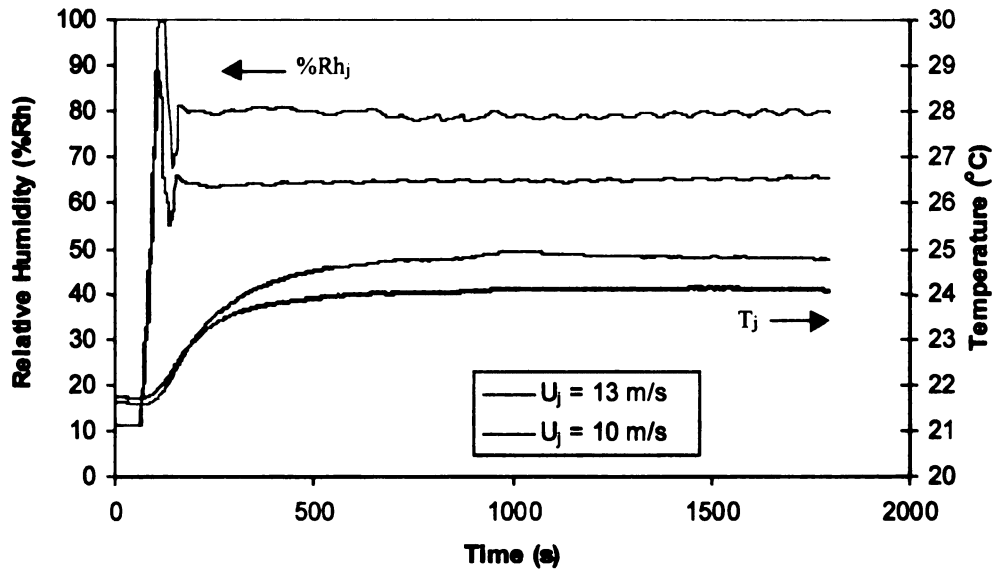


**Figure 2.14.** Typical transient response data for the wall jet flow in the FMTF.

Figure 2.14 indicates that the FMTF response to humidity changes is faster than to temperature changes and that steady-state conditions were reached within 8.3 minutes (500 s). The steady state jet conditions were stable within 2% Rh and 1 °C. These results defined the necessary settling time for the facility to obtain steady state operation. They also began to establish the limitations of the transient changes that may be implemented experimentally.

## **Chapter 3**

### **ISOTHERMAL FLOW MEASUREMENTS**

The wall jet flow field was first investigated as an isothermal flow. The isothermal, two-dimensional wall jet has been rigorously studied as detailed in Chapter 1. The purpose of this study was to investigate the developing region of the wall jet for three specific reasons:

1. To establish confidence in the experimental techniques through direct comparison with previous studies in the literature.
2. To detail the developing region of the wall jet which is subject to unique features of the flow facility. These effects damp out as the flow develops down stream.
3. To establish baseline data for comparison to future non-isothermal tests and to the CFD simulation results.

The isothermal experimental technique will first be discussed, followed by presentation of the measurement results. The experimental data will then be compared to the results from the literature and from the CFD model. Finally, the experimental procedure and the results will be evaluated.

The several features of the wall jet will be discussed. The definitions of various features and zones in the wall jet flow are defined in Figure 3.1. The inner and outer shear layers are defined based on the derivative of the time averaged velocity ( $U$ ) gradient with respect to the wall normal direction ( $y$ ).



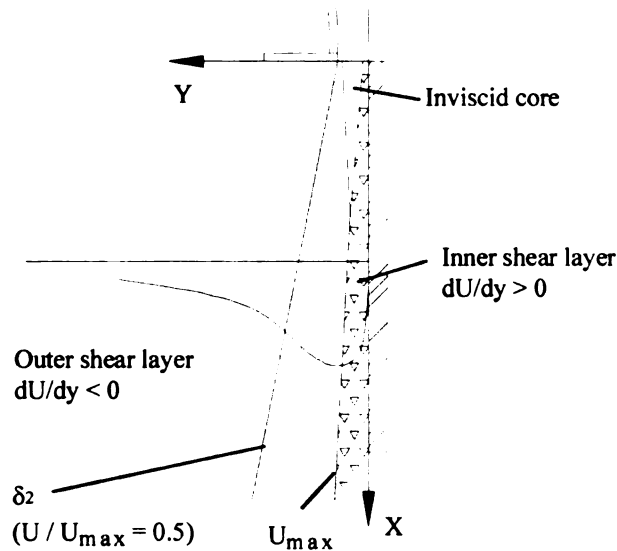


**Figure 3.1.** Definitions of features and zones in the two-dimensional wall jet flow.

### 3.1 MEASUREMENT RESULTS

Isothermal test data were obtained with a single hot-wire probe (velocity) and a calibrated thermocouple (temperature). The electrical resistance of the hot-wire is a function of temperature. Therefore, an average temperature is equivalent electronically to an average resistance. The hot-wire was maintained at a constant average temperature ( $\sim 230^\circ\text{C}$ ) by the anemometer control circuit. The control circuit utilizes a balanced Wheatstone bridge and Joule heating to maintain the sensing wire at a fixed average resistance. The hot-wire sensor is only responsive to changes in the convective cooling velocity in an isothermal flow and can therefore be calibrated easily to measure velocity. Although these

tests were performed for isothermal conditions (the jet and the thermally active test surface were not thermally active), temperature compensation is necessary to insure accurate hot-wire measurements if the ambient temperature during testing is different than the ambient temperature during hot-wire calibration. The hot-wire and thermocouple were traversed across the wall jet width with the stepper motor positioning system. The stepper motor and the output data were controlled/recorded with the systems described in Chapter 2. These measurements were conducted at ambient laboratory conditions. These were typically  $T_{\infty} \sim 22^{\circ}\text{C}$  and  $\%Rh \sim 60\%$ . The velocity of the inviscid core of the jet was set at 10 m/s for each test to provide a flow velocity comparable to the automotive flow field.

The isothermal velocity profiles are presented in their non-dimensional form ( $U/U_{\max}$  as a function of  $y/\delta_2$ ) in Figures 3.2 - 3.7. The peak velocity in each profile is defined as  $U_{\max}$ ;  $U_{\max}$  differs at each  $x/w$  location due to slight variations in the experimental set up and decay of the velocity as the jet progresses down stream. The ordinate is defined as  $y/\delta_2$ , where  $y$  is the distance from the test surface and  $\delta_2$  is the distance from the test surface in the  $y$ -direction to the location where the velocity ( $U$ ) has decreased to 50% of its maximum value ( $U_{\max}$ ) in the outer shear layer. This format collapses the data to a single profile when the jet has reached the *self-preserving*, fully-developed flow configuration [Potter and Foss, 1982]. The streamwise normal stress (SNS) is also included in each figure. The SNS is defined as

$$SNS = 100 \frac{u'^2}{U^2} \quad (3.1)$$

The SNS is an alternate method of presenting the root mean square (RMS) of the velocity fluctuations or the turbulence intensity.

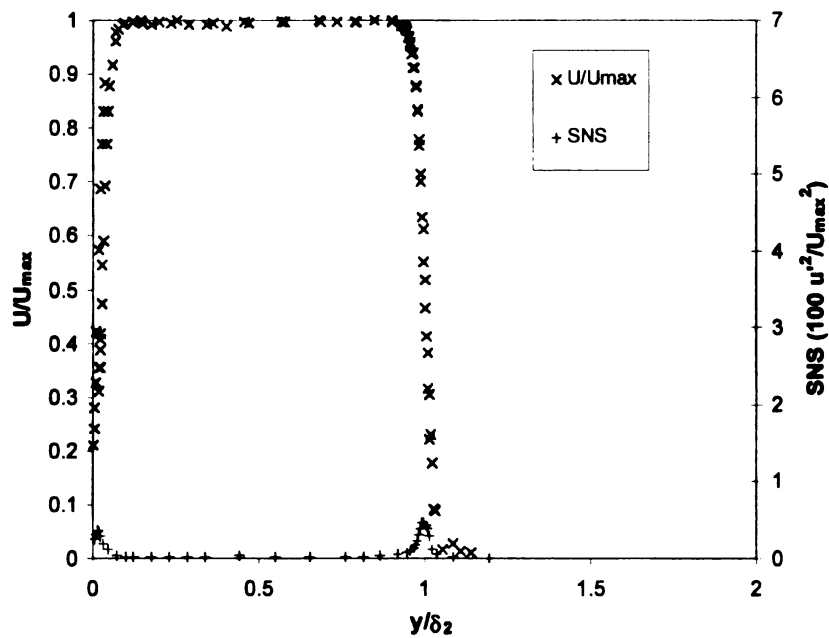


**Figure 3.2.** Non-dimensional velocity profile at  $x/w = 0.0$ .

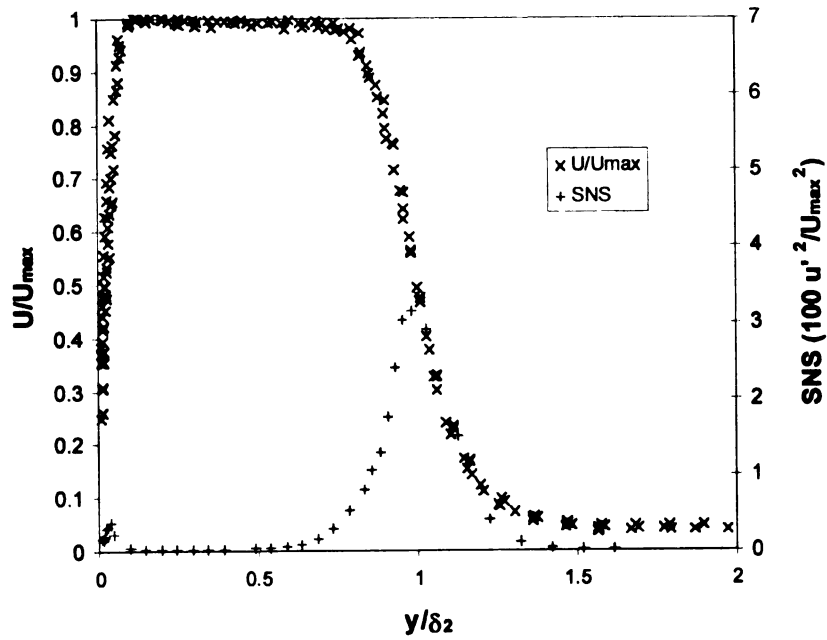


**Figure 3.3.** Non-dimensional velocity profile at  $x/w = 1.59$ .

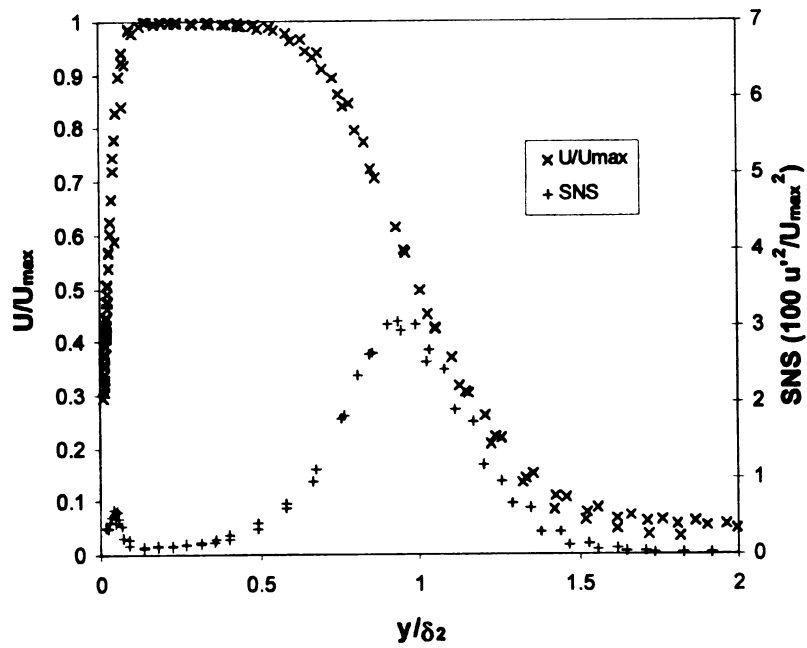


**Figure 3.4.** Non-dimensional velocity profile at  $x/w = 3.18$ .

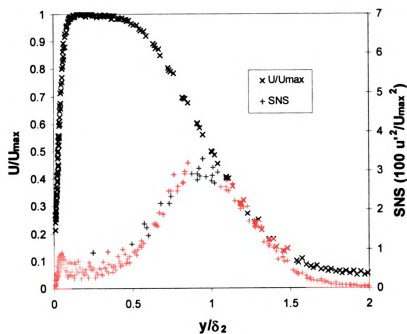


**Figure 3.5.** Non-dimensional velocity profile at  $x/w = 4.45$ .

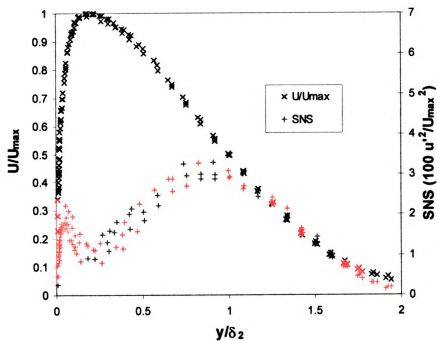


**Figure 3.6.** Non-dimensional velocity profile at  $x/w = 7.62$ .

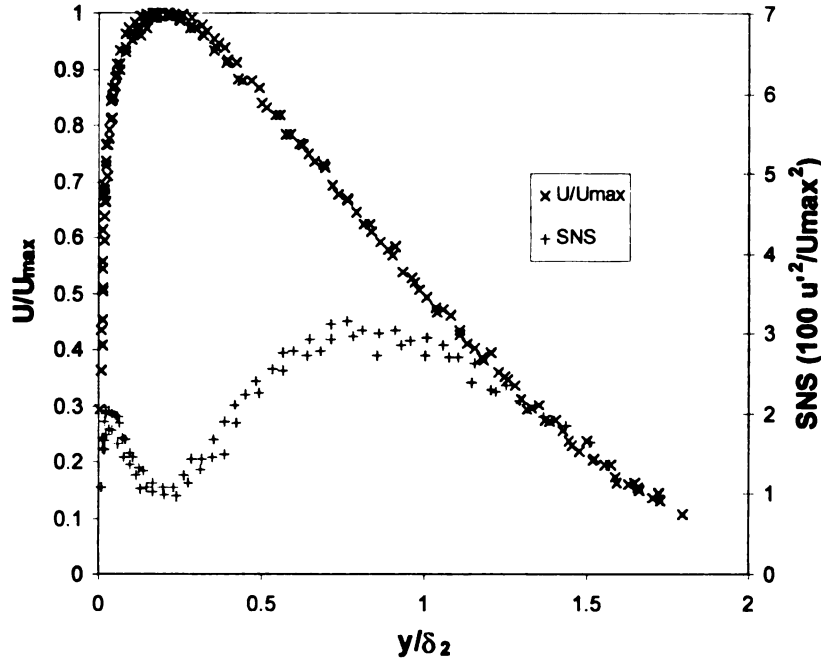


**Figure 3.7.** Non-dimensional velocity profile at  $x/w = 10.8$ .

The widening of the jet profile as the flow progresses in the streamwise direction is evident in Figures 3.2 - 3.7 as the flow develops from the "top hat" profile at the jet exit to the smooth profile at the downstream positions. The inviscid core region of the flow is evident in the profiles for  $x/w < 5$ . This region appears as a flat section in the profile and is very evident in the  $x/w = 0.0$  and  $x/w = 1.59$  profiles (Figures 3.2 and 3.3). The spreading of the jet into the stagnant air is also evident as the jet advances downstream. The inviscid region becomes narrower and disappears as the flow advances and the outer sheared region of the jet and the inner boundary layer advance toward the center of the jet and eventually meet (at approximately  $x/w \sim 6$ ).

It is expected that once the jet becomes fully-developed that the data will collapse to a single curve. Data from  $x/w = 7.62$  and  $x/w = 10.8$  are presented in Figure 3.8 along with data from Tailland [1967] and Eriksson et al. [1997] at  $x/w = 600$  and  $x/w = 20$  respectively. Note that the decay rate of the maximum velocity can also be compared between other fully developed wall jets as a means to verify the two dimensionality of the jet and to insure the self-preserving nature. This study focused on the developing region however and only two measurements of the maximum velocity did not include the inviscid core. At  $x/w = 7.62$  and  $10.8$ , the maximum velocity had decreased to approximately 98% and 94% of the jet velocity respectively.

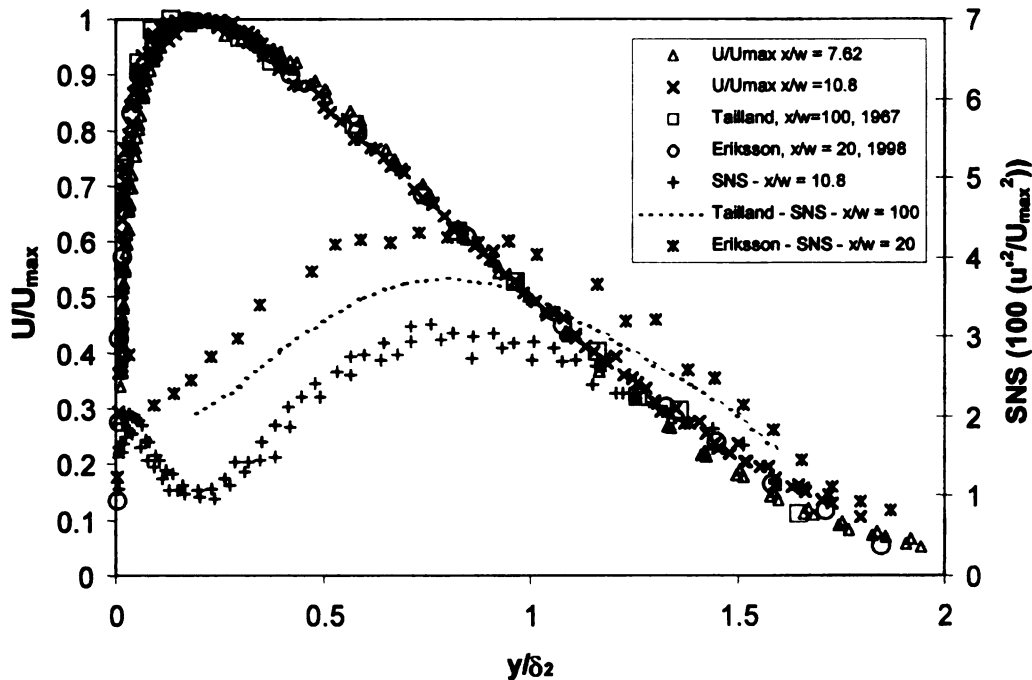


**Figure 3.8.** Comparison of experimental data to results from the literature.

It is concluded from the results presented in Figure 3.8 that the self-preserving, mean velocity profile develops between the measurement locations of  $x/w = 7.62$  and  $x/w = 10.8$  in the FMTF facility. The experimental data at  $x/w = 10.8$  agrees to within 1% of  $U_{\max}$  with the fully developed wall jet profiles in the literature. Note that the streamwise normal stress does not agree as well as the mean velocity profile. The SNS profile measured at  $x/w = 10.8$  is 20% to 30% lower than Tailland's data across the jet. This indicates that the mean flow has just assumed the fully developed form and the higher moments are still developing [Tennekes and Lumley, 1994] and that the initial jet conditions are still effecting the flow.

### 3.2 COMPUTED RESULTS AND COMPARISON TO EXPERIMENTAL DATA

A computational model of the FMTF facility was developed at Ford Motor Company by Dr. B. AbdulNour. A 2-dimensional, structured, quadrilateral mesh is generated from the geometry of the flow facility. The mesh contains 188,353 cells and is heavily clustered near the thermally active test surface to improve resolution and accuracy in this region. The general-purpose CFD package FLUENT<sup>®</sup> 5 is used for the numerical simulation. The grid was adapted iteratively per the solution results in terms of  $y^+$  and the velocity gradient. The  $y^+$  dimension of the first computational node along the surface ranges from 0.975 to 1.23. Both a modified  $k-\epsilon$  and a Reynolds stress model (RSM) were utilized to model flow



turbulence. Mean velocity and SNS results were nearly identical for the two turbulence models.

The results of the computational model are presented in Figures 3.9, 3.10 and 3.11. Figure 3.9 presents an overview of the CFD results. The development of the mean velocity and streamwise normal stress profiles are evident in this figure. Figures 3.10 and 3.11 show the data for  $x/w = 0.0$  and  $x/w = 10.8$ . Experimental velocity data for  $x/w = 0.0$  and 10.8 are included in Figures 3.10 and 3.11 for comparison purposes.

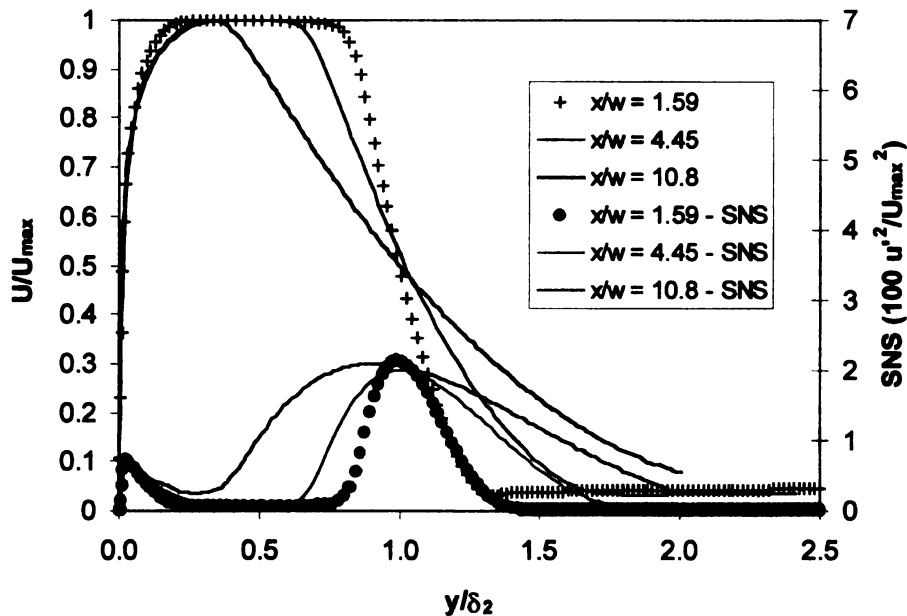


**Figure 3.9.** Computed velocity results for the wall jet flow field. Reynolds stress model utilized.

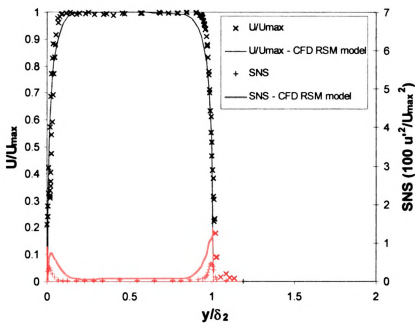


**Figure 3.10.** Comparison of experimental and computed velocity results

at  $x/w = 0.0$ .

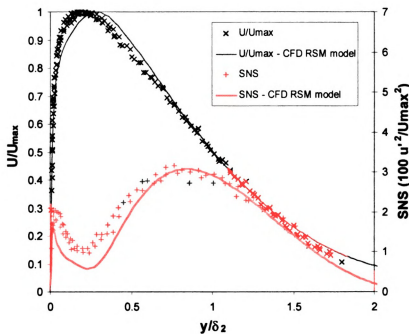


**Figure 3.11.** Comparison of experimental and computed velocity results

at  $x/w = 10.8$ .

The computed jet spreading rate was also compared to the experimental results. The rate of the spread of the jet can be monitored using the location of  $\delta_2$  as the flow develops. Figure 3.12 contains the jet spreading data. It can be seen that initially, the computational jet is wider but that the experimental flow growth rate exceeds the CFD result. It is of interest to note that this is the approximate location where the experimental flow has lost the inviscid core and is expected to begin transition to turbulent flow. The experimentally measured jet growth rate is 32% greater than the computation result, although the jet width at  $x/w = 10.8$  is only different by approximately 5%.

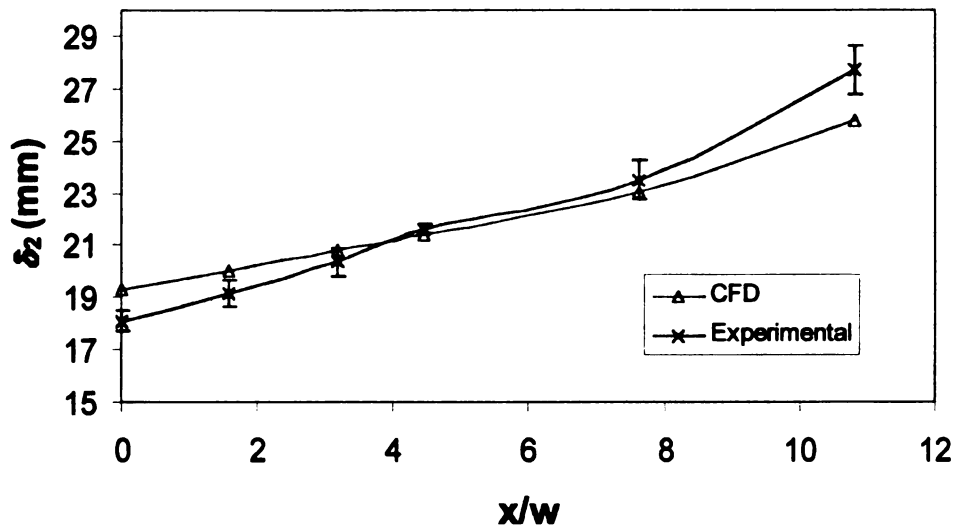


**Figure 3.12.** Comparison of jet spreading rates (location of  $\delta_2$ ).

### 3.3 DISCUSSION OF RESULTS

The measurements in the developing region of the wall jet illustrate the transition of the jet from the slug like profile at the contraction exit ( $x/w = 0.0$ ) to the onset of the fully developed mean velocity profile. The inner boundary layer of the experimental flow is laminar like at the exit of the two dimensional contraction. Figure 3.13 shows a comparison of the inner and outer boundary layer profiles at the contraction exit to the Blasius similarity solution profile [Bejan, 1995].

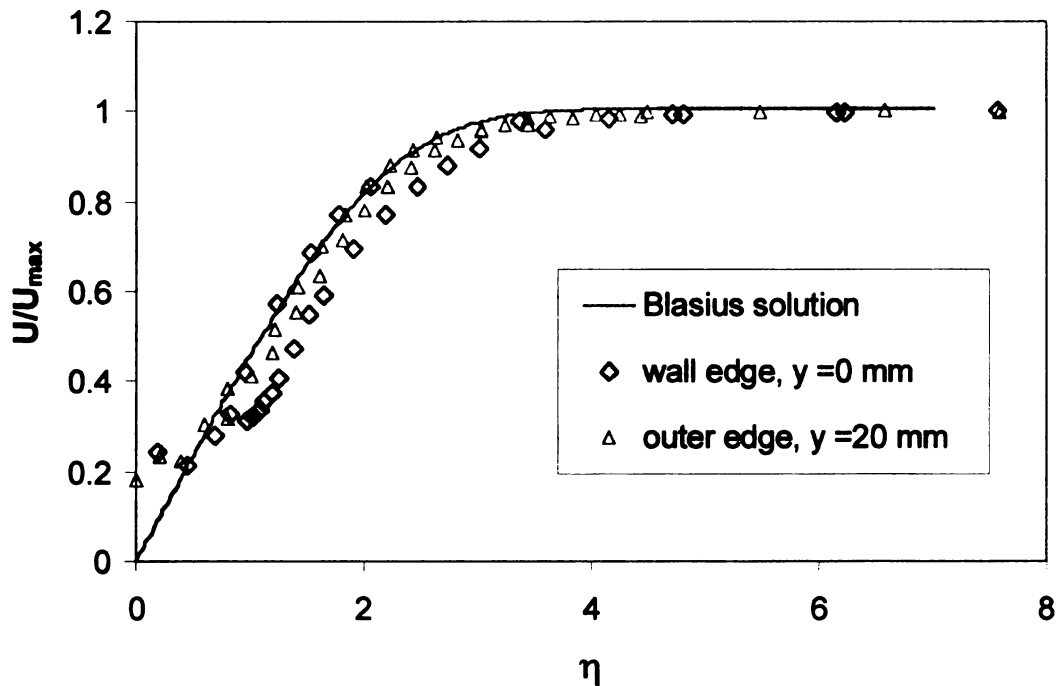


**Figure 3.13.** Boundary layer profiles at  $x/w = 0.0$  compared to the Blasius laminar profile.

This laminar like profile indicates that the flow must begin to undergo a transition to turbulence prior to  $x/w = 10.8$ . The transition phenomenon can be inferred since the mean velocity profile at  $x/w = 10.8$  conforms to the fully developed, turbulent wall jet profile. The experimental results agree exceptionally well (typically  $< 1\%$  of  $U_{\max}$ ) with the fully developed mean profile results extracted from the literature as seen in Figure 3.8.. This level of agreement is utilized to validate the measurement techniques and establishes confidence in the methods and equipment utilized for this study.

Comparing the measured velocity results with the CFD model illustrates two major discrepancies. The boundary layers at the contraction exit ( $x/w = 0.0$ ) are thicker in the computed result than those measured. The inner boundary layer also thickens more rapidly as the flow proceeds downstream in the computational model than in the experiment even though the computed wall jet profile growth rate is less than the experimental result. The experimental  $\delta_2$  grows from 18.2 to 27.7 mm from the slot exit to  $x/w = 10.8$  while the computational result grows from 19.3 to 25.7mm in the same region.

The most significant difference between the experiment and the computation is in the inner boundary layer region near the thermally active test surface. The computational boundary layer grows thickens at a greater rate than the experimental measurements indicate. This is clearly evident if the peak location of  $U/U_{\max}$  is considered in Figures 3.10 and 3.11. The CFD code over-predicts the growth of the inner boundary layer. The code is utilizing a turbulence model that is active throughout the flow field even though the

experiment indicates that there is a laminar like boundary layer at the jet exit ( $x/w = 0$ ). Thus the computational flow does not develop a laminar boundary layer that undergoes a transition to turbulence. This would also impact the velocity gradient (shear stress) at the wall, which would be expected to strongly influence the heat and mass transfer. In light of these considerations, a computational model with a divided mesh in which non-turbulent regions of the flow could be inserted and modeled is recommended to attain more accurate simulation results.

The computed result does approximate the experiment reasonably well. The largest variations in the mean velocity profiles between the experiment and the CFD occur in the inner boundary layer region. At  $x/w = 4.45$ ,  $y/\delta_2 = 0.1$ , there is a 13% difference in the mean velocities. This is the largest variation between the results and it decreases to an 8% variation at  $x/w = 10.8$ . The decrease in the maximum mean velocity at each streamwise location agrees to within 1.5% between the experimental measurements and the CFD results.

The Stream-wise Normal Stress (SNS) profiles agree within the experimental variation at every outer peak (in the outer shear layer) location. The SNS peak in the inner boundary layer differs by as much as 28% between the experimental and the computed results. This difference is probably also due to the use of a turbulence model throughout the flow. The inner and outer peaks of the computed SNS profiles at  $x/w = 10.8$  agree with the experiment within the experimental variation. Results from a CFD model with non-turbulent grid zones incorporated near the jet orifice have not been provided for comparison at this

time, but they are expected to improve the comparison between the experiment and the computation, especially in the inner boundary layer.

## **Chapter 4**

### **STEADY STATE, NON-ISOTHERMAL, NON-CONDENSING MEASUREMENTS**

The next phase of the project was to measure thermal effects in the flow field. The thermally active test section was chilled to add a thermal boundary layer to the flow. The temperature of the test surface was carefully monitored to prevent condensation from forming. This flow field added significant complications to the experimental technique as it required local temperature compensation for the hot-wire probe to be utilized. The hot-wire probe operates based on convective heat transfer and is therefore sensitive to temperature changes in the fluid flowing over the sensing wire. The data are utilized to verify the results of the CFD model with energy (heat) transfer occurring in the flow field. The following sections detail the experimental methods, uncertainty analysis, and experimental results. Comparisons to the isothermal work are made and the experimental data are compared to results from the computational model.

#### **4.1 EXPERIMENTAL METHODS**

A single 5  $\mu\text{m}$  diameter tungsten hot-wire was utilized for non-isothermal, non-condensing flow measurements to measure the streamwise velocity. Hot-wire sensors can be utilized in non-isothermal flows if the local fluid temperature can be measured and implemented to compensate the velocity measurement [Goldstein, 1996]. A cold-wire resistance thermometer constructed from 5  $\mu\text{m}$



diameter tungsten wire was utilized to measure the local fluid temperature. A cold-wire uses the temperature-electrical resistance material property to measure temperature electronically. The cold-wire probe was calibrated to determine the temperature-resistance relationship empirically. A very small sensing current (~1 mA) was used to measure the resistance (and therefore, the temperature) in the experimental wall jet flow field.

The velocity and temperature measurements in the non-isothermal flow were calculated from the hot-wire and the cold-wire signal using the following procedure. The temperature was calculated first from the cold-wire voltage signal with

$$T_{\text{Cold-wire}} = \frac{E - C_1}{C_2} \quad (4.1)$$

The quantities  $C_1$  and  $C_2$  were obtained from an ordinary least squares curve fit of the cold-wire calibration data. The measured voltage,  $E_{\text{measured}}$ , from the hot-wire was compensated utilizing the temperature output from the cold-wire with

$$E_{\text{Compensated}}^2 = E_{\text{Measured}}^2 \left( \frac{T_{\text{hw}} - T_{\text{cal}}}{T_{\text{hw}} - T_{\text{cw}}} \right) \quad (4.2)$$

Equation (4.2) compensated the hot-wire voltage for changes in the heat transfer relationship due strictly to variation of the local temperature from the temperature present when the hot-wire was calibrated. The velocity was then calculated with the compensated voltage value,  $E_{\text{compensated}}$ , utilizing Equation (4.3) presented by Collis and Williams [1959]:

$$E^2 = A + BV^n \quad (4.3)$$

The quantities A, B, and n were obtained from an ordinary least squares curve fit of the hot-wire calibration data. The cold-wire and the hot-wire probes must be calibrated prior to every experiment. Post calibration was also conducted if the probes survived the experiment intact. Note that Equation (4.3) was utilized until the TSI 1050 anemometer was replaced with the TSI IFA300 anemometer system. The IFA300 software replaced Equation (4.3) with a fourth order polynomial fit to the calibration data.

The sensors were aligned parallel to the wall along the same spanwise axis. The active sections were separated by 2.2 mm. Both sensors were constructed on site from 5  $\mu\text{m}$  diameter tungsten wire. A TSI anemometer was utilized to control the sensors and a 12 bit Keithley Metrabyte A/D card recorded their output at 8000 Hz for later data processing.

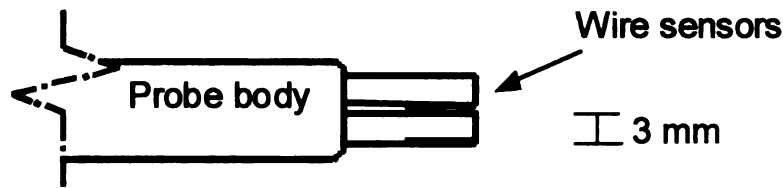


**Figure 4.1.** Schematic of the hot-wire/cold-wire dual probe sensing head.

The sensor positioning and data acquisition systems are configured as described in Chapters 2 and 3.

## 4.2 EXPERIMENTAL UNCERTAINTY

A hot-wire sensor is calibrated by positioning the probe in a flow with a known velocity as described in Chapter 3. The uncertainty in the thermally active experiments was slightly larger than the isothermal uncertainty due to the additional experimental variance added with the addition of the second sensor (the cold-wire). The experimental uncertainties in the non-isothermal flow of the velocity and temperature were calculated to be 3.5% of  $U_{\max}$  and  $\pm 0.5^\circ\text{C}$  respectively. The uncertainty in the velocity measurements was determined from the experimental variation from test to test. The temperature uncertainty was determined from the variance of the data utilized for the calibration data.

A cross correlation study was conducted with two hot-wires placed 4 mm apart in the flow. A correlation coefficient of 0.63 was measured indicating that the hot-wires were not necessarily measuring the same flow structure. The temperature and velocity are not necessarily correlated in this flow, but it is

essential that the hot-wire and cold-wire probes are measuring the same fluid mechanical event in order for the hot-wire temperature compensation to function properly. The worst scenario resulting from uncorrelated sensors is examined next.

The hot-wire measurement is compensated as indicated in Equation (4.2). The worst case scenario can be realized if the temperature and the velocity measurements are completely uncorrelated and out of phase. For example, the maximum temperature would occur locally at the hot-wire probe while the minimum (and incorrect) temperature fluctuation occurs at the cold wire probe. The maximum effect of this test case can be analyzed using the temperature data obtained in the flow. These data indicate that the maximum temperature fluctuation can be estimated as approximately  $0.15 (T_j - T_s)$  °C. The value of 0.15 is twice the RMS (standard deviation) measured at  $x/w = 10.8$ . This equates to 3 °C in a typical experiment. The error ( $\Delta E$ ) created in the hot-wire voltage can be calculated utilizing Equation (4.4).

$$\Delta E = E_{\text{Measured}} \left[ \left( \frac{(T_{\text{hw}} - T_{\text{cal}})}{T_{\text{hw}} - T_{\text{cw}} - 0.15(T_j - T_p)} \right)^{\frac{1}{2}} - \left( \frac{(T_{\text{hw}} - T_{\text{cal}})}{T_{\text{hw}} - T_{\text{cw}} + 0.15(T_j - T_p)} \right)^{\frac{1}{2}} \right] \quad (4.4)$$

Equation (4.4) results in a 1.26% error deviation from the correct compensated voltage. This will cause a maximum error of approximately 6.7% in the velocity at  $U = U_{\text{max}}$  (67cm/s at 10 m/s) utilizing a typical hot-wire calibration

result. However, the peak temperature fluctuation does not coincide with the maximum velocity. Thus the error can be more accurately estimated at 1.9% of  $U_{\max}$  (19 cm/s) in the inner boundary layer of the flow. Also note that this is the two standard deviation fluctuation level and thus 95% of the actual error is likely to be significantly less. Recall that the integral length scale of the flow was determined to be approximately 8 mm. This level of error was deemed acceptable since the actual wire sensing sections are closer together than 4 mm and the correlation coefficient is not actually zero.

#### **4.3 MEASUREMENT RESULTS OF THE NON-ISOTHERMAL, NON-CONDENSING EXPERIMENTAL REGIME**

The wall jet temperature was typically 24 °C (but varied with ambient conditions slightly from day to day ( $\pm 1$  °C)) and the temperature of the thermally active test section was set at 4 °C. The ambient humidity varied from 15% to 25% Rh from day to day, but was constant for the duration of each non-isothermal experiment to within 2% Rh. Note that for these conditions the dew-point never exceeds 3.6 °C.

Within the measurement uncertainty, the velocity profiles measured in the non-isothermal, non-condensing flow showed no deviation from the isothermal velocity measurements. This was expected due to the small changes in the fluid properties over the temperature range present in the thermal boundary layer. This result was further supported by a comparison of the Grashoff number and

the Reynolds number. This comparison indicated that the momentum effects were several orders of magnitude larger than the buoyancy effects. Based on these assumptions, it was expected that the thermal boundary layer would have a negligible effect on the velocity profile in the wall jet flow. The data displayed in Figure 4.2 show the comparison between the measured velocities at  $x/w = 10.8$  in the isothermal and non-isothermal, non-condensing experimental regimes. Figure 4.2 contains 3 non-isothermal, mean velocity data sets and the ensemble average of 5 isothermal experimental data sets. These non-isothermal data sets were statistically indistinguishable from the isothermal data with a null hypothesis test at a 95% confidence level.

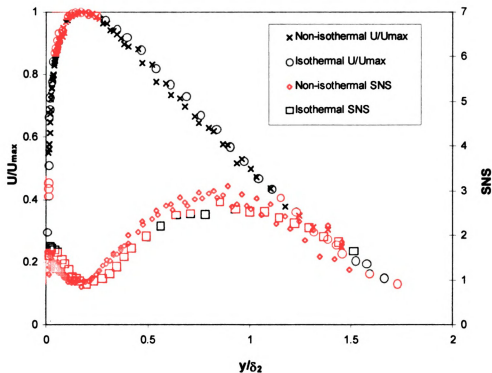


**Figure 4.2.** Comparison of velocity profiles in the non-isothermal, non-condensing and isothermal experimental regimes;  $x/w = 10.8$ .

The isothermal estimation of the wall shear stress was utilized to non-dimensionalize the velocity data into wall coordinates due to isothermal velocity measurements obtained closer to the wall than the non-isothermal, non-condensing measurements. The single hot-wire isothermal measurements were simpler to perform which made obtaining near wall velocity data easier. The near wall, isothermal velocity measurements were compared to other experimental measurements of the wall jet profile such as the data from Wygnanski et al. [1992]. This comparison is presented in Figure 4.3.

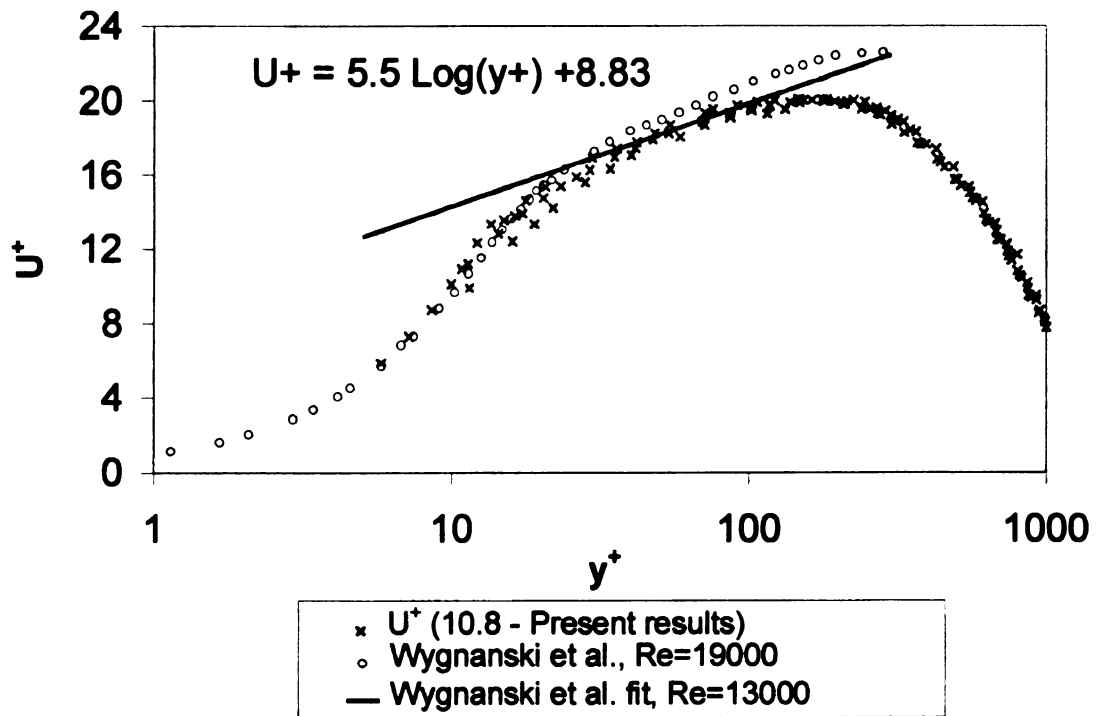


**Figure 4.3.** Comparison of the self preserving momentum profile in inner coordinates to data from Wygnanski et al. [1992];  $x/w = 10.8$ .

Figure 4.3 indicates the agreement between the 5 individual, isothermal experimental data sets and that of Wygnanski et al. This comparison indicates that the near wall velocity measurements are consistent with data in the literature. The shear velocity was estimated from the linear velocity profile measured near the test surface. Wygnanski also utilized near wall ( $y < 400 \mu\text{m}$ ) velocity measurements to calculate the shear velocity,  $U_\tau$ . This method tends to be less ambiguous than the Clauser method of estimating shear velocities. Note that the larger difference between the results beyond  $y^+ = 100$  is due to the larger velocities in the outer shear layer associated with a higher slot Reynolds number.

#### **4.3.1 NON-ISOTHERMAL VELOCITY PROFILES**

Detailed velocity profiles of the non-isothermal wall jet flow field were taken, but were indistinguishable from the isothermal profiles measured previously. This result was critical to the experimental program because it demonstrated that the hot-wire temperature compensation with the cold-wire measurement was functioning properly. Error in the compensation technique or in the cold-wire measurement would cause measurement errors in the velocity profile. Figure 4.4 through Figure 4.8 present the measured time-averaged velocity data and the streamwise normal stress (SNS) in the non-isothermal wall jet flow for the experimental locations  $x/w = 0.0, 1.59, 4.45, 7.62,$  and  $10.8,$  respectively.

The number of data sets,  $n$ , is indicated in each figure title. The reduction of the inviscid core due to growth of the inner boundary layer and outer shear



layer is evident in these figures. The figures also show the increasing magnitude of velocity fluctuations near the wall and the inward propagation of the shear layer turbulence as the flow advances in the streamwise direction.

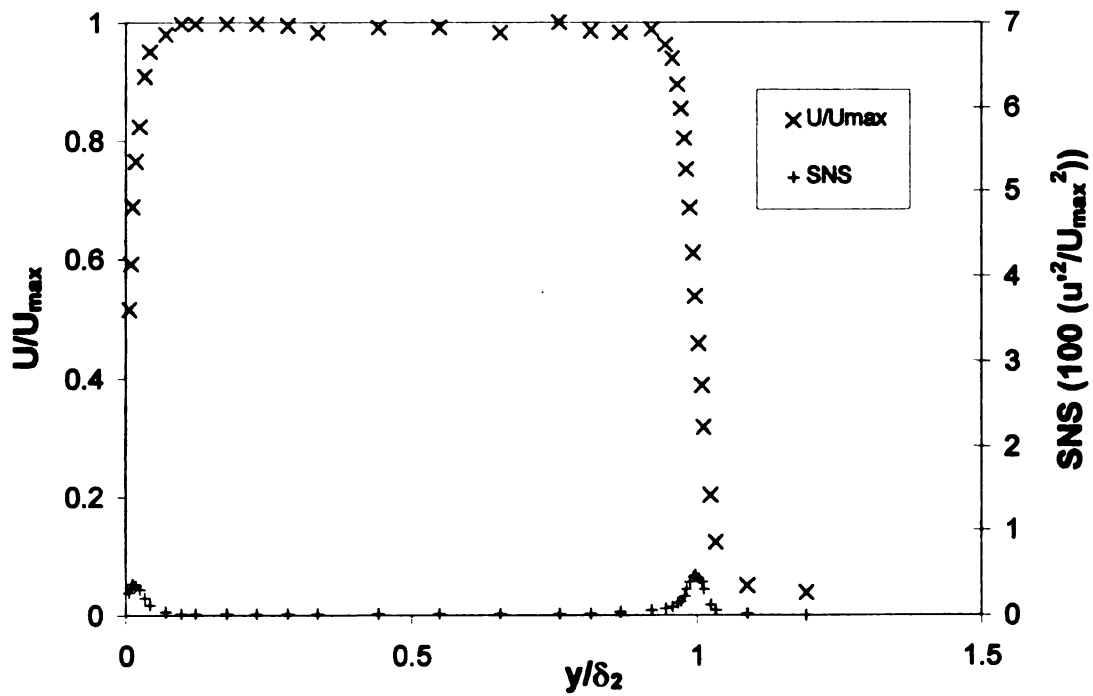


**Figure 4.4.** Velocity profile at  $x/w = 0.0$ ; non-isothermal;  $T_s = 4\text{ }^\circ\text{C}$ ;  $n = 1$ .

1  
0.8  
0.6  
 $U/U_{max}$   
0.4  
0.2  
0

Figure

1  
0.8  
0.6  
 $U/U_{max}$   
0.4  
0.2  
0

Figure

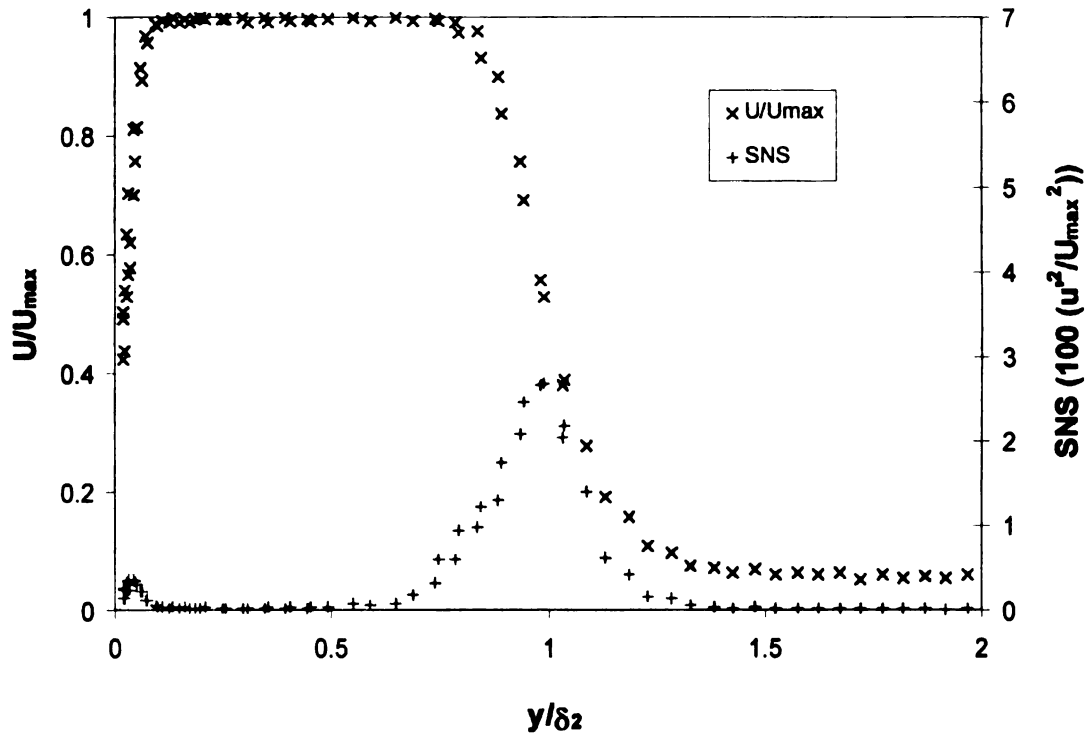


**Figure 4.5.** Velocity profile at  $x/w = 1.59$ ; non-isothermal;  $T_s = 4\text{ }^{\circ}\text{C}$ ;  $n = 2$ .

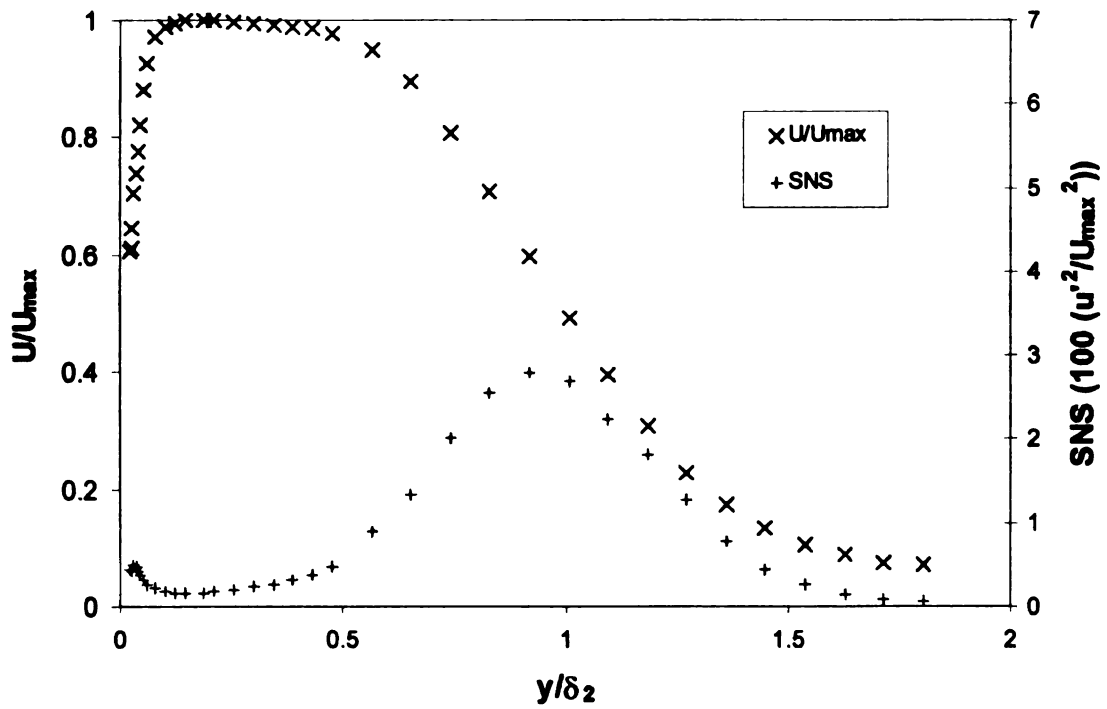


**Figure 4.6.** Velocity profile at  $x/w=4.45$ ; non-isothermal;  $T_s = 4\text{ }^{\circ}\text{C}$ ;  $n = 1$ .

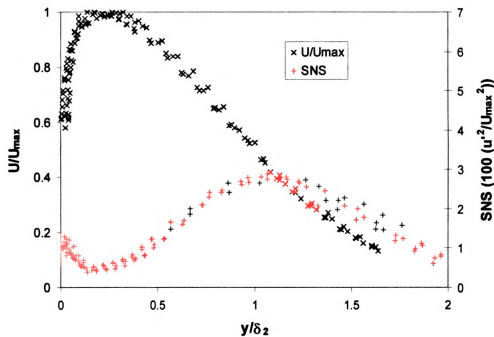


Figure 4.7. Velocity profile at  $x/w = 7.62$ ; non-isothermal;  $T_s = 4$  °C;  $n = 4$ .

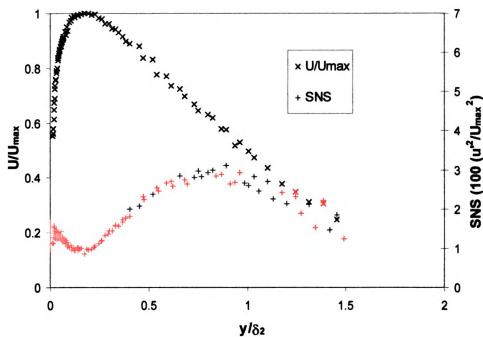


Figure 4.8. Velocity profile at  $x/w = 10.8$ ; non-isothermal;  $T_s = 4$  °C;  $n = 3$ .

expect

moment

experin

numbe

implem

indicat

solve t

measu

diamet

The re

experin

thus m

The ch

each e

0.003

[Thole

separa

can be

The conclusion drawn from the velocity measurements was that, as expected, the presence of the thermal boundary layer did not affect the momentum characteristics of the flow to an extent that was detectable with the experimental methods applied. This verified the results of the Grashoff-Reynolds number comparison and provided evidence that the cold-wire measurement was implemented properly to compensate the hot-wire output. This result also indicates that the CFD simulation could utilize an uncoupled methodology to solve the momentum and energy equations without introducing significant error.

#### **4.3.2 NON-ISOTHERMAL TEMPERATURE PROFILES**

The temperature data were taken directly from the cold-wire measurements utilizing Equation (4.1). The cold-wire was constructed from 5  $\mu\text{m}$  diameter tungsten wire, 1 mm in length with a typical resistance of 3-5 ohms. The resistance of the wire was measured with a 1 mA sensing current during the experiments. This low current resulted in negligible heating of the sensor and thus minimized the cold-wire sensitivity to changes in the convective velocity. The change in the resistance as a function of temperature was calibrated prior to each experiment. The coefficient of resistivity for tungsten is approximately  $0.003 \Omega/(\Omega ^\circ\text{C})$ . A very low noise amplifier is required to process the signal.

The frequency response of the 5  $\mu\text{m}$  cold wire is approximately 400 Hz [Thole, 1992]. The flow field frequency based on the momentum thickness of the separating laminar boundary layer and the free stream (inviscid core) velocity can be calculated from the Strouhal number [Ho and Huerre, 1984].

whi

FM

frec

crite

fluc

the

tem

sen

of 1

Data

obta

were

diam

aver

lowe

the s

$$St = \frac{f \theta}{\frac{U_j}{2}} \quad (4.5)$$

The Strouhal number for laminar boundary layer separation is 0.032, which results in a frequency of approximately 100 Hz for the conditions in the FMTF. Thus the cold-wire temperature sensor is capable of measuring at a frequency of more than twice the fluctuation frequency, meeting the Nyquist criterion, and capturing temperature fluctuations associated with velocity fluctuations (transport). A faster temperature sensor could be utilized to verify the dynamics measured with the 5  $\mu\text{m}$  sensor. A greater sensitivity to temperature and a faster time constant can be obtained with a smaller diameter sensor. A 2.5  $\mu\text{m}$  diameter tungsten wire has an estimated frequency response of 1200 Hz [Thole, 1992] and was incorporated to realize these improvements. Data obtained with the 2.5  $\mu\text{m}$  wire probes were indistinguishable from the data obtained with the 5  $\mu\text{m}$  wire probes. The 5  $\mu\text{m}$  probes were utilized since they were easier to manufacture and generally more robust.

The temperature profiles at  $x/w = 10.8$  were verified with a 7.6  $\mu\text{m}$  diameter micro-thermocouple. The thermocouple measured the same time-averaged temperature profile as the cold-wire sensor, but it measured a slightly lower RMS profile. The lower fluctuation measurement is most likely the result of the slower time response of the thermocouple damping out fluctuations.



non-d

respe

the te

shown

set of

layer.

to the

flat pla

from th

differe

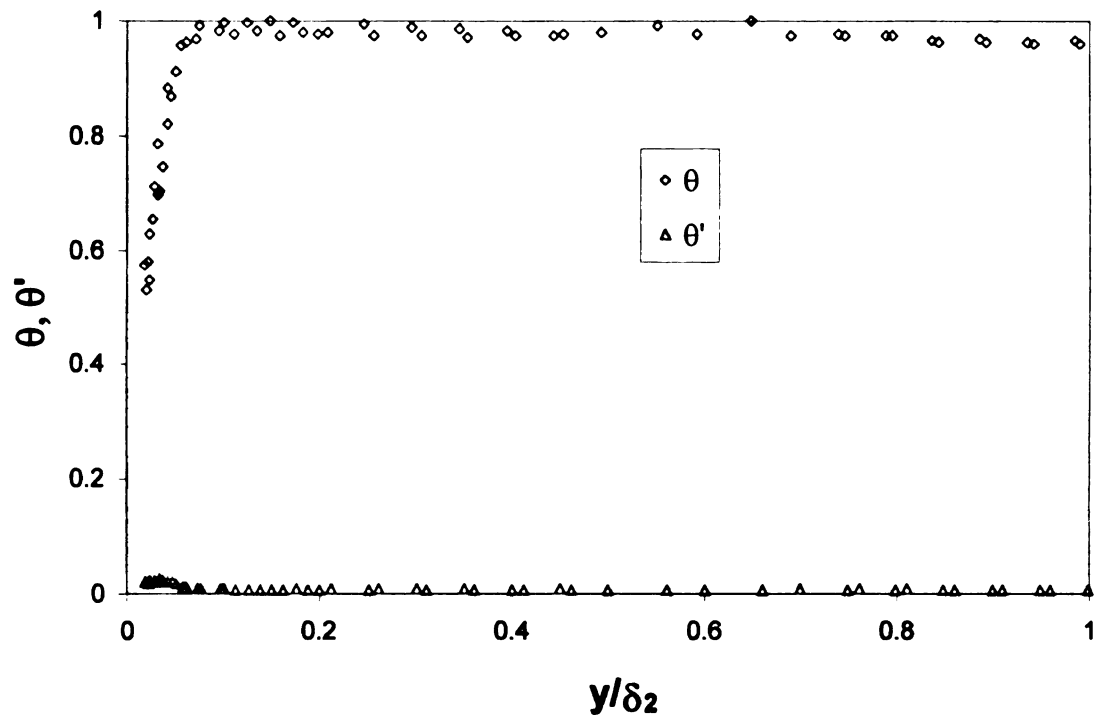
the inn

Figure 4.9 through Figure 4.12 present the cold-wire temperature data at non-dimensional streamwise locations of  $x/w = 1.59, 4.45, 7.62$  and  $10.8$ , respectively. The temperature profiles have been non-dimensionalized based on the temperature difference between the test surface ( $T_s$ ) and the jet exit ( $T_j$ ) as shown in Equations (4.6) and (4.7).

$$\theta = \frac{T - T_s}{T_j - T_s} \quad (4.6)$$

$$\theta' = \frac{T'}{T_j - T_s} \quad (4.7)$$

All the figures contain 3 data sets except Figure 4.10, which contains one set of data. The figures reveal the expected thickening of the thermal boundary layer. Other inferences based on flat plate boundary layer theory are limited due to the significant differences in the general flow features of a wall jet flow and a flat plate boundary layer flow. Specifically, the propagation of the fluctuations from the outer shear layer into the inner boundary layer represents a significant difference and results in quicker initiation of the transition to a turbulent flow in the inner boundary layer.



**Figure 4.9.** Non-dimensional temperature profile at  $x/w = 1.59$ ;  $T_s = 4^\circ\text{C}$ .

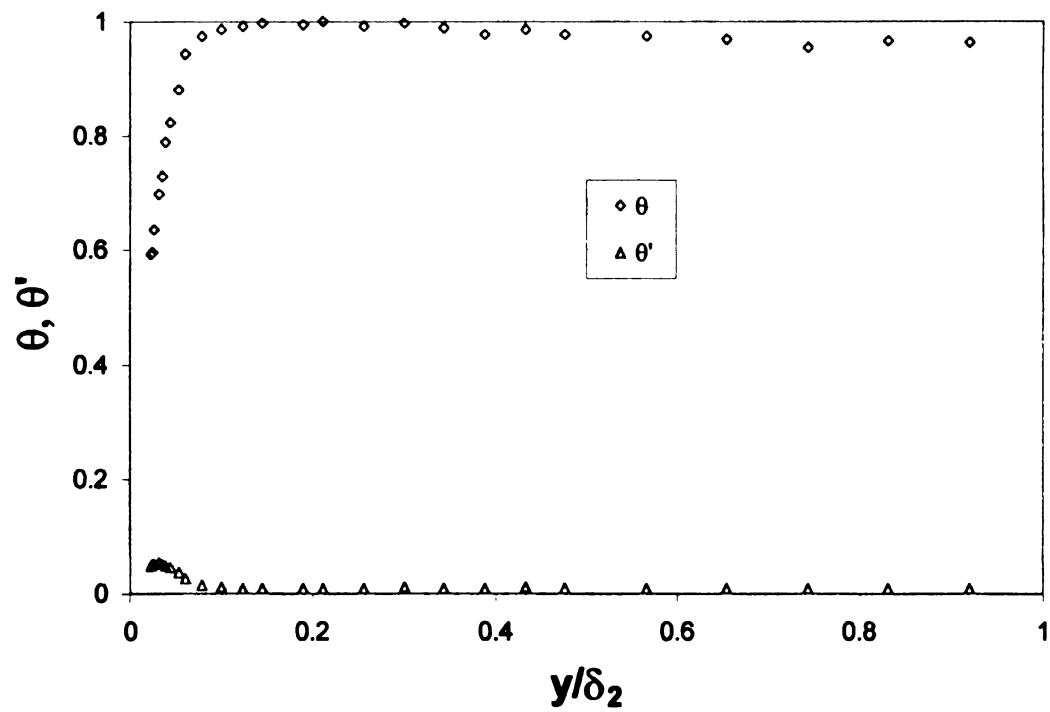


**Figure 4.10.** Non-dimensional temperature profile at  $x/w = 4.45$ ;  $T_s = 4^\circ\text{C}$ .

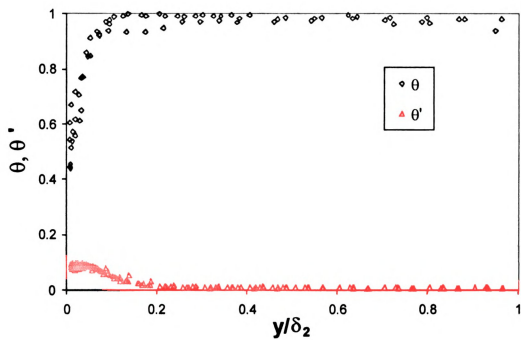


**Figure 4.11.** Temperature profile at  $x/w = 7.62$ ;  $T_s = 4^\circ\text{C}$ .

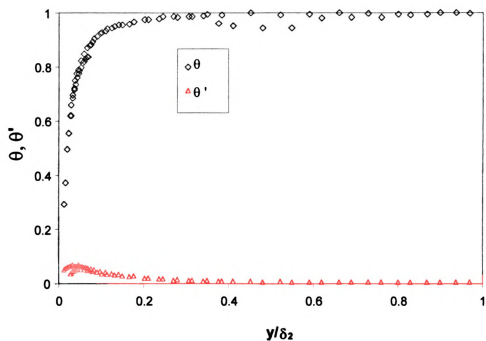


**Figure 4.12.** Temperature profile at  $x/w = 10.8$ ;  $T_s = 4^\circ\text{C}$ .

#### **4.4 SUMMARY OF EXPERIMENTAL RESULTS**

The measured velocity profiles in the non-isothermal jet are unaffected by the thermal gradients near the wall. This information was inferred from a Grashoff-Reynolds number comparison that indicated that the inertial effects were several orders of magnitude larger than the buoyancy effects. The small changes in the fluid properties associated with the temperature gradient within the thermal boundary layer also support this assumption. The comparison between the measured velocity profiles in the isothermal and the non-isothermal, non-condensing experimental flows confirm that no measurable differences exist.

The comparison of the isothermal and non-isothermal velocity data at  $x/w = 10.8$  to published data in the fully-developed, self-preserving region indicate the quality of the measurements taken. The agreement with the published, fully developed profiles provides a high level of confidence in the measurements taken in the developing region of the wall jet.

The developing region of the wall jet is of particular interest because of the similarities to the defroster/defogger flow field. Both flow fields exit from high aspect ratio openings and issue across thermally active surfaces. Actual defroster flows impinge on the surface of interest and generally have higher turbulence intensities than the flow studied here. The developing region of the wall jet is sensitive to the particular geometry of the test facility and must therefore be quantified experimentally for accurate comparisons to computational results to be performed. The velocity and temperature measurements from the FMTF provide a powerful opportunity for direct comparison of the experimental

results and the CFD predictions of the flow field. This comparison can be implemented to validate or improve the computational models utilized for practical design applications.

The excellent match of the isothermal and non-isothermal experimental velocity profiles at each  $x/w$  location indicate that the hot-wire temperature compensation in the thermal boundary layer is functioning properly. The velocity profiles from the two different experimental regimes are statistically indistinguishable. The hot-wire velocity measurement is corrected for local temperature variation with the cold-wire temperature measurement. The combination of these two probes in the boundary layer allows simultaneous measurement of the streamwise velocity, temperature and their fluctuating components. This arrangement allowed local temperature compensation for the hot-wire to improve velocity measurement accuracy. These measurements provide a useful set of benchmark data for comparison to the temperature field calculations from the CFD simulations.

The experimental data also indicate that the CFD simulations can be performed with an uncoupled methodology. This methodology refers specifically to whether the momentum and energy equations need to be solved simultaneously. The fact that the experimental velocity profile is independent of the temperature profile indicates that an uncoupled solution can be implemented. The uncoupled model is much more efficient to implement computationally.

#### **4.5 COMPARISON OF EXPERIMENTAL DATA TO CFD RESULTS**

The computational model utilized an uncoupled solution scheme. The velocity profile was solved independent of the thermal effects. This is the equivalent of solving the isothermal flow field. The isothermal velocity solution then provides the necessary information to solve the energy equation and arrive at a solution for the thermal boundary layer. This solution technique was assumed adequate since the experimental measurements indicated no measurable change in the velocity profiles (see Figure 4.2). This technique allows for the simulation to be conducted in less time. The comparisons of the velocity results are identical to the results presented in Section 3.2 and will not be repeated here.

Figures 4.13 through 4.15 present the comparison of the thermal boundary layer in the experimental facility and the computational results.

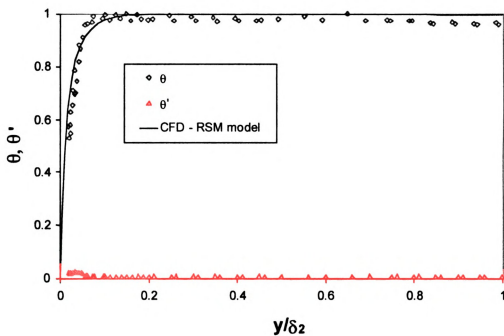


**Figure 4.13.** Comparison of the experimental and computed temperature profiles  
at  $x/w = 1.59$ ;  $T_s = 4$  °C.

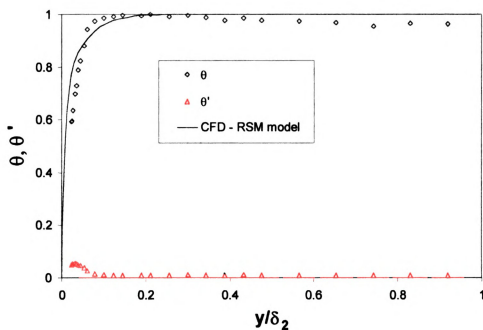


**Figure 4.14.** Comparison of the experimental and computed temperature profiles  
at  $x/w = 4.45$ ;  $T_s = 4$  °C.



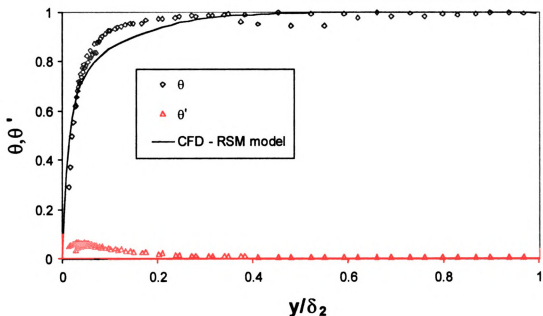


**Figure 4.15.** Comparison of the experimental and computed temperature profiles  
at  $x/w = 10.8$ ;  $T_s = 4\text{ }^{\circ}\text{C}$ .

The mean (time - averaged) temperature profiles indicate that the thermal boundary layer (as determined by  $\delta_T(x/w)$ ) in the CFD simulation thickens at a greater rate than the experimental measurements indicate. This is probably the result of the turbulence model once again and is directly coupled to the fact that the momentum boundary layer ( $\delta(x/w)$ ) thickened at a greater rate in the simulation than in the experiment. This information supports the use of a transition model to activate the turbulence model or a zonal grid structure to allow the turbulence model to be implemented at a predetermined flow location.

The mean temperature profiles at  $x/w = 1.59$  agree within the experimental uncertainty. The comparison between the experiment and the computation

continues to degrade as the boundary layers thicken at different rates as the flow progresses downstream. At  $x/w = 10.8$ , the profiles differ by approximately 8% of the maximum temperature difference (or about 1.6 °C). The temperature gradient at the test surface ( $dT/dy \big|_{y=0}$ ) is up to 61% larger in the computed result than in the experimental data. This indicates that the computational model over-predicts the heat transfer at the thermally active surface. The greater estimate of the heat transfer would lead to under-prediction of the time necessary to defrost or defog a windscreen. Federal law specifies defrosting times for passenger vehicles (FMVSS103). Successful modeling would reduce or prevent modifications to existing designs once prototype testing is initiated. The data obtained provides the opportunity to tune the computational model to agree with this model flow field and potentially improve the computational capabilities.



## **Chapter 5**

### **STEADY STATE, NON-ISOTHERMAL, CONDENSING MEASUREMENTS**

The steady state, non-isothermal, condensing regime was studied with two separate methodologies. Velocity and temperature profiles in the flow field were measured with the same techniques detailed in Chapters 3 and 4. The overall mass transfer rate to the thermally active test section was also studied. The steady state mass transfer was studied as a limiting case to determine overall system performance in the Ford-MSU test facility and to measure the time averaged and spatially averaged mass transfer coefficient on the thermally active test section. These data provide insight into the global performance of the system and established another validation data set for direct comparison to the computational work being performed at Ford Motor Company. The average mass transfer coefficient ( $h_m$ ) on the thermally active test section in the FMTF wind tunnel was measured at 0.0407 m/s for a jet Reynolds number of 13,300. This result was within 10% of the computed result obtained with non-turbulent grid zones incorporated near the jet orifice.

#### **5.1 TEMPERATURE AND VELOCITY MEASUREMENTS**

Hot-wire and cold-wire measurements in the non-isothermal, condensing flow regime were conducted. The steady state, non-isothermal, condensing experiments were conducted with the thermally active wall temperature set at approximately 4 °C and the relative humidity of the wall jet set at 50%. The

ambient temperature was approximately 24 °C ( $\pm 1$  °C) for all of the experiments. The time-averaged velocity profile is expected to agree with the isothermal velocity profile due to the small changes in the fluid properties over the temperature range utilized and the low rate of mass transfer associated with the condensation. The three experimental velocity measurements shown in Figure 5.1 bear out these expectations when compared to the ensemble average of the isothermal velocity profiles. These measurements were complicated by the presence of a thin layer of liquid H<sub>2</sub>O (the condensate) on the test surface. It is believed that this fluid destroyed the hot-wire when contact occurred. This made near wall velocity measurements difficult to obtain. However, the cold-wire was more robust than the hot-wire due to the very low overheat utilized. The cold-wire was infrequently destroyed during the experiments and was capable of obtaining temperature data closer to the test surface than the hot-wire probe.

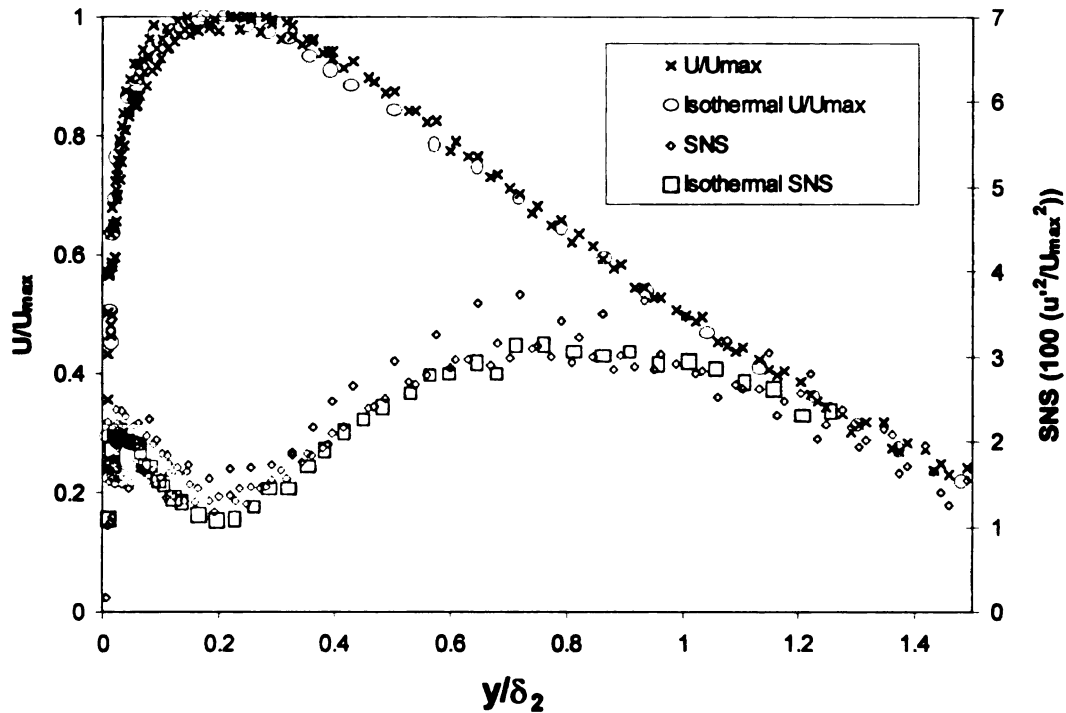


**Figure 5.1. Comparison of velocity profiles in the non-isothermal, condensing and isothermal experimental regimes.**

The temperature profiles in the flow were measured next. Results from the literature indicated that a measurable shift in the temperature profile might be present change [Legay-Desesquelles and Prunet-Foch, 1986]. The time-averaged temperature profiles presented in Figure 5.2 show a statistically significant difference in the near wall region ( $y/w < 0.03$ ) between the non-isothermal, non-condensing experiments and the non-isothermal, condensing experiments. A 95% confidence level was utilized for the null hypothesis test.

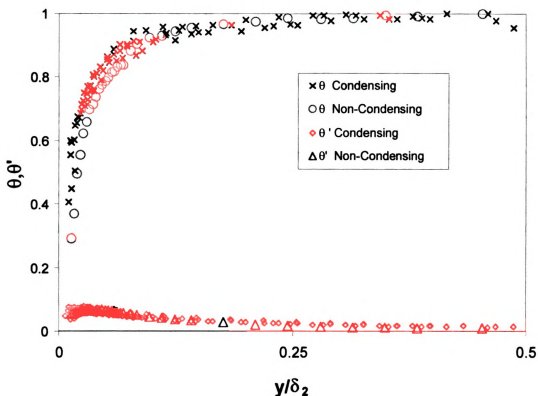


**Figure 5.2.** Comparison of temperature profiles in the condensing and non-condensing, non-isothermal experimental regimes;  $T_s = 4\text{ }^{\circ}\text{C}$ .

The effect of the latent heat release created by the condensation could be evident as an increase in the slope of the temperature profile at the wall. The temperature gradient would increase if the latent energy is released volumetrically near the wall, if mixing is improved due to the additional surface roughness created by the fluid structure, or if a portion of the latent heat is convected from instead of conducted into the test surface. The saturation temperature for the experimental conditions was computed to occur (for constant total pressure) at  $y/\delta_2$  of 0.1 ( $y \approx 450\text{ }\mu\text{m}$ ). This could result in volumetric heat

generation within a condensing vapor adjacent to the wall as the latent heat is released. The difference in the temperature data in Figure 5.2 is consistent with this assumption. However, no vapor layer was apparent during the experiments, which is consistent with Matuszkiewicz and Vernier [1991]. Matuszkiewicz and Vernier [1991] state that droplet formation in flows with  $Le < 1$  is impossible in the condensation boundary layer if the free stream droplet mass fraction is zero and the temperature gradient is small. The conditions in the FMTF flow are consistent with this specification and therefore no vapor is anticipated.

The regression curves fit to the non-isothermal, non condensing and the non-isothermal, condensing temperature measurements are statistically different for values of  $y/w$  less than 0.03 at a 95% confidence level, assuming that all the errors present are purely random. The difference was determined by comparing the confidence intervals for each regression result. The data were taken with a hot-wire/cold-wire dual probe and the experiment was terminated when the hot-wire signal indicated failure. This limited the nearest temperature measurement to the wall to be at a  $y^+$  location of approximately 10, using the isothermal shear velocity ( $U_\tau$ ). The isothermal shear velocity was utilized because it was better resolved than the non-isothermal, condensing velocity measurements and no significant difference in the velocity profiles were anticipated or detected (see Figure 5.1).

The increase in the non-isothermal, condensing temperature profile is consistent with predicted and observed trends in the literature for convective flows with phase change [Legay-Desesquelles and Prunet-Foch, 1986]. The



addition of mass transfer to the flow increases the effective heat transfer and thus raises the effective Nusselt number. This alteration of the heat transfer directly impacts the temperature profile in the flow. The surface temperature was maintained at a constant value. However, the heat flux into the surface was not measured during these experiments. Verification of the offset could be investigated by installing a heat flux meter in the test surface and comparing the change in the heat flux conducted into the surface to the total quantity of mass condensing (and thus the total latent heat released) on the surface. The difference in the heat flux into the thermally active test surface and the total latent heat released would represent the total additional heat flux convected away by the wall jet flow field.

## **5.2 STEADY STATE MASS TRANSFER MEASUREMENTS**

Steady-state condensation measurements were conducted by collecting the fluid draining from the bottom edge of the thermally active test section. The thermally active test section is aligned vertically to allow the fluid to flow off during experiments (see Figure 2.2, item 9 and Figure 5.3). The collection and measurement system utilized to measure the steady state condensation rate is presented in Figure 5.3 [Kinnen, 2000]. A funnel with a narrow inlet was attached to the lower edge of the thermally active test section. A beaker was constructed with a narrow inlet to collect and contain the condensate. The beaker provided 3 narrow slits for the airflow to escape. This arrangement was chosen to minimize the possible evaporation of the condensate collected. Tests

were also conducted with no active condensation occurring on the test section to measure the quantity of fluid evaporating from the beaker. Flow humidity levels were varied throughout the experimental range during the evaporation tests. The steady state condensation measurements were corrected for evaporation based on these results. The correction for the evaporative losses was of the order of 5 to 10% of the total condensate volumes and was a linear function of the concentration difference as expected.

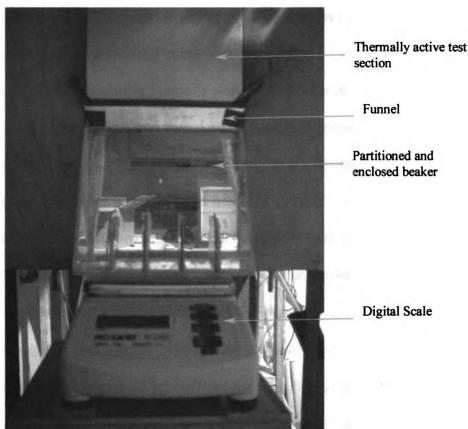


**Figure 5.3.** Steady state condensation - collection and measurement system.

The mass of the condensate in the beaker was recorded with an electronic scale with an RS-232 output linked to a PC. The experiment was allowed to equilibrate for at least 30 minutes before data acquisition was initiated. Data were acquired for 30 minutes and then the total mass transfer rate was calculated. The mass accumulation data as a function of time were fit with a linear regression model. The results were highly linear with  $r^2 = 0.98$  or larger.

The experimental results and numerical steady-state condensation predictions are presented in Figure 5.4. The data are plotted as the total condensation rate to the thermally active test section (grams/min) as a function of the concentration difference in the flow field ( $\text{kg/m}^3$ ). The concentration difference is based on the humidity and temperature at the exit of the two dimensional contraction and the average surface temperature at the centerline of the thermally active test section. Note that the presence of the condensate layer was calculated to have a negligible effect ( $< 0.01\text{ }^\circ\text{C}$ ) on the accuracy of the thermocouple measurements. This is consistent with the literature, which indicates that the interface and surface temperature may be expected to be the same for flows with specific humidities ( $\omega$ ) less than  $0.1\text{ kg H}_2\text{O/ kg air}$  [Matuszkiewicz and Vernier, 1991]. The specific humidity in the experimental flow was always less than  $0.02\text{ kg H}_2\text{O/ kg air}$ . The computational results were provided by Dr. B. AbdulNour (Ford Motor Company) and were computed with Fluent 5<sup>®</sup> with a user defined function (UDF) incorporated into the software. The

UDF utilized the calculated concentration gradient at the wall and Fick's law to calculate the mass transfer to the surface.

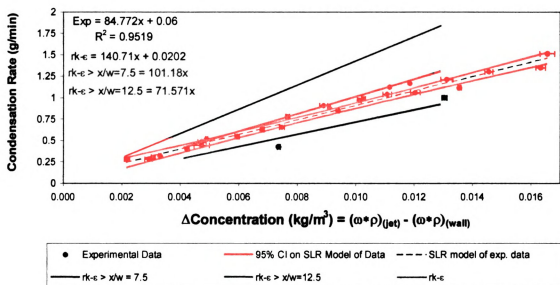


**Figure. 5.4.** Comparison of the experimental and computed steady-state condensation results.

These results were published in Hoke et al. [2000]. The slope of the predicted condensation rate, with the turbulence model active in the entire flow field, is 55% larger than the measurement results. The numerical simulation assumes that the flow is turbulent throughout the flow field. The experimental measurements show a laminar-like, Blasius velocity profile at the jet exit. Mabuchi and Kumada [1972] show a 45% increase in the average mass transfer

coefficient between a wall jet with an laminar to turbulent transition and a wall jet with an fully turbulent initial boundary layer. This is indicative that the difference between the experiment and the CFD results may be caused by the turbulence model utilized in the entire flow field simulation.

The numerical model was modified as recommended in Chapter 2 to incorporate zones where the turbulence model could be turned on and off to simulate the effects of the laminar to turbulent transition. The experimental velocity measurements of the inner boundary layer indicate that the transition region begins before  $x/w = 5$ . This estimate is based on the sharp rise in the streamwise normal stress in the inner boundary layer that begins to become pronounced at  $x/w = 4.45$ . Two simulations were conducted where the transition location was set at  $x/w = 7.5$  and  $12.5$ , respectively [Chui, 2000]. The results from these simulations bracket the experimental results and are shown in Figure 5.4.

The slope of the condensation rate measured experimentally is  $84.7 \text{ g/min}/(\text{kg/m}^3)$  or  $0.0014 \text{ m}^3/\text{s}$ . Note that dividing this parameter by the thermally active test surface area ( $0.045 \text{ m}^2$ ) yields results for the mass transfer coefficient in more usual dimensions of  $\text{m/s}$ , producing  $h_m = 0.031 \text{ m/s}$ . Measurements of the test surface temperature by AbdulNour et al. [1997] have shown that the edges of the thermal test surface are significantly effected by conduction to the splitter plate and that only 80% of the thermally active test surface could be considered isothermal. The center of the thermally active test surface was reported to be isothermal to within  $1^\circ\text{C}$  [AbdulNour, et al., 1997]. Temperature measurements of the thermally active test section were conducted with the

infrared camera and are presented in Figure 5.5. The measurements were conducted with the thermally active test surface heated to avoid complications with condensation on the surface. The condensation on the surface could create larger temperature variations on the surface; however, the heat flux associated with the mass transfer in a typical experiment is less than 20 W. This flux was estimated to effect the surface temperature by less than 1 °C at any location. Note that the circulating bath is capable of 500 W of cooling.

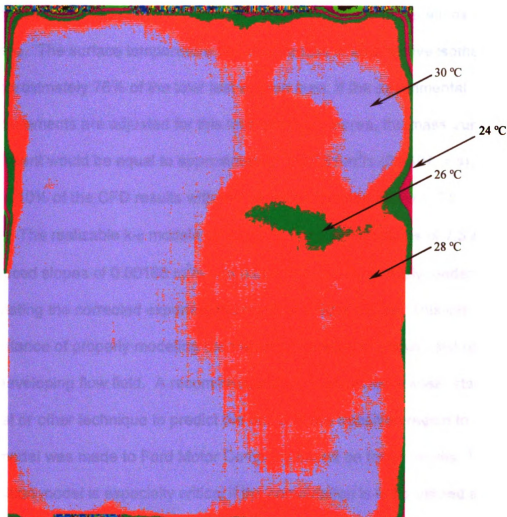


**Figure 5.5.** Temperature variation on the thermally active test section for a constant temperature circulating bath temperature of 34 °C.

Based on the results presented in Figure 5.5, it is expected that the edges of the thermally active test section are 5 to 6 °C warmer than the center during the condensation experiments. This temperature variation would reduce the concentration difference by approximately 60 to 80% compared to the center of the test section in a typical experiment. The thermal flux from the higher

condensation rates is expected to create larger temperature variations on the surface. The surface temperature variation results in an effective isothermal area of approximately 76% of the total test section area. If the experimental measurements are adjusted for this loss of effective area, the mass transfer coefficient would be equal to approximately  $0.00181 \text{ m}^3/\text{s}$  ( $0.0407 \text{ m/s}$ ), which is within 10% of the CFD results with the transition location at  $x/w = 7.5$ .

The realizable  $k-\epsilon$  models utilizing the transition locations of 7.5 and 12.5 produced slopes of  $0.00168 \text{ m}^3/\text{s}$  and  $0.00119 \text{ m}^3/\text{s}$  respectively, under-estimating the corrected experimental result of  $0.00181 \text{ m}^3/\text{s}$ . This indicates the importance of properly modeling the transition location to obtain valid results in the developing flow field. A recommendation to incorporate a linear stability model or other technique to predict the onset of the transition region to improve the model was made to Ford Motor Company based on these results. The transition model is especially critical if the computation is to be utilized as a design tool in similar flow fields since an experimental prototype may not be feasible/available. The  $x/w$  locations of 7.5 and 12.5 for the transition zones were chosen based on the experimental velocity measurements and the test surface geometry. Also note that the transition region in the experiment is expected to begin before  $x/w = 5$ . Recall that transition does not occur at sharply demarcated boundary

The spatial average of the Sherwood number ( $h_m w / D$ ) over the thermally active test surface can be determined from the steady-state condensation measurements by calculating an average mass transfer coefficient from the slope



of the results in Figure 5.4. Local information cannot be obtained from the steady-state experiments since the data measured are of the mass transfer to the entire surface. These experimental and computational average results are compared in Figure 5.6. to averages taken from data published by Mabuchi and Kumada [1972]. The results from Mabuchi and Kumada are referenced as M&K in the figure along with a descriptor indicating the jet Reynolds number ( $U_j w / \nu$ ) in the experiment. The average Sherwood number results from the experimental data were corrected for the effect of the temperature variation on the test surface as previously explained. Note that the data from Mabuchi and Kumada [1972] is representative of much of the data in the literature such as Akfirat [1966].

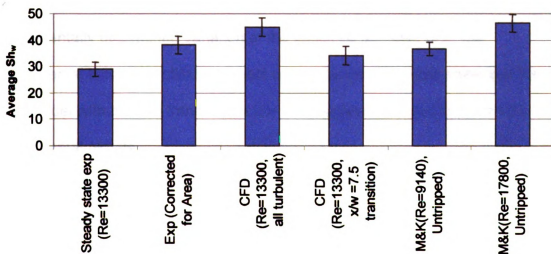


**Figure 5.6.** Average, steady-state Sherwood number comparison for the experimental, computational, and published results.

Utilizing linear interpolation to obtain an estimate for  $Re_w = 13,300$  based on the untripped results published by Mabuchi and Kumada [1972] provides an estimate of  $Sh_w = 41$ . The area-corrected steady state condensation results ( $Sh_w = 38.2 \pm 3.4$ ) presented in Figure 5.6 agree with the expected results extrapolated from the data published by Mabuchi and Kumada [1972] to within the 95% confidence region. This indicates that the flow may be undergoing transition similar to that indicated by the published results.

The variation in the simulation results indicates the sensitivity of the CFD mass transfer calculations to the location of the inner boundary layer transition to turbulent flow. The "error bars" on the CFD result reflect the difference between the predictions obtained with the RSM and the  $k-\epsilon$  turbulence models. The uncertainty indicated by the "error bars" on the other results are the experimentally determined variation of the specified uncertainty of the experimental technique utilized. Direct comparisons of the data show that the CFD model with a zonal transition at  $x/w = 7.5$  agrees to within 10% with the experimental results.

Comparison of the velocity and temperature gradients at the thermally active test surface as discussed in Chapters 3, 4, and 5 could also explain the discrepancy between the CFD model and the experimental results. Tables 5.1 and 5.2 contain the comparison between the velocity and temperature gradients measured and calculated at the thermally active wall surface.

**Table 5.1.** Comparison of experimental and computed velocity gradients at the thermally active surface.

Experimental Ensemble results			CFD Results RSM model k-ε			% Variation CFD from Exp.	
x/w	dU/dy <sub>0</sub> (1/s)	r <sup>2</sup>	x/w	dU/dy <sub>0</sub> (1/s)	dU/dy <sub>0</sub> (1/s)	x/w	% Variation
0	11132	0.84	0	22193	22832	0	105.1
1.59	10595	0.90	1.59	22270	21315	1.59	101.2
3.18	12268	0.94	3.18	21827	20213	3.18	64.8
4.45	9390	0.86	4.45	21420	19576	4.45	108.5
7.68	12179	0.87	7.68	20490	18472	7.68	51.7
10.8	14534	0.81	10.8	20134	18208	10.8	25.3

**Table 5.2.** Comparison of experimental and computed temperature gradients at the thermally active surface.

Experimental Ensemble results			CFD Results RSM model k-ε			% Variation CFD from Exp.	
x/w	dT/dy <sub>0</sub> (°C/m)	r <sup>2</sup>	x/w	dT/dy <sub>0</sub> (°C/m)	dT/dy <sub>0</sub> (°C/m)	x/w	% Variation
1.59	16123	0.96	1.59	42671	41303	1.59	156.2
4.45	22450	0.98	4.45	36226	30150	4.45	34.3
7.68	20000	0.92	7.68	33067	27739	7.68	38.7
10.8	16147	0.98	10.8	31224	26451	10.8	63.8

The CFD model consistently results in larger velocity and temperature gradients at the wall surface. The % variation in Tables 5.1 and 5.2 is defined as the 100 times the difference between the CFD and the experimental results divided by experimental result.

The over-prediction in the wall gradients by the CFD model is probably also responsible for the over-estimation of the steady state mass transfer rate. The transition region should begin before  $x/w = 7.62$  based on the experimentally measured increase in the streamwise normal stress profile in the inner boundary layer. Correcting the wall gradient prediction should lower the overall mass transfer calculation result and allow the zonal turbulence model transition location to better reflect the experimentally determined position.

## **Chapter 6**

### **OPTICAL MEASUREMENT OF TRANSIENT MASS TRANSFER UTILIZING INFRARED THERMOGRAPHY**

**A non-contacting, optical measurement technique was sought that could be utilized to obtain transient mass transfer measurements on a surface in convective flow applications. A non-contacting, optical technique is highly desirable since no probes or sensors are added to the flow or surface under interrogation. Presence of a probe or sensor can create experimental artifacts effecting the results. Additionally, infrared wavelengths were utilized to obtain a high degree of sensitivity due to the spectral absorptivity characteristics of liquid water. There is evidence in the literature that the presence of liquid water and other liquids are detectable with infrared sensors [Bearman et al. 1998, Pekemir and Davies, 1999].**

**Utilizing thermographic reflectance measurements to measure local condensate thickness is based on the absorptivity of the condensate. Figure 6.1 presents a model schematic of a uniform thin film of water on a reflective surface. This figure greatly simplifies the actual experimental conditions but it does demonstrate a theoretical basis for the technique. The condensate surface observed in the experiment is more complex than the thin film assumed in the model and appeared to consist of a film mixed with randomly distributed droplet-like structures. For long enough times, these droplets eventually coalesced into larger droplets in the tests in the FMTF and flowed off the thermally active test section.**

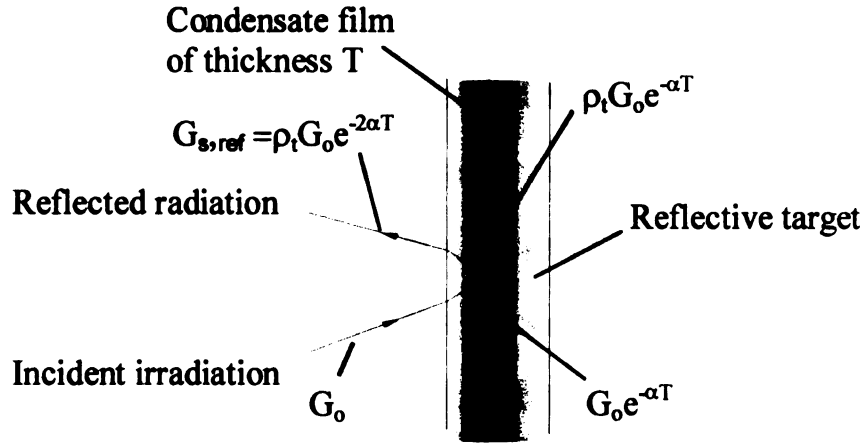


**Figure 6.1. Thin film absorption model**

In this model, the incident irradiation ( $G_o$ ) would be absorbed by the condensate film over two thicknesses as it was reflected from the target surface. The quantity of energy absorbed is an exponential function and is dependent on the absorptivity ( $\alpha$ ) and the thickness ( $T$ ) of the condensate. Note that the angles of incidence in Figure 6.1 are exaggerated for illustrative purposes. The actual experiment utilizes illumination and viewing angles nearly perpendicular to the target surface. A simple analysis of the physical situation presented in Figure 6.1 would result in the reflectance of the sample with a thin condensate film being calculated as

$$\rho_s = \frac{G_{s,ref}}{G_o} = \frac{\rho_t G_o e^{-2\alpha T}}{G_o} \quad (6.1)$$



In principle, Equation (6.1) could be solved for the condensate thickness (T). A complication arises from the fact that the intensity of the reflected energy cannot be measured directly. The infrared camera is only capable of measuring the radiosity (J) from the target surface, which includes emitted and reflected energy (the targets utilized are opaque). However, the reflectance can be obtained by measuring the total radiation from the surface when the target is independently illuminated by two sources, A and B, with different intensities [Inframetrics, 1988]. The emitted energy from sources A and B must also be measured directly. Assuming that the target surface temperature is the same in both measurements, then  $(\epsilon_s \sigma T^4)_A = (\epsilon_s \sigma T^4)_B$ . Subtracting the two measurements eliminates the emitted radiation from the image data. The target reflectance can then be calculated by

$$\begin{aligned} \rho_s &= \frac{J_{sA} - J_{sB}}{J_{mA} - J_{mB}} = \frac{\rho_s G_A + (\epsilon_s \sigma T^4)_A - \rho_s G_B + (\epsilon_s \sigma T^4)_B}{\rho_m G_A + (\epsilon_m \sigma T_m^4)_A - \rho_m G_B + (\epsilon_m \sigma T_m^4)_B} = \\ &= \frac{\rho_s G_A - \rho_s G_B}{\rho_m G_A - \rho_m G_B} = \frac{\rho_s G_A}{\rho_m G_A} = \frac{\rho_s G_B}{\rho_m G_B} \end{aligned} \quad (6.2)$$

Note that the reflectivity of the mirror ( $\rho_m$ ) was determined to be ~0.97. If the reflectance of the aluminum target and the intensity of the irradiation (G) from the two illumination sources are assumed to be constant, the thickness can be calculated from the following ratio



$$\ln\left(\frac{\rho_{sf}}{\rho_{so}}\right) = \ln\left(\frac{\frac{\rho_s G_f e^{-2\alpha T}}{G_f}}{\frac{\rho_s G_o}{G_o}}\right) = -2\alpha T. \quad (6.3)$$

The sensitivity of the optical reflectance method was explored based on this thin film model. The dynamic range of the technique is expected to be dependent on the wavelength of infrared radiation utilized and the sensitivity and resolution of the optical system used. The IR camera utilized, an Inframetrics Inc. model 600L, has an 8 bit detector sensitive to wavelengths between 8 to 12  $\mu\text{m}$ . The average absorptivity of liquid water in this spectrum range is approximately  $1300 \text{ cm}^{-1}$  [Modest, 1993]. The 8 bit range limits the useful sensitivity in the low reflectance range and defines the measurement resolution obtained with the current equipment. It was expected that the reflectivity could be accurately determined to approximately 0.1 before the signal to noise ratio became untenable. Equation (6.1) was utilized to determine the response of the IR system to condensate accumulation on aluminum targets to estimate the maximum thickness measurable with the experimental equipment available. The results of this analysis are presented in Figure 6.2. The typical aluminum sample reflectance of 0.7 was utilized in the calculation.

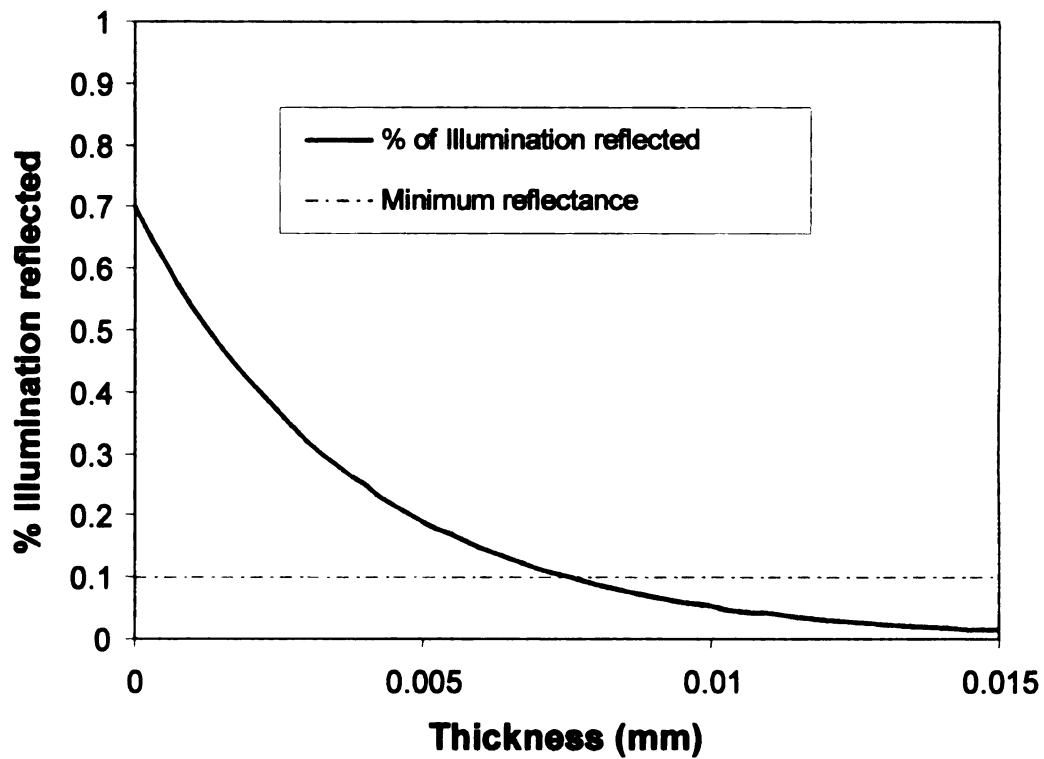


**Figure 6.2.** Thin film model results of the Inframetrics 600L sensitivity.

The results presented in Figure 6.2 indicate that the useful dynamic range of the optical condensate measurement technique developed with the equipment available would be limited to a maximum thickness measurement of approximately 7 to 8  $\mu\text{m}$ . Thus the technique is highly sensitive to initial condensate development but has a limited dynamic range.

The relation determined experimentally is not as simple as the thin film model indicates. However, this log relation provides a useful linearization of the data [Hoke et al., 2000]. The experimental results differ significantly from the thin film model predictions because the condensate does not develop as a uniform

thin film but is observed to be a mixture of film and droplets as shown in Figure 6.3.

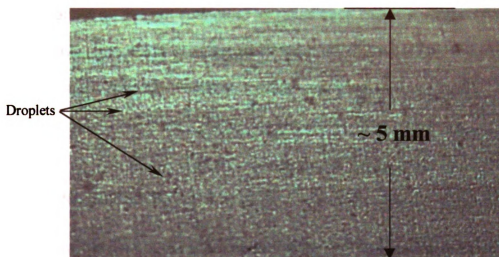


**Figure 6.3.** Structure of the condensate formation on the thermally active test section.

The droplets seen in Figure 6.3 scatter and absorb light differently than a thin film and the optical path length through the condensate would not be uniform across a droplet on the target surface. Due to these effects, an empirical relation was sought between the reflectance measurement and the thickness of the condensate present.

Individually characterizing the droplets is not necessary due to the optical properties of the infrared system utilized. The infrared camera obtains a digital image of the surface and each pixel of the image is an integrated average of an



area of the surface observed. The Inframetrics 600L long wave camera utilized for these experiments integrates over a length scale of 0.67 mm to 1.19 mm for viewing distances of 336.5 mm and 616 mm respectively [Inframetrics, 1988]. This is approximately one to two orders of magnitude larger than the largest droplets observed on the test surface. The reflectance calibration presented here takes advantage of this area integration and assumes a stationary droplet distribution in each optically integrated measurement area (optical pixel).

## **6.1 EXPERIMENTAL METHODS**

The development of the experimental technique required four phases. The first phase developed an independent methodology to measure the trace amounts of water on the calibration target surfaces. The second phase consisted of calibrating the IR camera measurement of the surface reflectance as a function of the condensate present on the test samples. The effects of viewing angle and distance were also tested during the second phase. The third step involved validation of the technique under conditions where non-uniform condensate thicknesses were expected on the aluminum calibration targets. The fourth and final step involved quantifying the error present in the method, examining the limitations and establishing the accuracy of the technique.

### **6.1.1 MEASUREMENT OF TRACE CONDENSATE UTILIZING HS-C-GC-FID**

The spectral sensitivity of the infrared camera utilized limits the estimated maximum dynamic range of the optical thickness measurement to approximately 8  $\mu\text{m}$ . This estimate is based on the thin film model. This is the equivalent of having 0.8  $\mu\text{g}$  of condensate per square centimeter of target surface area.

Conventional techniques for water measurement such as gravimetric or titration techniques were not suitable for a quantity this small. Furthermore, since the target is cooled below the ambient dew-point, the calibration target must also be isolated quickly to prevent additional condensation or evaporation. Simply moving the target to a secondary measurement location without isolating it from the environment could cause significant measurement error. An error estimate in the condensation measurement based on the target temperature and an ambient humidity of 50% Rh was calculated from a simple energy balance between the internal energy of the target and the latent energy of condensation or evaporation. This first order estimate was calculated with

$$(mc_p \Delta T)_{\text{aluminum}} = (mL)_{\text{condensate}} \quad (6.4)$$

This would result in a 1% error in the mass measurement from additional condensation. This result indicates that further condensation is not of critical importance. However, a more significant problem is evaporation of the condensate from the target. Visual observation of the wetted aluminum targets

indicates that exposure to dry ambient air can remove a significant amount of the condensate from the target.

An indirect measurement technique for the measurement of trace quantities of water using head-space, capillary, gas chromatography (HS-C-GC) was developed by Loconto et al. [1996] based on the work of Loeper and Grob [1988]. In this method, a sample containing an unknown quantity of water (H<sub>2</sub>O) is added to a head-space vial. A stoichiometric excess of calcium carbide (CaC<sub>2</sub>) is added and the vial is quickly sealed. The calcium carbide reacts with the water in the vial and produces acetylene (C<sub>2</sub>H<sub>2</sub>) and calcium hydroxide (Ca(OH)<sub>2</sub>) according to Equation (6.5) [Noller, C., 1966].



The acetylene gas can be detected with the headspace, capillary, gas chromatography system utilizing a flame-ionization detector (HS-C-GC-FID) and measured with a high degree of accuracy. The HS-C-GC-FID system must be calibrated against samples with known quantities of water in order to be utilized as an effective measurement method.

All the materials and hardware utilized for the HS-C-GC-FID calibration were prepared as if they were to be utilized in the condensation experiment. The headspace vials were cleaned with de-ionized water and hydrochloric acid solution and then rinsed with de-ionized water and acetone. The headspace vials were dried in an oven at 110 °C for 24 hours and then stored in a desiccator

for later use. This treatment provided clean vials with a low measured blank level that was repeatable.

Aluminum test targets (10 mm x 32 mm x 0.8 mm) were polished with a fiber-free pad, cleaned with acetone and allowed to soak in the ambient atmosphere for at least one hour. To prevent deviation from the actual testing conditions and methods, a dry aluminum test target was added to each vial to account for any effect the aluminum may have on the chemical reaction or the acetylene concentration levels. Each sample (including the controls) included an aluminum target.

Two different methods for adding trace water were utilized. Initially, a solution of water dissolved in a polar organic compound was utilized. Solutions of 10,000 parts per million (ppm) of water in methyl tert-butyl ether (MTBE) were prepared. These solutions were delivered to headspace vials with a glass liquid handling syringe. Calcium carbide was added and the vials were sealed and shaken to insure that physical contact occurred between the water and the calcium carbide. The specimens were then stored for 24 hours at ~10 °C. The samples were analyzed by sampling the headspace of each 22 mL HS vial using a 100 µL Pressure-Lok<sup>®</sup> gas-tight syringe (Precision Sampling, Inc.). The headspace sample was then injected in to a Autosystem<sup>®</sup> GC (Perkin-Elmer). The analog output from the C-GC-FID was connected to a PC via a 600<sup>®</sup> interface (PE-Nelson). The PC used Turbochrom<sup>®</sup> (PE Nelson) software for chromatographic data acquisition and data reduction. The control settings for the



HS-C-GC-FID are presented in Appendix C. The output was utilized to calibrate the GC-FID system.

The calibration was verified by adding water directly to the 22 mL headspace vials with 20  $\mu$ L Pipetman [Gilson]. It was found that the two calibrations did not agree within the margin of error expected. Initially, the accuracy of the direct H<sub>2</sub>O addition was suspect due the difficulty of precisely delivering aliquots of less than 5  $\mu$ L of H<sub>2</sub>O into the vials.

The density of H<sub>2</sub>O at ambient temperature is  $\sim 1\text{mg}/\mu\text{L}$ . The use of conventional 22 mL HS vials for calibration was abandoned since it is experimentally difficult to transfer from 0.5 to 3  $\mu$ L aliquots of H<sub>2</sub>O precisely using liquid handling glass syringes. Use of 125 mL HS vials with crimp tops enabled the volume of H<sub>2</sub>O to be increased by a factor of 125/22 or 5.68 while maintaining the concentration of H<sub>2</sub>O at the level that would be found if the more conventional 22 mL HS vials were utilized.

A new calibration was then conducted by scaling up the entire process to reduce the experimental difficulties with delivering small volumes of water. The following procedure was utilized to calibrate the HS-C-GC-FID: 5.68, 11.36 and 17.04  $\mu$ L of H<sub>2</sub>O were added to each 125 mL vial with a 20  $\mu$ L Pipetman<sup>®</sup> (Gilson). Note that these volumes produce C<sub>2</sub>H<sub>2</sub> concentrations equivalent to 1, 2 and 3  $\mu$ L of H<sub>2</sub>O in a 22 mL HS vial. A stoichiometric excess of calcium carbide was then added and each vial was immediately sealed and shaken vigorously on a VWR vortex mixer [model K-550-G]. The specimens were then stored for 24 hours at  $\sim 10^\circ\text{C}$ . Three controls were prepared for each calibration run to

establish a baseline. The controls consisted of an aluminum target and calcium carbide, but no H<sub>2</sub>O.

The samples were analyzed in an identical manner as before. First, the headspace of each 125 mL HS vial was sampled using a 100  $\mu$ L Pressure-Lok<sup>®</sup> gas-tight syringe and the sample injected into an Autosystem<sup>®</sup> GC. The analog output from the GC-FID was recorded with a PC using the 600<sup>®</sup> interface. The PC used Turbochrom<sup>®</sup> for chromatographic data acquisition and data reduction. The peak area measurement was obtained and the control average subtracted from each run. The control subtraction was performed to eliminate the effect of variable atmospheric humidity levels between test dates. A typical chromatographic result is presented in Figure 6.4

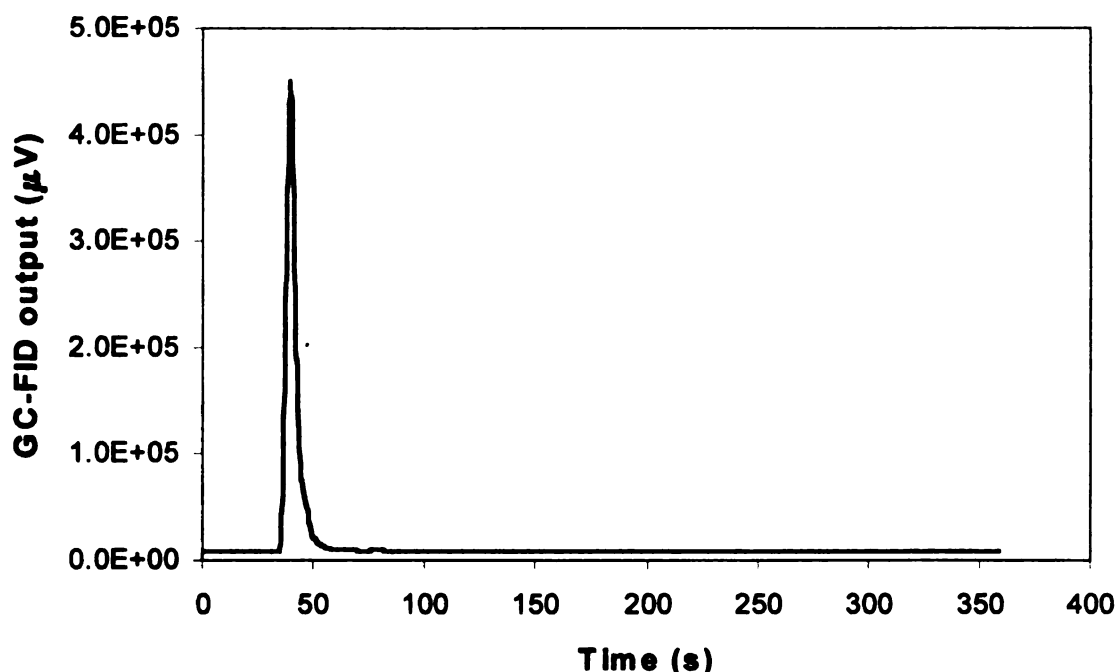


**Figure 6.4.** Typical chromatogram obtained during HS-C-GC-FID calibration.

The results of the scaled up calibration agreed with the direct H<sub>2</sub>O method in the 22 mL vials within the margin of error but the results did not agree with those obtained from the technique utilizing the H<sub>2</sub>O / MTBE solution. The highest confidence is placed in the scaled up calibration method since it introduces the fewest unknowns. The potential causes for error in the H<sub>2</sub>O / MTBE solution calibration method include the solubility of the acetylene in the MTBE and incomplete reaction of the CaC<sub>2</sub> with the H<sub>2</sub>O when in the MTBE solution. Research into the exact nature of the difference between the calibration techniques was not conducted. The actual IR- H<sub>2</sub>O calibration experiments contain only H<sub>2</sub>O and since the effect of the MTBE in calibration samples could not be easily quantified, the H<sub>2</sub>O / MTBE methodology was discarded.

The success of the scaled up calibration technique is based on the measurement characteristics of the flame-ionization detector. The FID is sensitive to the total number of carbon atoms injected into the detector, thus it is sensitive to mass not concentration [Skoog and Leary, 1992]. Since a volume of headspace gas is injected, the total mass injected is directly dependent on the concentration of carbon (C<sub>2</sub>H<sub>2</sub> in this procedure) in the measurement volume. The concentration of the C<sub>2</sub>H<sub>2</sub> depends on the initial volume of air and the total mass of water present prior to the conversion reaction. If the headspace vial volume and the quantity of water are increased by the same ratio, identical concentrations of C<sub>2</sub>H<sub>2</sub> per unit volume are produced.

The HS-C-GC-FID system utilized in these tests was being used for other experiments while these tests were conducted. The instrument is sensitive to

numerous settings including the hydrogen and air gas pressure settings. Due to the imprecise control of several of the system inputs, new calibrations were conducted with every experiment to compensate for drift of the HS-C-GC-FID system. A typical calibration of the HS-C-GC-FID system is presented in Figure 6.5.

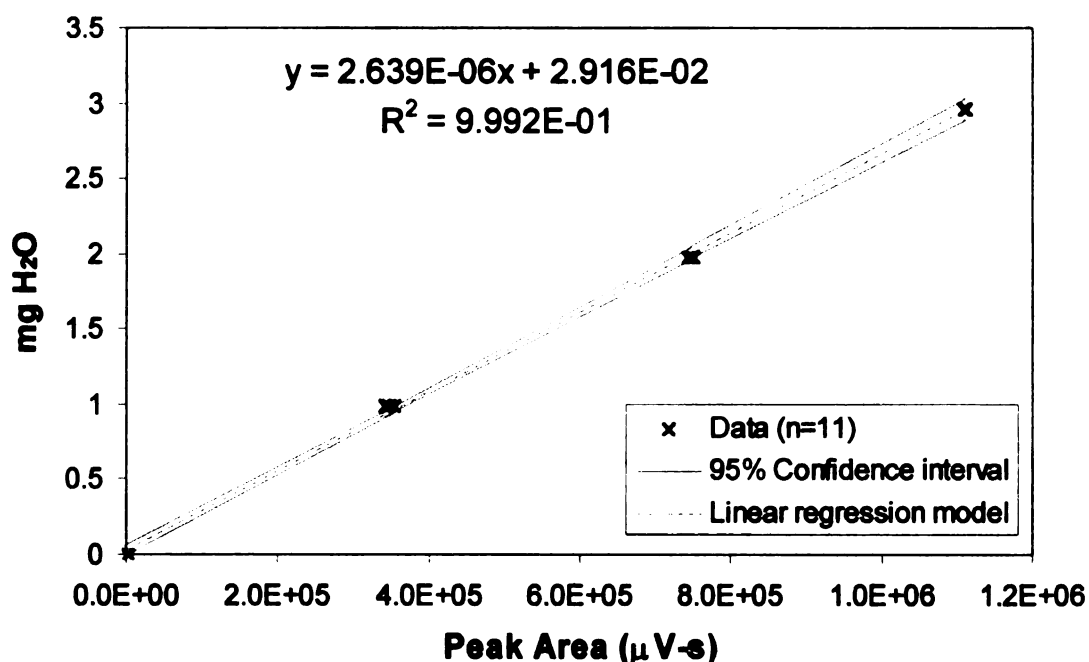


**Figure 6.5.** Typical calibration result for GC-FID system response to the volume of water added. (n = 11 calibration samples).

The result presented in Figure 6.5 can be utilized to measure the volume of water present in an unknown sample. This measurement has a 95% confidence region indicated by the solid red lines in Figure 6.5. The 95% confidence intervals range from  $\pm 46 \mu\text{g}$  at 0 mg,  $\pm 21 \mu\text{g}$  at 2 mg to the maximum deviation of  $\pm 38 \mu\text{g}$  at 3 mg. Typically, the range from 0 to 2 mg was sufficient to encompass the range of condensate mass deposited on the aluminum targets utilized in the empirical calibration presented here. Note that the calibration relation is often formatted with the axes reversed, this causes a negligibly small change in the confidence region and is essentially equivalent to the presentation here.

This result provides an independent means to determine the mass (and therefore, volume) of water present on an optical calibration target. An experiment to calibrate the infrared camera response to local condensate thickness was designed such that the optical targets could be easily captured in the 22 mL headspace vials necessary for the gas chromatography technique to be utilized.

An investigation of other methods to measure the condensate on the aluminum target surface was conducted. These included Nuclear Magnetic Resonance (NMR), Magnetic Resonance Imaging (MRI) technology, laser speckle methods, and shadow moire techniques. The NMR and MRI technologies present the opportunity for very fine measurements of the water present, but cannot be utilized on metal surfaces [Gregory, 1997]. It also doesn't

allow sample isolation and there is limited access to this type of equipment due to its cost and operating expense.

Laser measurement methods were also investigated. Laser speckle techniques can provide very accurate in-plane displacement measurements but are not very sensitive to out of plane motion [Cloud, 1998]. Independent validation (calibration) would also be necessary if this method were utilized to calculate condensate volumes on the surface. Local measurements of fluid thickness during condensation are also possible with laser interferometry. However, the limitations of this measurement are that it only provides information along the fringe lines and has a minimum thickness capability of approximately 100  $\mu\text{m}$  [Schlesinger et al., 1986]. Thus neither of these techniques are applicable for the range of the experiments conducted here.

The shadow moiré technique was also investigated. This technique projects a moiré or shadow grid pattern on the surface of interest. Changes in the geometry of the surface can then be measured by monitoring changes in the pattern [Cloud 1998]. The resolution necessary to obtain reasonable measurements of the condensate pattern is not feasible with visible light thus requiring expensive optics and detectors. Data reduction with this technique would also be very complicated and would require external validation/calibration. Based on these findings, the HS-C-GC-FID technique was adopted for trace water measurement to calibrate the infrared reflectance response.

### **6.1.2 CALIBRATION OF THE SURFACE REFLECTIVITY AS A FUNCTION OF CONDENSATE THICKNESS**

**An experiment was developed to quantify the change in the reflectivity of the aluminum test surface with the volume of condensate present. The intent was to develop an empirical relationship based on the local change in the reflectance that could be utilized to provide an optically based measurement of the condensate thickness as a function of position and time. The result of this measurement could then be utilized to calculate the local mass transfer rate or, if the free stream concentration could be measured or was known and thermodynamic equilibrium assumed at the surface, a local mass transfer coefficient. Since this technique would not rely on mechanical or chemical alterations of the surface and could be applied in any situation where optical access is available, artifact-free measurements of transient mass transfer coefficients would be possible.**

**Aluminum was chosen as the test surface due to its relatively high reflectance (typically 0.60 to 0.70 as prepared), high thermal conductivity, low thermal capacitance, and wide applicability in heat transfer devices. The high reflectivity simplified the measurements since more of the dynamic range of the Inframetrics 600L infrared camera could be utilized. The high thermal conductivity and low thermal capacitance simplified the experimental design by reducing the cooling power necessary and helped to insure an acceptably isothermal test surface. Small samples were manufactured from aluminum sheet (10 mm x 31 mm x 0.8 mm). This size was selected so that it would easily fit in**

the headspace vials utilized with the HS-C-GC-FID technique to determine the total amount of water present.

The experimental configuration utilized in the calibration experiments is shown schematically in Figure 6.6 and photographically in Figure 6.7. A detailed list of the equipment and settings utilized is presented in Appendix B.

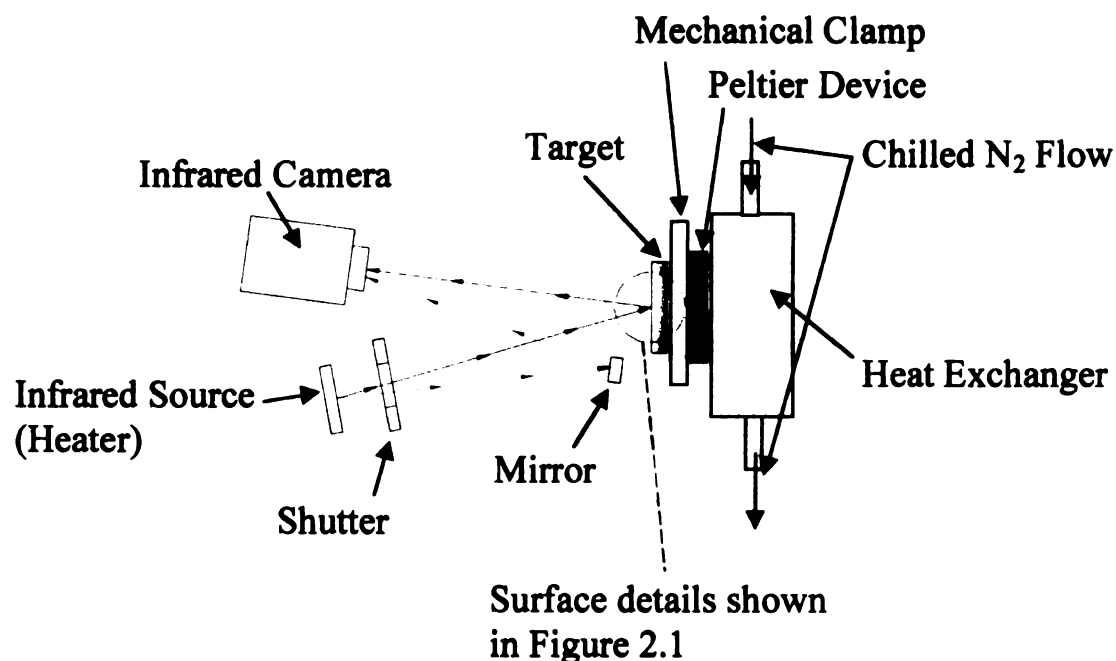


**Figure 6.6.** Schematic of the IR-H<sub>2</sub>O calibration experiment.



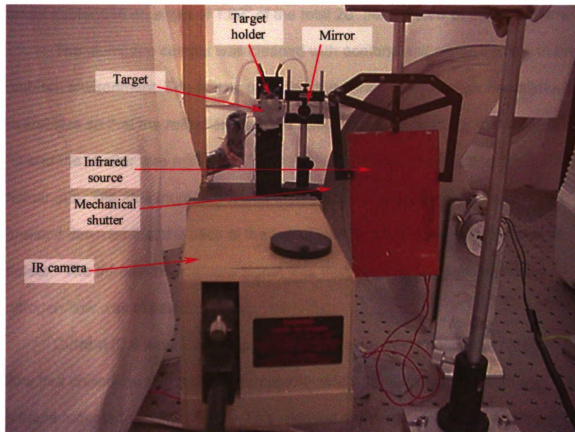


**Figure 6.7.** Photograph of the IR-H<sub>2</sub>O calibration experiment.

The initial calibration experiment was performed with the IR camera at a distance from the calibration samples that could be replicated in the FMTF facility. The test was designed in this fashion so that if further testing indicated distance was an important factor, extensive recalibration would not be necessary prior to use in the FMTF. The Inframetrics camera was positioned with the bayonet mount 616 mm (24.25") from the calibration target and viewed the target at an angle of 8° from perpendicular. The viewing angle was necessary to

illuminate the sample with the infrared source (heater). The aluminum calibration target subtended an angle of  $1.02^\circ$  of the total  $20^\circ$  field of view of the IR camera.

The aluminum sample was cleaned with acetone and allowed to dry in the ambient environment. The heater providing the infrared illumination was allowed to stabilize so that the reflection from the reference mirror was approximately  $49^\circ\text{C}$  and the shutter was activated. The sample holder was heated and dried with a hot air gun. The aluminum target was then placed in the mechanical clamp and pressed down so that the back of the target was in firm contact with the sample holder. The Inframetrics camera signal was then recorded and the chilled nitrogen flow was initiated.

Current (0.6 amps) was supplied to the Peltier device once the nitrogen flow had chilled the target holder to approximately  $15^\circ\text{C}$  (monitored with a surface mounted thermocouple). This reduced the target temperature below the ambient dew-point within 180 seconds. The current to the Peltier device was adjusted if necessary to maintain the target above the freezing point. The temperature of the target was inferred from a thermocouple mounted next to the target on the aluminum clamp holding the target. The clamp and target were of identical thickness and were in good thermal contact with one another.

The target was then allowed to soak in the ambient environment for various lengths of time to allow condensate to build up on the front surface of the target. The target was then dropped into a 22 mL headspace vial, calcium carbide was added and the vial was sealed for later analysis with the HS-C-GC-FID technique outlined in section 6.1.1. The total mass of water present was

divided by the surface area of the sample exposed to the atmosphere to obtain an estimate of the average condensate thickness. The condensate was assumed to be uniformly dispersed on the exposed aluminum surface based on the uniformity of the changes in the surface reflectance. The coefficient of variation of the surface reflectance was typically 3.8% and always less than 5%. The average thickness was utilized since the IR camera measurement integrates over each measurement pixel. The initial and final reflectance measurements of the targets were obtained from the recorded video data. The results of this process are presented in Figure 6.8.

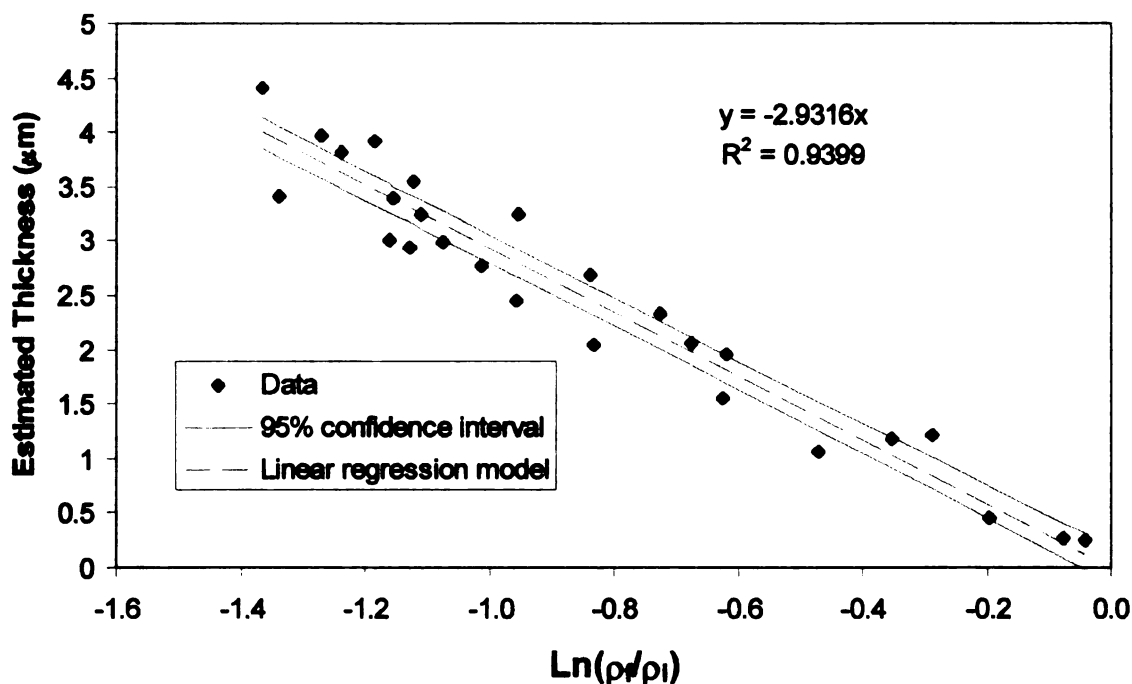


**Figure 6.8.** Ensemble correlation of reflectance ratio to estimated thickness of condensate present.

The data are represented by the solid diamonds in Figure 6.8. A linear regression model was fitted to the data. The model was forced to have a zero intercept since the physics of the problem indicates that a dry sample should not change reflectance without modification of the surface. This causes a very slight change in the model. If an intercept is incorporated into the model, the fitted line is  $y = -2.893x + 0.0329$ . However, the null hypotheses of zero intercept is retained (t-test p-value = 0.81) so the fitted line given in Figure 6.8 was used for the calibration. The 95% confidence interval of the mean regression result presented in Figure 6.8 is less than  $\pm 0.17\mu\text{m}$ . The scatter in the data about the regression model is larger and could be interpreted as a truer estimate of the variability of the technique since the calibration targets only approximate the test surface. The standard deviation of the data about the log-linear regression line is  $\sigma = 0.30\mu\text{m}$ . The usefulness of this result is dependant on the calibration surfaces being representative of the test surface. The type of surface material and finish are critical to maintaining this assumption.

The variability of the data in Figure 6.8 was investigated. It was discovered that the residuals were dependent on the target utilized. Plotting the data for each target shows a higher degree of linearity in the results for each target. Figure 6.9 presents the data from Figure 6.8 for each target and demonstrates the effect of the target on the result obtained.

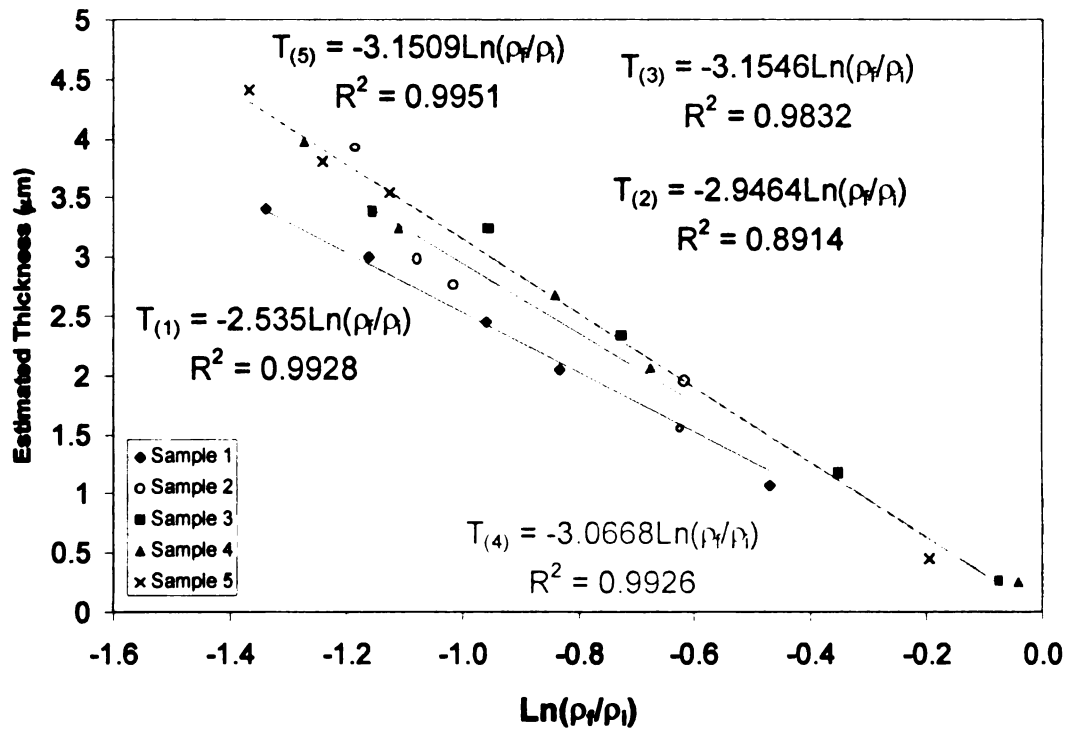


**Figure 6.9. Correlation of reflectance ratio to estimated thickness of condensate present for each aluminum target utilized.**

The aluminum targets were handled in an identical fashion for each calibration experiments. Targets #1, #4, and #5 were polished with an abrasive pad to create a homogeneously roughened surface. The surfaces of targets #2 and #3 were left with the original cold rolled finish. The differences between samples could be the result of minute surface variations. The high degree of linearity for each test result (with the possible exception of target #2) indicates that the simple reflectance model does provide an appropriate non-dimensional form for the data. This result indicates that the best condensate thickness

measurement can be obtained by utilizing a calibrated target in the flow field of interest. A composite calibration of representative surfaces can be utilized but the uncertainty in the measurements would increase. This can be observed directly by comparing the squared correlation coefficients ( $R^2$ ) in Figures 6.8 and 6.9 as well as the obviously improved linearity of the results when separated by individual target specimens.

#### ***6.1.3 EFFECT OF DISTANCE AND ANGLE ON THE IR-H<sub>2</sub>O OPTICAL CALIBRATION.***

The distance between the IR camera and the surface of interest is not expected to effect the correlation results. The slit response function (SRF) of the Inframetrics 600L infrared camera utilized in these experiments was empirically determined previously [Hoke, 1998]. At the distance utilized for all the experiments presented here, the pixel size is 6.1 mm and the 95% SRF is 7.0 mm. The camera is incapable of resolving objects of the scale of the individual droplets on the aluminum targets. The infrared detector effectively integrates a local reflectance in each pixel, thus averaging the effect of multiple droplets.

The angle of incidence between the infrared camera, the surface and the infrared source is not anticipated to significantly effect the results over angles less than the Brewster angle of the condensate. The optical path length through the droplets/film is a weak function of angle at small angles and thus small variation in the viewing and illumination angle should not effect the calibration significantly. However, empirical calibration of angles much greater than were utilized here ( $8^\circ$ ) is recommended prior to application.

## **6.2. VALIDATION OF THE OPTICAL MEASUREMENT CALIBRATION WITH A NON-HOMOGENEOUS CONDENSATE FIELD**

**A method to validate the optical measurement was sought as a means to confirm the accuracy of the experimental correlation developed. Two concepts were explored before a methodology was decided upon. The first method was to create a "sandwich" of liquid water between two materials with a gap width of known thickness. The second method explored was to create a non-homogeneous condensate field on the aluminum targets. The volume measurement obtained from the HS-C-GC-FID method could then be compared with a pixel by pixel, surface integral of the condensate volume obtained from the infrared, surface reflectance measurements.**

**The sandwich method required surfaces with an acceptable flatness and smoothness tolerance. The surfaces would have to be smooth to within 0.25  $\mu\text{m}$  and would have to maintain a flatness specification across the target surface of similar dimensions in order to provide a useful measurement. Variation in the surface larger than 0.25  $\mu\text{m}$  would create larger uncertainty than that obtained with the HS-C-GC-FID calibration and would limit the usefulness of the validation technique. One material would also have to be transparent to infrared radiation and the other material would have to be highly reflective to the same wavelengths. Aluminum and germanium were selected as possible materials based on these criteria. Four significant problems arose as this method was further investigated. These complications were:**

1. Aluminum target surface would not match current target surface characteristics. The current calibrated aluminum targets would not be useable for this technique.
2. A germanium lens with appropriate specifications would cost approximately \$2000 for a 25mm diameter specimen.
3. Condensate in the gap would not be consistent with the structured condensate observed in the calibration or FMTF experiments and could therefore create different results. This could limit the usefulness of any comparisons made.
4. Selecting an appropriate gap material to space the aluminum and germanium materials.

Due to these difficulties, the non-homogeneous method was then explored. This method requires that a non-uniform condensate film develop on the aluminum targets. Altering the aluminum target surface temperature, altering the concentration gradient over the target surface, or altering the mass transfer coefficient could create the desired non-uniform condensate field. The total condensate volume on the target could then be measured with the HS-C-GC-FID technique. The change in the surface reflectance of the aluminum target would then be evaluated pixel by pixel and a thickness calculated for each pixel with the correlations presented in Figures 6.8 and 6.9. Since the pixel size is known, a total volume of condensate on the surface can be calculated. The resulting volume from the infrared technique can then be compared directly to the HS-C-GC-FID result.



The non-uniform method provided a much more direct and simple means of validation and allowed direct comparison to the existing data set with the fewest number of possible complications and was therefore selected. The weakness of the non-uniform method was that it also utilizes the gas chromatographic technique so an error hidden in this technique would also effect the non-uniform tests. However, since the condensate film would not be uniform but would qualitatively have the same structure, it was decided that this method was superior to creating an artificially uniform liquid film with the known gap "sandwich" technique.

Initially, a non-uniform, fin like temperature distribution was chosen for creating the non-homogeneous condensate field. A model was created to estimate the temperature distribution that might be obtained with varying sample thicknesses. An estimate of  $5 \text{ W m}^{-2} \text{ K}^{-1}$  for the convective heat transfer coefficient was made assuming a zero velocity far field with a temperature of  $20^\circ\text{C}$ . The model was based on a one-dimensional fin analysis since only the lower portion of the target would be cooled and the back of the aluminum target would be placed against an insulating Teflon surface to insure that condensate only developed on the side of the target facing the infrared camera. The model predication for the temperature distribution are presented in Figure 6.11. The axes in Figure 6.11 represent the location on the target surface ( $x \text{ (m)}$ ), the target material thickness ( $m$ ), and the vertical axis is the target temperature ( $K$ ).

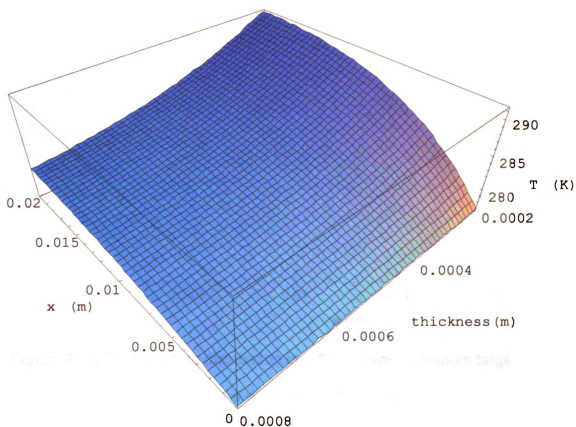


**Figure 6.11.** Temperature distribution in aluminum target derived from a one-dimensional fin analysis.

Since the influence of the specific targets was previously identified as discussed in section 6.1.2, the target thickness was fixed at 0.8 mm so that the calibrated targets could continue to be utilized. This resulted in a temperature profile on the aluminum target as shown in Figure 6.12.

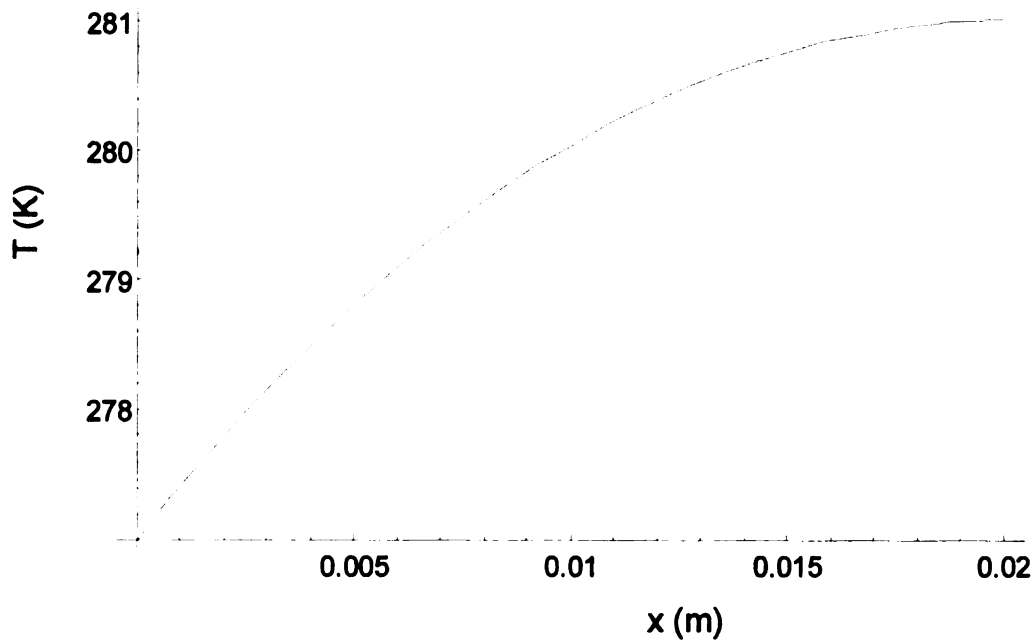


**Figure 6.12.** Temperature distribution in 0.8 mm thick, aluminum target derived from a one-dimensional fin analysis.

The temperature distribution presented in Figure 6.12 results in a spatial variation in the concentration gradient driving the mass transfer to the target surface. Equation (6.6) was utilized to convert the temperature gradient to a concentration gradient along the target [Çengel and Boles, 1989].

$$\Delta C = C_j - \frac{0.622 \phi P_{ref} e^{\frac{L}{R_w} (\frac{1}{T_{ref}} - \frac{1}{T(x)})}}{R_{air} T(x)} \quad (6.6)$$

Utilizing (6.6) results in a spatial distribution of the concentration difference along the length of the 0.8 mm thick, aluminum target as shown in Figure 6.13.

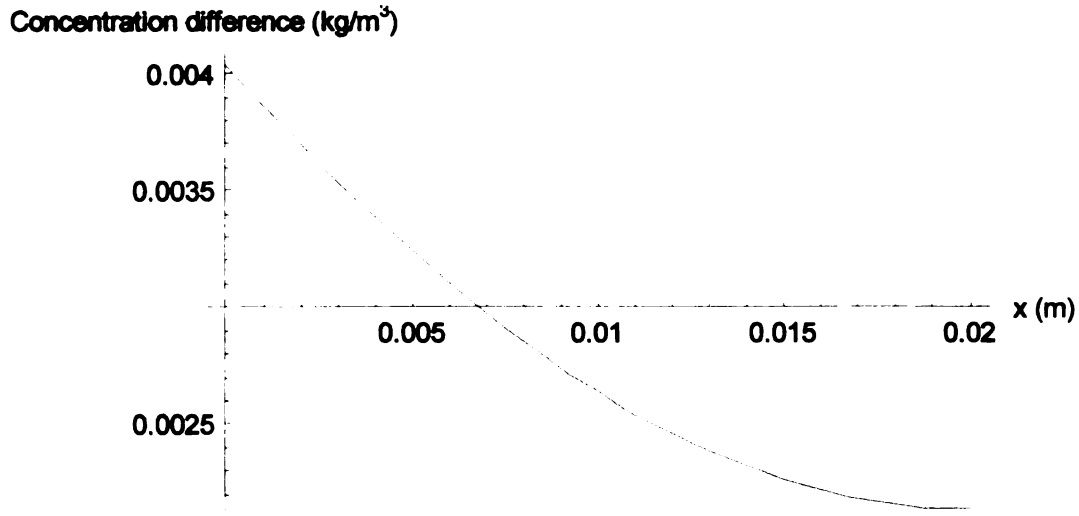


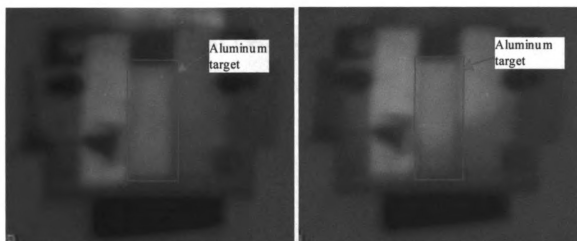
**Figure 6.13.** Concentration gradient distribution along the aluminum target resulting from the fin temperature distribution.

This temperature gradient results in an approximate 40% variation of the concentration gradient along the surface. Initial experimental data did not agree with the model results. Only a 5-15% variation in the target surface temperature was observed. This was attributed to the fact that a quiescent far field did not exist and that the Teflon insulation cooled much quicker than the model indicated. A more pronounced difference in the condensate pattern was desired so a means was sought to amplify the variation.

Dry nitrogen gas is currently used to cool the heat exchanger attached to the Peltier device (see Figure 6.6). The nitrogen flow exits the heat exchanger system with an approximate temperature of 10 °C. Experiments revealed that diverting this flow to the surface for an instant could dry a portion of the aluminum target and since the temperature was above the freezing point, there was no risk of causing icing of the surface. This method was adopted to enhance the variation in the condensation field.

#### ***6.2.1. NON-HOMOGENEOUS EXPERIMENTAL PROCEDURE AND RESULTS.***

The calibration procedure outline in section 6.1.2 was utilized with one additional step, dry nitrogen gas was utilized to evaporate a region of condensation on the target prior to capture in the 22 mL headspace vials. This produced a non-homogeneous condensate field. Examples of two typical thermograms before and after a region was exposed to the nitrogen flow are presented in Figure 6.14.



*Before application of  $N_2$  jet*                      *After application of  $N_2$  jet*

**Figure 6.14.** Non-homogeneous concentration field on an aluminum target before and after a portion was dried with nitrogen gas.

The infrared image was then evaluated pixel by pixel with the correlation previously obtained for the uniform condensation, IR- $H_2O$  calibration result (Figure 6.9). The calculated thickness was multiplied by the area per pixel to obtain a volume of condensate present. The thickness variation on a target in a typical experiment is presented in Figure 6.15. The coefficient of variation (COV) of the image data in Figure 6.15 is 27.8%. The average COV observed during the non-uniform tests was 27.1% and ranged from 3.7% to 47.7%.

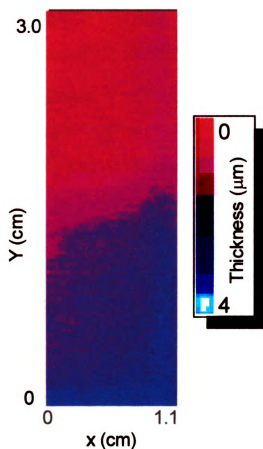


**Figure 6.15.** Measured thickness results on aluminum target #4 during a non-homogeneous condensation field test.

The volume obtained with the pixel by pixel analysis was compared to the result obtained from the HS-C-GC-FID technique. A perfect result would present a 1:1 slope when the IR and the HS-C-GC-FID results were plotted against one another. The results of the comparison are presented in Figure 6.16.

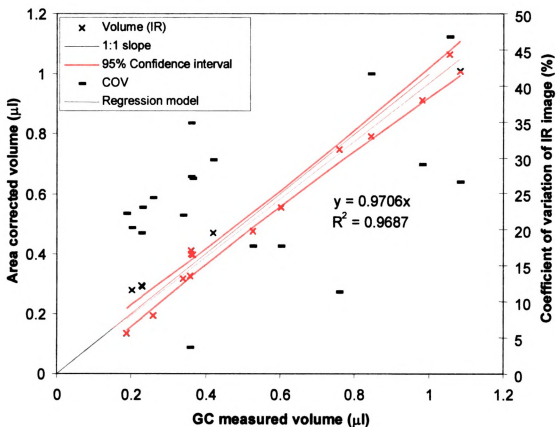


**Figure 6.16.** Results of the non-homogeneous concentration field tests utilizing the HS-C-GC-FID technique as the reference standard.  
Coefficient of variation in each non-uniform image presented.

Data from 18 tests are presented in Figure 6.16. The result in Figure 6.16 agrees with the expected slope of 1.0 within the statistical uncertainty of the data. This indicates that the method is self-consistent and capable of resolving the total mass transfer to a surface with a non-homogeneous condensate field.



The correlations derived for each aluminum target were utilized to convert the change in surface reflectance to a local thickness (Figure 6.9). The surface area contained in each pixel was then determined from the optical arrangement. Multiplying the pixel area by the calculated condensate thickness and summing across the surface results in a total volume estimate derived from the infrared reflectance measurement. The entire aluminum target was not analyzed because the edge effects where the target is held create non-physical artifacts in the infrared image. Approximately 88% of the surface was interrogated optically and the assumption was made that the remainder of the surface contained an identical condensation pattern. Thus each optically integrated IR result was multiplied by a factor of 1.136 to correct for the area. This assumption could account for some of the scatter observed in Figure 6.16.

## **Chapter 7**

### **OPTICAL, TRANSIENT MASS TRANSFER MEASUREMENTS IN THE DEVELOPING WALL JET**

#### **7.1 INTRODUCTION**

The final phase of the project was to measure the mass transfer to the thermally active test surface in the Ford-MSU test facility with the new optical infrared reflectance technique. This represents the culmination of the project to collect a benchmark data set for the purpose of calibrating the CFD model. These measurements provide condensate thickness data as a function of time and location. Surface temperature measurements combined with temperature and humidity measurements in the wall jet provide the necessary data to determine the concentration difference in the flow field. This combination of data allows the mass transfer coefficient and the Sherwood number to be calculated as a function of time and location. The results of the transient data measured with the optical technique will be compared to the steady state results presented in Chapter 5 and with steady state results in the published literature. These results indicate that the optical infrared reflectance technique is functioning as expected and provide insight into application of the technique.

#### **7.2 EXPERIMENTAL CONFIGURATION**

The infrared camera was positioned to view the thermally active test section from a distance of 616 mm at an angle of  $8^\circ$ . This distance and angle are identical to those utilized in the calibration experiments presented in Chapter 6.

A hole was cut in the Lexan® window in the FMTF in order to provide optical access for the infrared camera. A 3" x 12" heater thermally bonded to a blackened aluminum plate was utilized as a source of infrared illumination. Electrical current sufficient to heat the aluminum plate to approximately 49 °C was supplied. Figure 7.1 presents a photograph of the experimental configuration in the FMTF. Note that the infrared source (heater) and shutter are hidden on the far side of the camera.

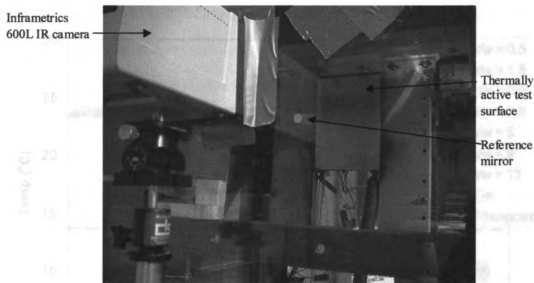


**Figure 7.1.** Experimental setup in the Ford-MSU test facility.

The constant temperature bath was set to the desired temperature (typically, 4 °C) and allowed to stabilize with the flow to the thermally active test section turned off. The thermocouple and video data acquisition systems were

activated and the initial reflectance of the surface was measured. The flow to the thermally active test section was initiated and the mechanical shutter was activated to capture reflectance measurements of the thermally active test section as the surface temperature decreased below the wall jet dew-point temperature. Figure 7.2 contains the thermocouple temperature record of the thermally active test section.

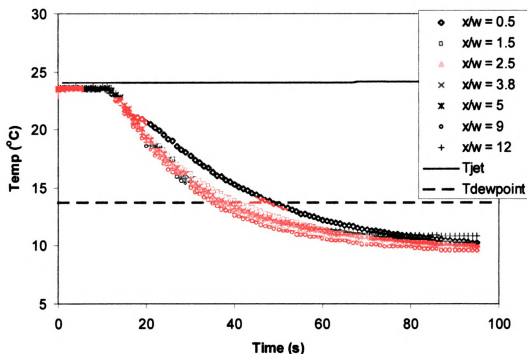


**Figure 7.2.** Surface temperature history of the thermally active test section during a typical transient condensation experiment.

The thermocouples are mounted on the back of the thermally active test section at the streamwise locations indicated in Figure 7.2. The thermocouples are mounted off the centerline of the test section at  $z/w = -1.0$ . This location corresponds to the measurement location interrogated by the optical infrared reflectance technique on the opposite surface.

### 7.3 TRANSIENT OPTICAL DATA

Infrared images of the surface were recorded with a video cassette recorder for the duration of the experiment for post processing. The images were time marked during recording with a video timer. The raw video images were captured as digital images with Image Pro Plus 4.1 (Media Cybernetics) and intensity data were extracted from the images for further analysis. Two images are utilized to calculate the apparent surface reflectance utilizing the same techniques detailed in Chapter 6. An example of the raw 8 bit images and the resulting surface reflectance obtained from the image data is presented in Figure 7.3.

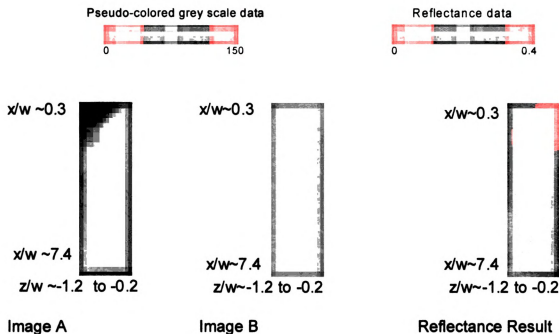


**Figure 7.3.** Typical infrared images of the thermally active test surface during transient condensation experiment and the resulting surface reflectance.

The two-dimensionality of the results presented in Figure 7.3 is expected to be due to the temperature variations on the thermally active test surface. This pattern is not evident in the measurement of the initial surface reflectance and changes throughout the experiment. The standard deviation of the condensate thickness measurement across the image never exceeds  $0.25 \mu\text{m}$  at any instant and the maximum difference between the maximum and the minimum is typically less than  $0.6 \mu\text{m}$ . The initial surface reflectance and the surface reflectance at  $t = 69\text{s}$  are presented in Figure 7.4 for comparison.

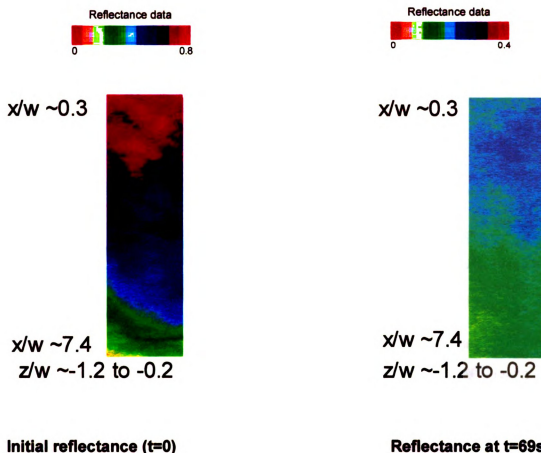


**Figure 7.4.** Reflectance measurements at  $t = 0s$  and  $t = 69s$  of thermally active test surface.

The surface reflectance measurements of the thermally active test section were converted to condensate thickness measurements with the result presented in Figure 6.8. The conversion to thickness of the image data was conducted pixel by pixel. The mapping from optical surface reflectance to condensate thickness provided spatial and temporal data of the mass transfer to the thermally active test section. Sample measurements of the condensate thickness development

on the test surface are presented in Figure 7.5. Further experimental measurement results of the transient condensate development are included in Appendix E.

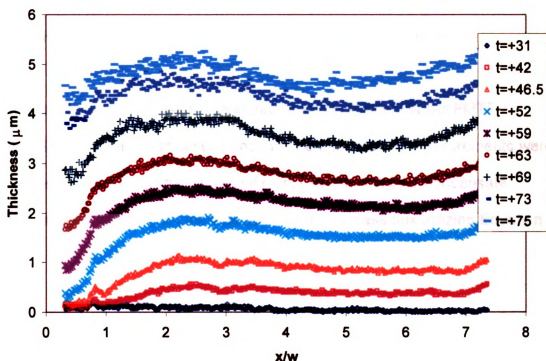


**Figure 7.5.** Typical condensate thickness measurements on the thermally active test surface during transient condensation ( $T_j = 24.1\text{ }^{\circ}\text{C}$ ,  $\%Rh_j = 51.1$ ).

The data collected can be utilized to calculate the concentration difference in the flow field and mass flux to the surface, thus providing a measure of the mass transfer coefficient as a function of location and time. The transformation of



the image data to the transient condensate thickness measurements and discussion thereof will be presented in the next section. Temporal variation of the mass transfer coefficient is not anticipated in the results since the velocity field is steady with only the surface temperature changing. The rate of change in the surface temperature is less than 0.5 °C/s while the flow is resident on the thermally active test surface for less than 0.05 seconds. The concentration difference does develop transiently with the surface temperature.

#### 7.4 RESULTS OF THE TRANSIENT CONDENSATION EXPERIMENTS IN THE FMTF

The condensate thickness and surface temperature measurements were converted to local mass transfer coefficient data. Initially the condensate thickness as a function of time was converted to a mass flux utilizing Equation (7.1):

$$j'' = \left( \frac{T(t_2) - T(t_1)}{t_2 - t_1} \right) \rho_{H_2O} \quad (7.1)$$

The concentration difference between the thermally active test surface and the wall jet flow was calculated using the Clausius-Clapeyron equation [Çengel and Boles, 1989]. The temperature and humidity of the wall jet and temperature of the chilled surface were used for the calculation. The assumption of thermodynamic equilibrium is employed at the thermally active test surface. The result is:

$$\Delta C = (\omega \rho)_j - (\omega \rho)_s =$$

$$= 0.622 P_{\text{Ref}} \left( \frac{\rho_j \% R h_j e^{\left( \frac{h_{fg}}{R} \left( \frac{1}{T_{\text{Ref}}} - \frac{1}{T_j} \right) \right)}}{P_{\text{Tot}} - P_{\text{Ref}} e^{\left( \frac{h_{fg}}{R} \left( \frac{1}{T_{\text{Ref}}} - \frac{1}{T_j} \right) \right)}} - \frac{\rho_s e^{\left( \frac{h_{fg}}{R} \left( \frac{1}{T_{\text{Ref}}} - \frac{1}{T_s} \right) \right)}}{P_{\text{Tot}} - P_{\text{Ref}} e^{\left( \frac{h_{fg}}{R} \left( \frac{1}{T_{\text{Ref}}} - \frac{1}{T_s} \right) \right)}} \right) \quad (7.2)$$

The complete derivation of Equation (7.2) is presented in Appendix D.

Note that the temperature of the thermally active test surface ( $T_s$ ) is a function of time and location. The temperature profile on the test surface was interpolated from the thermocouple results presented in Figure 7.2. An example of the resulting temperature profile on the test surface is presented in Figure 7.6. Note that the discrete data points in the figure indicate the surface temperature measurements and thus the actual thermocouple locations.

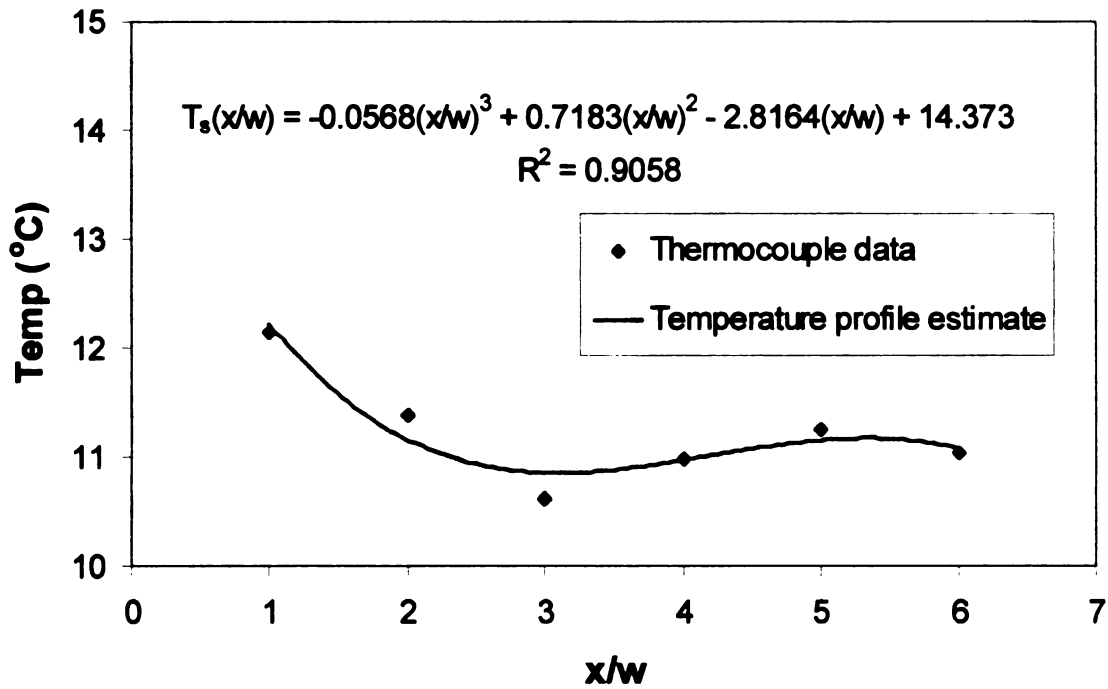


**Figure 7.6.** Typical temperature profile at  $t = 59s$  on the thermally active test surface during transient condensation experiment ( $T_j = 24.1\text{ }^{\circ}\text{C}$ ,  $\%Rh_j = 51.1$ ).

The temperature profile in Figure 7.6 was then used with Equation (7.2) to estimate the concentration difference along the thermally active test surface. The estimated concentration difference at  $t = 59s$  for experiment #2 on 15 June, 2001 is presented in Figure 7.7.

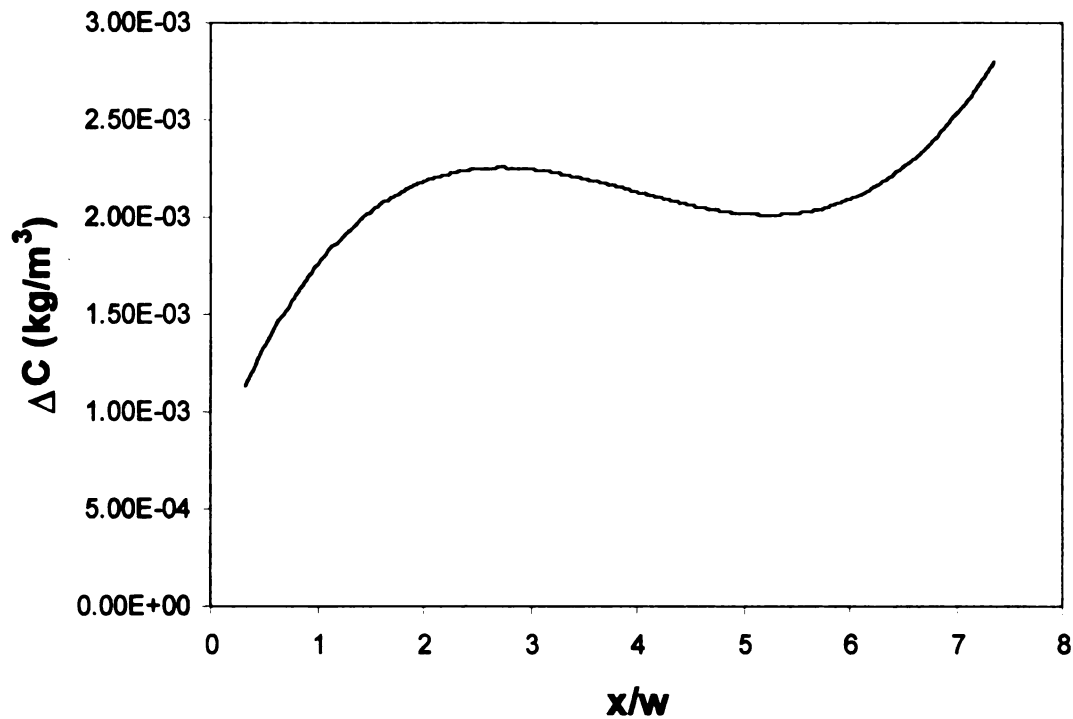


**Figure 7.7.** Typical concentration difference between the wall jet flow and the thermally active test surface at  $t = 59\text{s}$  during transient condensation experiment.

The concentration difference and the mass flux can be used with Fick's law, Equation (7.3), to calculate the mass transfer coefficient. Note that the average concentration difference between the measurement times  $t_2$  and  $t_1$  was utilized in the mass transfer coefficient and the Sherwood number calculations.

$$h_m = \frac{j''}{\Delta C} \quad (7.3)$$

The Sherwood number can be applied to non-dimensionalize the data obtained with the optical infrared reflectance technique. The Sherwood number based on the jet orifice width, with Equations (7.1), (7.2), and (7.3), is equal to

$$Sh_w = \frac{h_m w}{D} = \frac{\left( \frac{T(t_2) - T(t_1)}{t_2 - t_1} \right) \rho_{H_2O} w}{0.622 P_{Ref} \left( \frac{\rho_j \% R h_j e^{\left( \frac{h_{fg}}{R} \left( \frac{1}{T_{Ref}} - \frac{1}{T_j} \right) \right)}}{P_{Tot} - P_{Ref} e^{\left( \frac{h_{fg}}{R} \left( \frac{1}{T_{Ref}} - \frac{1}{T_j} \right) \right)}} - \frac{\rho_s e^{\left( \frac{h_{fg}}{R} \left( \frac{1}{T_{Ref}} - \frac{1}{T_s} \right) \right)}}{P_{Tot} - P_{Ref} e^{\left( \frac{h_{fg}}{R} \left( \frac{1}{T_{Ref}} - \frac{1}{T_s} \right) \right)}} \right) D} \quad (7.4)$$

The results of a typical experiment transformed into non-dimensional (Sherwood number) form are presented in Figure 7.8. The legend indicates the approximate center time of the data utilized to calculate the Sherwood number and indicates the total time separation ( $dt = t_2 - t_1$ ) in seconds between the condensate thickness measurements used to calculate the mass flux and the concentration difference.

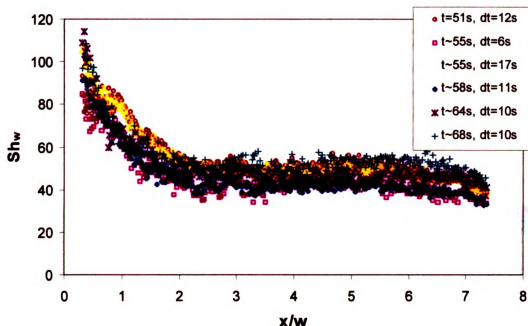


**Figure 7.8.** Typical Sherwood number results on the thermally active test surface during transient condensation experiment ( $T_j = 24.1\text{ }^{\circ}\text{C}$ ,  $\%Rh_j = 51.1$ ).

Note that the scatter near the onset of condensation ( $t_{\text{dew-point}} \sim 40\text{ s}$ ) is the result of the increased uncertainty in the concentration difference. The uncertainty will be discussed in detail in section 7.6.

The entire length of the thermally active test section was surveyed in two separate experiments since the field of view of the infrared camera was not sufficient to visualize the entire test surface at the working distance utilized. The first section of the thermally active test surveyed extended from  $x/w \sim 0.3$  to  $7.4$ . The second field of view produced data from  $x/w \sim 5.1$  to  $12.1$ . The compiled results are presented in Figure 7.9.

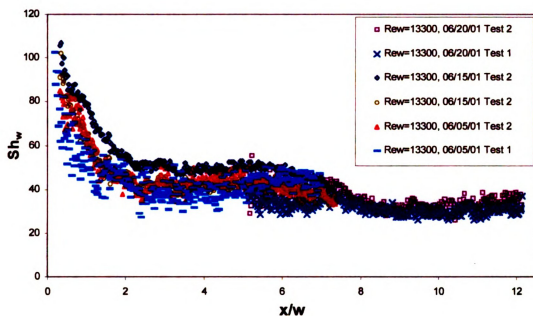


**Figure 7.9.** Compiled Sherwood number results on the thermally active test surface ( $Re_w=13300$ ).

The Sherwood number results presented in Figure 7.9 are internally consistent and of the correct order of magnitude to be consistent with expectations. Figure 7.10 presents a comparison of the data in Figure 7.10 (collapsed to a single curve fit) to the steady state results published by Mabuchi and Kumada [1972]. A fifth order curve was fit to the experimental data. The experimental Sherwood number is not expected to be a polynomial but a function of  $Re_x^{0.5}$  and/or a  $Re_x^{0.8}$ . These relationships are the classical results for laminar or turbulent flow fields respectively. However, since the exact form of the data is unknown, a fifth order fit was deemed acceptable. Note that in Figure

7.10, the tripped results from Mabuchi and Kumada, which conform to a  $Re_x^{0.8}$ , show the same profile as the present results.

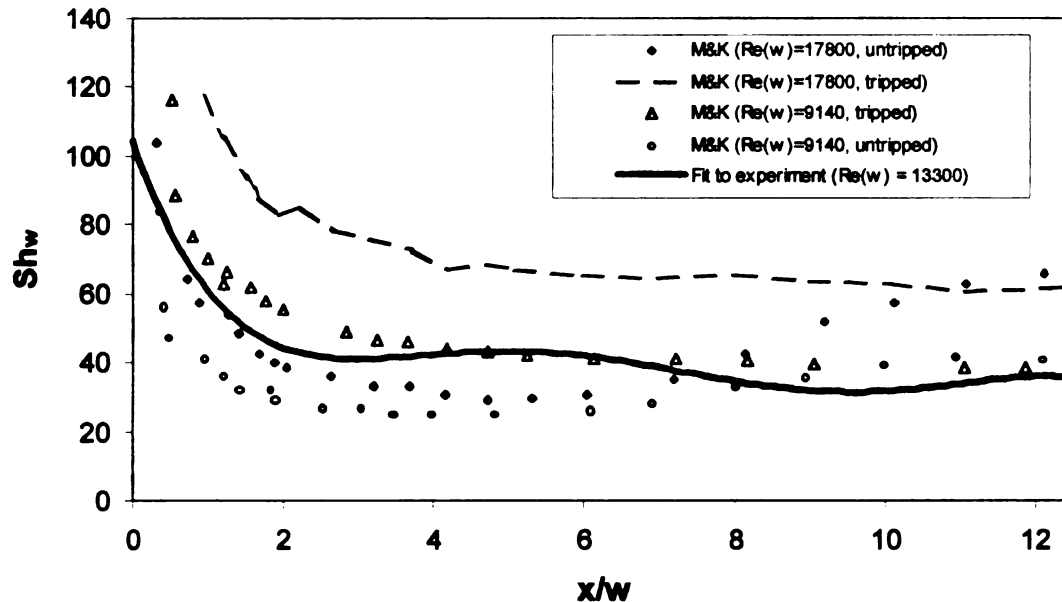


**Figure 7.10.** Comparison of experimental and published [Mabuchi and Kumada, 1972] Sherwood number results.

The experimental result in Figure 7.10 does not indicate the laminar to turbulent transition that is evident in the  $Re_j = 17,800$  result from Mabuchi and Kumada [1972]. The transition is region is visible in the Sherwood number increasing after reaching a local minimum (at approximately  $x/w = 5$ ). This is not necessarily unexpected since the developing region of the jet is influenced strongly by the particular jet orifice and upstream conditions ( $x/w < 25$ ) [Mabuchi and Kumanda, 1972]. The turbulence intensity at the jet exit can also strongly



influence the location and nature of the transition region. The results published by Federov et. al. [1997] indicate that the average Sherwood number increases by 19% as the turbulence intensity increases from 0% to 1%. The study by Federov et. al. was conducted in a developing channel flow but the results indicate that the transition location is responsible for the dramatic change in the Nusselt and Sherwood numbers. Small changes in the turbulence intensity were observed to create large changes in the heat transfer in the laminar range by Kestin et. al. [1961] in a flat plate boundary layer. Kestin et. al. attribute this effect solely to the change in the transition location in the flow field. Analogous effects could be expected in the developing wall jet flow. The turbulence intensity upstream of the jet orifice in the Ford-MSU test facility is 1.7%. The profile of the measured fluctuations at the wall jet orifice is detailed in Figure 3.2. Mabuchi and Kumada [1972] do not specify the turbulence intensity at any location in their test flow.

The data obtained with the optical infrared reflectance technique were then integrated spatially for direct comparison to the steady state results presented in Chapter 5. The fifth order curve fit of the experimental Sherwood number results was integrated to estimate the spatially averaged result on the entire thermally active surface. The fit to the experimental data is presented for clarity in Figure 7.11.

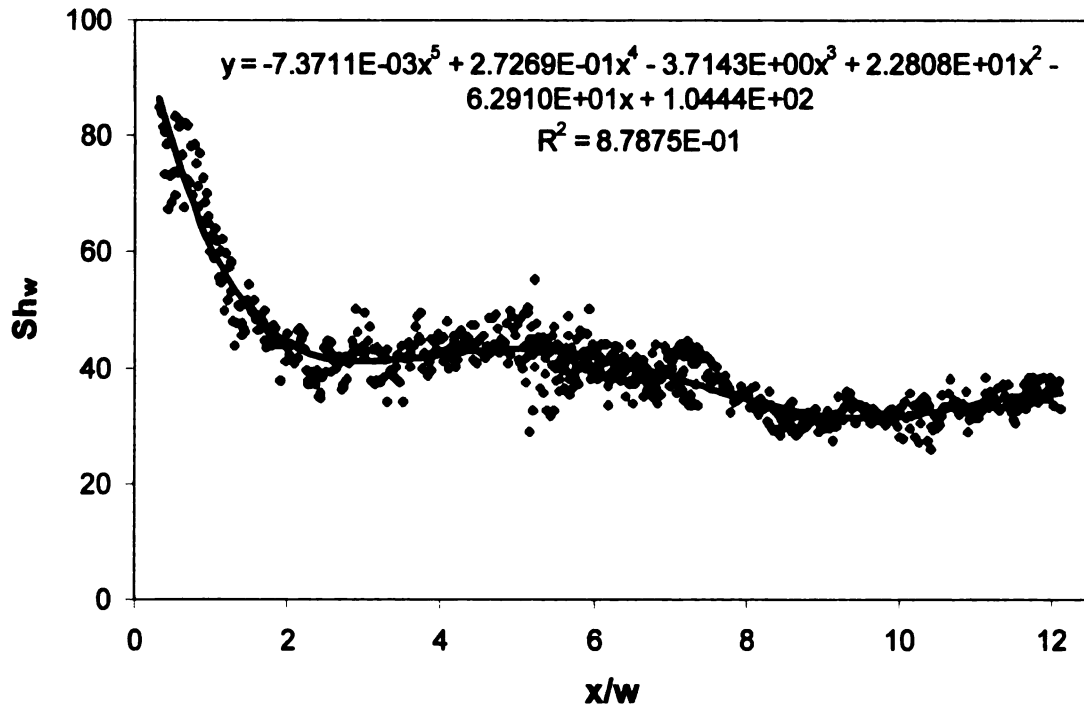


**Figure 7.11.** Experimental Sherwood number results fitted with a fifth order curve.

The fit to the data was integrated with Equation (7.5) to determine the spatially averaged Sherwood number.

$$Sh_w = \frac{1}{L} \int_0^L f(x) dx \quad (7.5)$$

This results in a spatially averaged Sherwood number of 42.1. This result and the experimental steady state result ( $Sh_w = 38.2 \pm 3.4$ ) agree to within the

overlapping 95% uncertainty regions. This result is significant because it indicates internal consistency for the experimental results obtained in the FMTF flow field. Since the transient results and the steady state results are expected to agree since the velocity fields in the two experiments are identical.

## **7.5 SHERWOOD NUMBER DEPENDENCE ON JET REYNOLDS NUMBER**

Experiments were conducted by varying the wall jet velocity to further investigate the optical infrared reflectance technique. The Sherwood number results were expected to increase with increasing Reynolds number, similar to the trends apparent in Mabuchi and Kumada [1972]. Figure 7.12 presents the experimental results as a function of the jet Reynolds number.

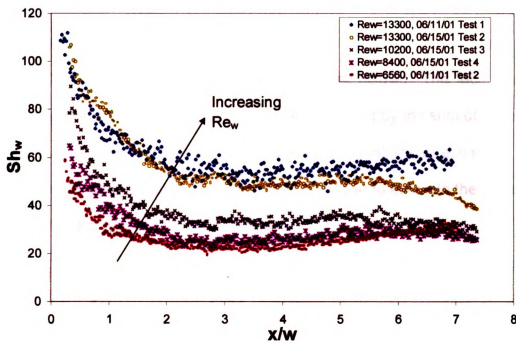


**Figure 7.12.** Experimental Sherwood number results as a function of the jet Reynolds number.

The trends measured with the optical infrared reflectance technique show the expected increase in the Sherwood number with increasing Reynolds number. None of the Reynolds number results show clear evidence of a laminar to turbulent transition region. The profile measured in the FMTF is consistent between experiments however, and may be the distinctive signature of the wall jet geometry, turbulence intensity, and the upstream flow conditioning in the Ford-MSU test facility.

## 7.6 UNCERTAINTY ESTIMATES FOR THE OPTICAL INFRARED REFLECTANCE TECHNIQUE

An uncertainty estimate was calculated based on the observed uncertainties in the optical infrared reflectance technique. The technique of partial derivatives as outlined by Moffat [1988] was utilized. This technique results in the uncertainty in a function being estimated by the sum of squares of the partial derivatives multiplied by the measured variability (or estimated variability) in each variable. Equation (7.6) is utilized to estimate the uncertainty in R which is a function of the variables  $X_i$  :

$$\delta R = \left\{ \sum_{i=1}^n \left( \frac{\partial R}{\partial X_i} \delta X_i \right)^2 \right\}^{0.5} \quad (7.6)$$

Applying Equation (7.6) to the Sherwood number result presented in Equation (7.4) provides an estimate of the uncertainty in the Sherwood number. The result of this calculation is lengthy and is included in Appendix F. The variables and the uncertainty associated with each is presented in Table 7.1.

**Table 7.1. Variables and uncertainties utilized to calculate the uncertainty in the Sherwood number.**

<b>Variable (<math>X_i</math>)</b>	<b>Uncertainty (95% confidence level typically) (<math>\delta X_i</math>)</b>
T(t) (thickness)	$\pm 0.17 \text{ } \mu\text{m}$ (from regression model in Figure 6.8)
t (time)	$\pm 0.5 \text{ s}$
w (jet width)	$\pm 0.0005 \text{ m}$
D (diffusivity)	$\pm 2 \times 10^{-7} \text{ m}^2/\text{s}$
$T_s$ (wall temperature)	$\pm 0.25 \text{ } ^\circ\text{C}$
$T_j$ (jet temperature)	$\pm 0.25 \text{ } ^\circ\text{C}$

Applying Equation (7.6) to the Sherwood number ( Equation (7.4)), with the values specified in Table 7.1, results in the uncertainty estimate in the Sherwood number presented in Figure 7.13. This result is not exact for each experiment conducted since the specific uncertainty estimates will depend on the experimental conditions realized. Note that the uncertainty is the greatest when the test surface temperature is near the calculated dew-point temperature.

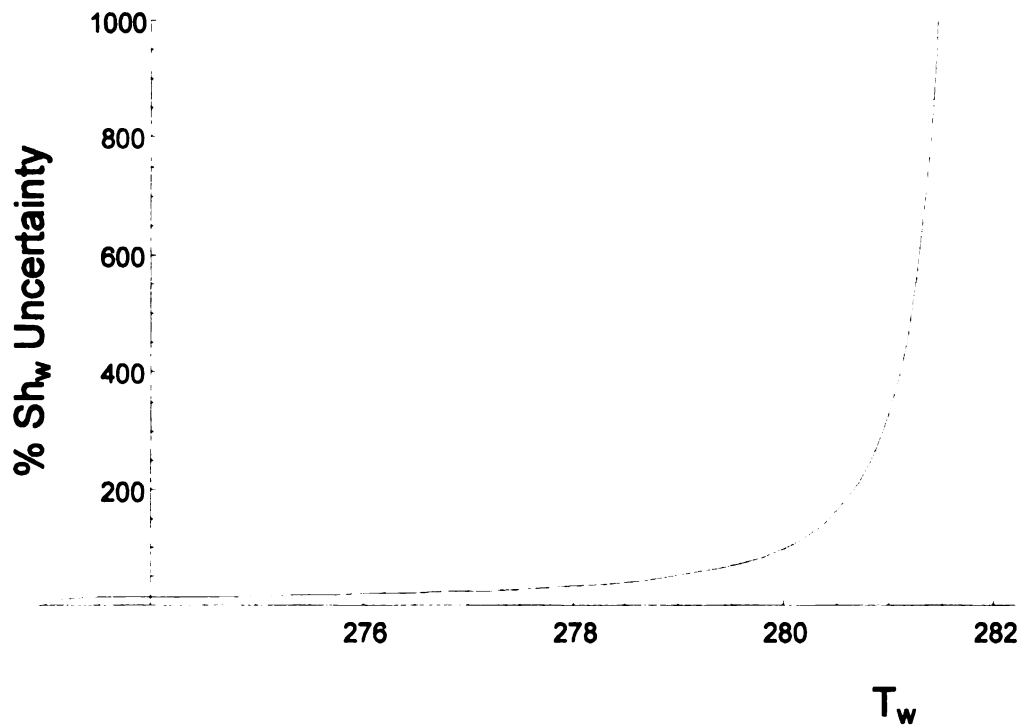


**Figure 7.13.** Percent uncertainty in the experimental Sherwood number results as a function of the temperature of the thermally active wall surface ( $T_s$ ).

$T_{\text{dew-point}} \sim 283 \text{ K.}$

The uncertainty in the Sherwood number is great enough to reduce the usefulness of the comparison, especially when the surface temperature is near the dew-point of the wall jet flow. Table 7.2 presents the contributions to the total error for typical experimental conditions.

**Table 7.2. Contribution of the experimental variables to the total uncertainty.**

<b>Parameter</b>	<b>Value</b>	<b><math>(S_x dx)^2</math> @ <math>T_w = 10.0</math> °C</b>	<b><math>(S_x dx)^2</math> @ <math>T_w = 8.0</math> °C</b>
$T_w$	10.0, 8.0 °C	6023	132
$T_j$	24 °C	5517	152
$Rh_j$	46%	13860	381
$w$	.02 m	25.2	4.2
$D$	$2.48 \times 10^{-5}$ m <sup>2</sup> /s	2.6	0.45
$\Psi_1$	2.0 $\mu$ m	332	53.9
$\Psi_2$	3.9 $\mu$ m	332	53.9
$\Delta t$	10 s	100.7	16.8
% $w/\Delta C$		96.9%	83%
% $w/\Delta \Psi$		2.5%	13.6%
$Sh_w$	142, 82	200.6	25

The experimental parameters involved with the determination of the concentration difference in the flow constitute the majority of the uncertainty in the Sherwood number calculation. The relative humidity measurement is the single largest contributor to the uncertainty. The current system utilized in the facility is a chilled mirror system that cost \$2500 with an accuracy of  $\pm 1.25\%$ . Clearly, more accurate determination of the relative humidity in the jet and the jet and test surface temperatures would greatly enhance the Sherwood number determination.

The lowest attainable uncertainty with typical experimental parameters decreases to approximately  $\pm 22\%$  when the test surface temperature decreases to 2 °C. However, the optical infrared reflectance technique sensitivity to condensate is great enough that the measurement is saturated well before the surface temperature is reduced that far. The strength of the optical infrared



reflectance technique is detecting and measuring transient, local condensate thickness on the surface of interest. Improved estimates of the Sherwood number would depend on developing an independent and more accurate method to determine the concentration difference in the flow field. Such a method would replace monitoring the thermally active test surface temperature.

## **Chapter 8**

### **SUMMARY**

The original motivation for this project was to develop benchmark data for use as a calibration and validation tool for a computational fluid dynamics model utilized in automotive defroster/demister design. The developing region of a two-dimensional wall jet was selected as a model flow field and a facility was constructed.

The isothermal, wall jet flow field was initially studied in the experimental facility. Hot-wire anemometry was utilized to survey the flow at the jet orifice and five downstream locations. The measurement results were compared to data from the literature to validate the facility and the measurement techniques utilized. The mean velocity profile in the Ford-MSU test facility conformed to the canonical self-preserving, two-dimensional wall jet profile at streamwise locations greater than  $x/w > 7.62$ .

Comparison of the experimental results with the computed results indicates that the CFD model, with both the Reynolds stress and the  $k-\epsilon$  turbulence models, over-predicted the velocity gradient at the wall and the inner layer boundary growth rate. The jet spreading rate, as measured by  $\delta_2$ , was under predicted by the CFD model by approximately 30%. The discrepancy in the inner boundary layer and specifically in the velocity gradient at the wall surface is critical to successfully model the heat and mass transfer. This

discrepancy indicates that the model will over-predict the heat and mass transfer at the surface.

The non-isothermal, non-condensing ( $T_s > T_{\text{dew-point}}$ ) flow was investigated next. Hot and cold-wire anemometry were utilized during this experimental phase. The cold-wire probe provided temperature measurements in the flow. The cold-wire data were also utilized to temperature compensate the hot-wire velocity measurements. Hot-wire and cold-wire measurements were conducted at the same streamwise locations as the isothermal experiments. The velocity data were found to agree with the isothermal measurements to within the experimental uncertainty. This result was expected from Reynolds number – Grashoff number comparisons and the small property variations associated with the small temperature changes in the experimental flow field. This result also indicated that a decoupled momentum and energy solution technique could be utilized in the computational model with the introduction of minimal error.

Only the experimental temperature data were compared to the CFD result since the velocity data from the experiment and the CFD were unchanged. The computational model over-predicted the temperature gradient at the wall surface and the growth rate of the thermal boundary layer (as measured by  $\delta_T$ ) by approximately 30% and 10% respectively. This level of agreement is approximately equal to the results from the velocity comparison. The thermal penetration from the surface into the flow is controlled by the transport properties in the inner boundary layer and therefore, this level of agreement is expected.

The non-isothermal, condensing ( $T_s < T_{\text{dew-point}}$ ) flow regime was investigated next. Velocity and temperature profiles were obtained at the orifice and at the streamwise location  $x/w = 10.8$ . It was found that the velocity profile again agreed with the isothermal measurements to within the experimental uncertainty. This result was again expected due to the Reynolds – Grashoff number comparison, the small property changes in the flow, and the low mass transfer rate. The mass transfer velocity to the surface is 0.3% of the jet velocity and was not anticipated to effect the velocity profile.

A measurable offset was detected in the near wall temperature profile at  $x/w = 10.8$  between the non-isothermal, non-condensing tests and the non-isothermal, condensing experiments. This result is consistent with results in the literature for flows with condensation phase change [Legay-Desesquelles and Prunet-Foch, 1986]. This increase is the result of the enhanced heat transfer resulting from the latent heat released at the wall surface.

Steady state condensation to the thermally active test section was investigated next. The average mass transfer coefficient was determined to be  $h_m = 0.031$  m/s. Later studies of the temperature of the test surface indicate that the mass transfer in the steady state case is under-predicted due to temperature variations of the thermally active surface. A corrected estimate of the mass transfer coefficient of  $h_m = 0.0407$  m/s is deduced based on the observed temperature variations of the thermally active test surface.

A novel optical mass transfer tool was developed in the next phase of the experimental work to study the early transient stages of the condensation

phenomena. Infrared measurements of the surface reflectance were found to be highly sensitive to the presence of condensation on the reflective surface. The apparent surface reflectance was calibrated as a function of the measured thickness of water on the aluminum targets. A new technique to measure small quantities (<5 mg) of H<sub>2</sub>O was developed to facilitate this calibration.

The IR-H<sub>2</sub>O reflectance technique was determined to be very sensitive to condensate thickness and was capable of obtaining transient condensate thickness measurements. The technique has a measurement range of 0-5  $\mu\text{m}$  and is accurate (on calibrated surfaces) to  $\pm 0.17 \mu\text{m}$  at a 95% confidence interval. The technique has limited usefulness in determining the mass transfer coefficient due to the uncertainty associated with the concentration difference in the flow field. Small errors in the temperature ( $\sim 0.2^\circ\text{C}$ ) can result in orders of magnitude shifts in the uncertainty in the mass transfer coefficient, especially when the temperature of the surface is near the dew-point temperature of the flow.

The IR-H<sub>2</sub>O reflectance technique was applied to the developing wall jet flow field in the Ford-MSU test facility. It was found that the mass transfer coefficient measurements were consistent with the expected Reynolds number dependence. The results did not show the expected laminar transition to a turbulent profile but did conform to a turbulent  $\text{Re}_x^{0.8}$  type profile. The difference between the published results and the data obtained in the FMTF could be the effect of the facility design on the developing region. The particular facility nozzle geometry and flow conditioning have been noted to influence the jet up to 25 jet

widths downstream of the jet exit [Mabuchi and Kumada, 1972]. This is consistent with the results published by Hsiao and Sheu [1996] who determined that the transition region in a two dimensional wall jet flow develops from 3 to 24 slot widths downstream of the jet exit. Akfirat [1966] also presents evidence that the transition region can begin upstream of the nozzle exit. No measurements of the heat or mass transfer coefficient were made above  $x/w = 0.0$  in this study. The transient measurements obtained with the optical infrared reflectance technique do agree with the steady state results obtained in the same facility. This indicates that the variation from the literature is the direct result of the facility and that the optical technique is functioning as expected.

The benchmark data set has been obtained and supplied to Ford Motor Company. A new technique to measure small aliquots of water ( $< 5$  mg) was developed to facilitate the development of a novel optical condensate measurement tool. An optical infrared reflectance technique was developed to measure condensate on a reflective surface. The technique proved to be highly sensitive and provided a 0 - 5  $\mu\text{m}$  condensate thickness measurement range. The optical infrared reflectance technique was applied in the Ford-MSU test facility flow to measure the mass transfer to the thermally active test surface. These results concluded the project and indicated that the development of the optical technique was a success.

## **8.1 FUTURE WORK**

**Six recommendations are made concerning future work with and development of the optical infrared reflectance technique. These are primarily concepts to expand the capabilities of the technique, improve the determination of the Sherwood number and to apply the method to other flows of interest related to this project.**

- 1. Development of a more accurate method to determine or control the concentration difference between the flow and the surface of interest. The largest contribution to the experimental uncertainty is the concentration difference. New concentration measurement techniques could greatly enhance the capabilities of the technique. Utilizing a dry nitrogen environment in a closed wind-tunnel system would allow a precise amount of water to be delivered and evaporated into the environment. This technique would allow much more precise determination of the concentration difference between the test surface and the flow field and reduce the uncertainty associated with the Sherwood number. Coupling this technique with more accurate surface temperature measurements would further improve results.**
- 2. Verification of the assumptions regarding distance and angle on the condensate thickness – reflectance correlation. This would be critical at short viewing distances or with optics that would decrease the infrared camera pixel area to an order of magnitude where droplet features and patterns on the surface could effect the correlation result.**

3. **Application on glass.** To apply the technique in an actual automotive defroster/demister test, determination of the condensate thickness – reflectance correlation would be necessary. The Inframetrics IR camera used in the present experiments is not sufficient for this procedure due to the limited (8 bit) range. The low reflectance ( ~ 10%) of automotive glass to infrared radiation would necessitate the use of a higher resolution infrared detector. Note that a higher resolution camera would also extend the condensate thickness measurement range of the technique on more reflective surfaces.
4. **Defroster/demister performance testing.** As detailed in the present work, FMVSS103 specifies measuring the “dry” areas of the windshield during defroster performance tests. The test begins with 500  $\mu\text{m}$  of ice on the windshield which is much larger than the dynamic range of the optical infrared reflectance technique. As the test proceeds, this layer melts and areas of the windshield become dry. The optical infrared reflectance technique could determine which areas of the windshield contained less than 5  $\mu\text{m}$  of condensate quantitatively and aid in engineering analysis.
5. **Validation of the technique in a canonical flow field.** Further testing of the optical infrared reflectance technique in previously well characterized flow field would further strengthen the results of the present work. A flat plate boundary layer flow undergoing transition would provide an ideal test environment, especially if the concentration difference in the flow could be resolved precisely.



**6. The thin film model indicates that the dynamic range of optical infrared reflectance technique is dependent on the absorptivity in water of the wavelengths utilized for the reflectance measurement. This assumption is supported by the visible light spectrum results obtained by Bearman et. al. [1998] and the near infrared work performed by Anderson et. al. [1996]. Preliminary tests utilizing a 3.2 - 5.1  $\mu\text{m}$  detector were conducted as a portion of this work. The effect on the dynamic range was not conclusively discernible from the tests conducted however due to complications that arose with the gas chromatography equipment and the fact that the absorptivity coefficient is only 15% different over the wavelengths utilized.**

**The future work proposed would expand the potential applications of the technique developed here and further verify and define the accuracy and resolution in various test environments. The strength of the technique is the measurement of condensate thickness on the surface of interest. Application of the technique in defroster/demister test environments could greatly enhance the data available regarding visibility and driver safety and result in improved testing methodologies.**

## **APPENDICES**

## APPENDIX A

### COLD WIRE CALIBRATION METHODOLOGY

A cold-wire probe, shown schematically in Figure A.1, is constructed from a thin metallic wire material (5  $\mu\text{m}$  diameter tungsten wire was utilized at the FMTF) whose resistance is a function of temperature. The temperature-resistance relationship can then be obtained through a calibration so that the sensor can be utilized to measure temperature fluctuations in a flow field of interest. The resistance of the sensor is measured by passing a fixed, small ( $\sim 1\text{mA}$ ) sensing current through the probe. The resistance of the cold-wire probe can then be monitored by measurement of the voltage drop across the probe.

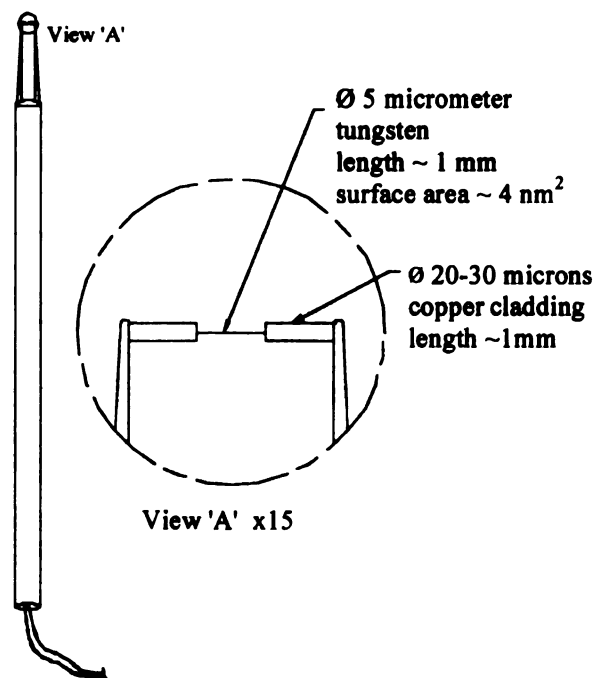


**Figure A.1.** Schematic of a cold-wire probe.

**A cold-wire calibration system was constructed and validated to improve measurement accuracy and to eliminate the need for external cold-wire calibration or the purchase of a calibration system. Four design objectives were decided upon and consisted of**

- 1. An economical device that can be incorporated into the existing FMTF facility.**
- 2. Allow for cold-wire calibrations in less than 1 hour.**
- 3. Incorporate 4 calibration points with differences of at least 5 °C.**
- 4. Generate a spatially uniform, steady state temperature profile for each calibration point.**

**The design presented in Figure A.2 was completed to meet these objective targets [M. Desjardins, 2001]. Common materials were utilized to obtain the most economical device possible. Stainless steel screening was utilized to heat two of the airflow paths and a coiled, copper heat exchanger cooled the airflow in one chamber. The screen heaters and the copper heat exchanger in the temperature conditioning section are shown in Figure A.3. Axisymmetric nozzles cut from soda bottles were utilized to accelerate the flow to good effect due to the high contraction ration (20:1). The exit velocity profile of this nozzle is very uniform and had been previously characterized for hot-wire calibration [Hoke, 1998]. The cold-wire calibration device is presented in Figure A.4.**

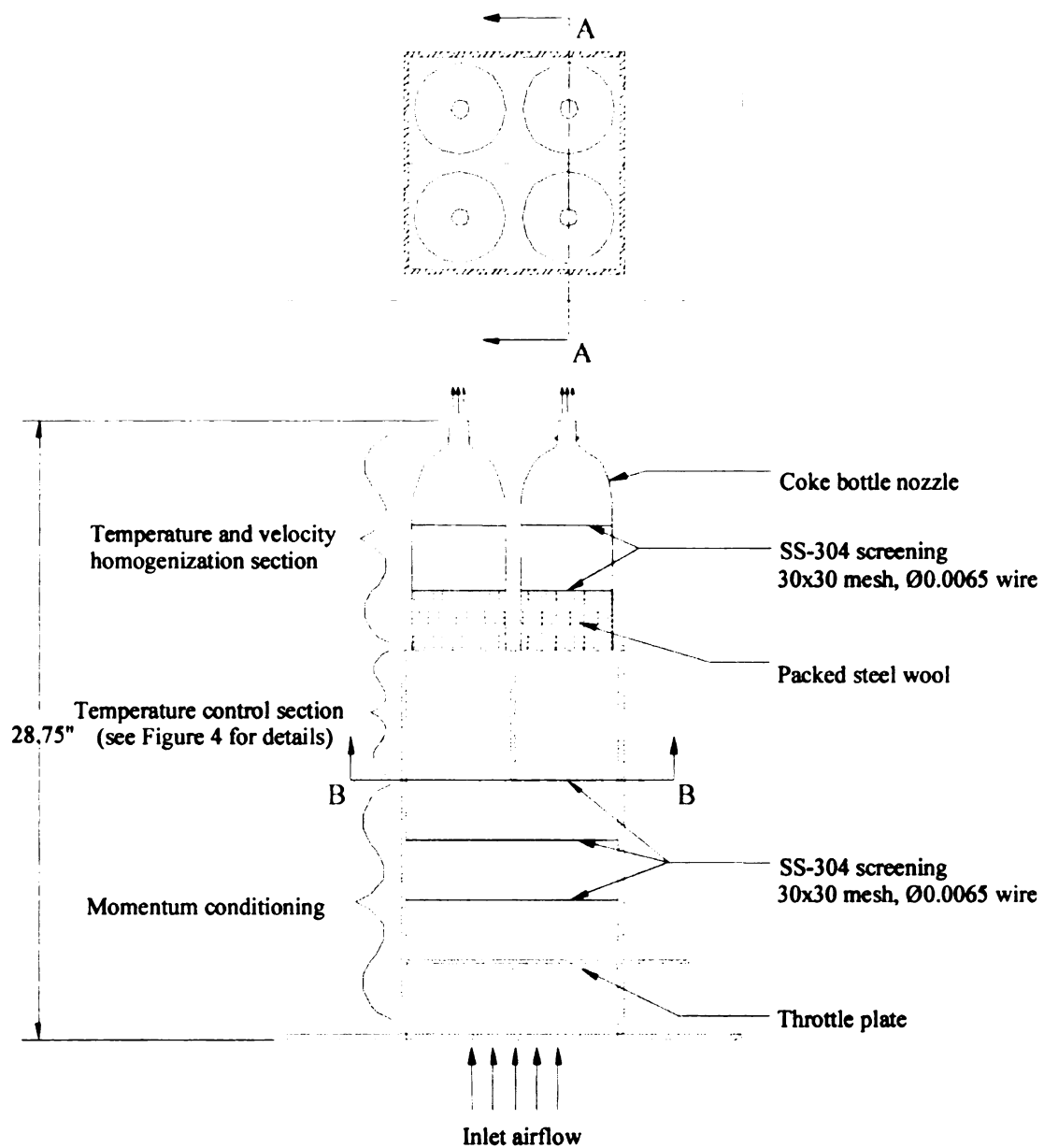


**Figure A.2. Schematic of the cold-wire calibration device.**

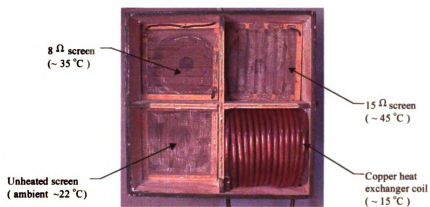


**Figure A.3.** Temperature conditioning section of the cold-wire calibrator.

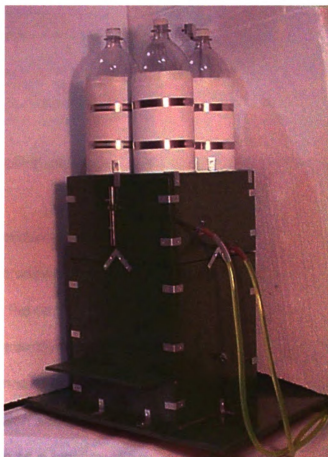


**Figure A.4.** Cold-wire calibration device.

Temperature profiles at the exit of the four nozzles were then taken with a mechanical traverse system and a thermocouple. The results of these measurements are presented in Figure A.5. The temperature scale in Figure A.5 has been adjusted by subtracting the ambient temperature since the offset between each nozzle is independent of the day to day drift in the ambient temperature.

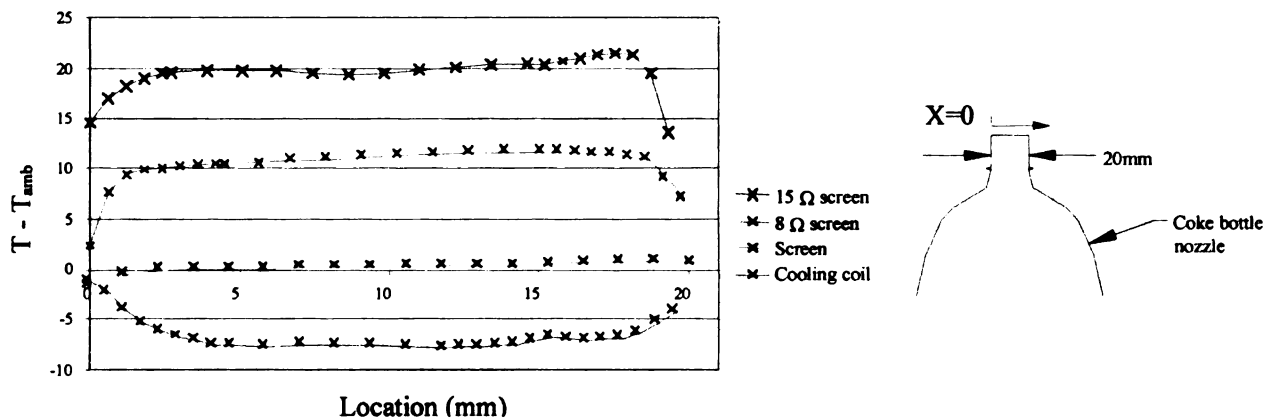


**Figure A.5.** Temperature profiles at the exit plane of the four calibration nozzles.

Although the temperature profiles are not perfectly flat in the center portions of the nozzles, the spatial variation was deemed acceptable since it was less than 1 °C / mm in the central portion of each nozzle and the local temperature is measured independently for reference during the calibration process.

The convergence of the temperature measurement was studied to assess the limit of the calibration accuracy. The time-averaged (mean) temperature and standard deviation as a function of time are presented in Figure A.6.

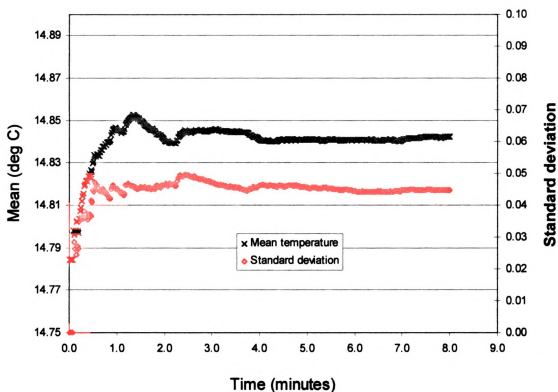


**Figure A.6.** Time-averaged mean temperature and standard deviation of the cold wire measurement as a function of time.

The uncertainty in the mean temperature utilized for the cold-wire calibration can be calculated as [Neter et al., 1993]

$$\bar{X} - \mu < \left| \frac{t_{\alpha} \sigma}{\sqrt{n}} \right| \quad (\text{A.1})$$



**The uncertainty in the mean temperature calculated using Equation (A.1) converges to less than 0.1 °C when two minutes of temperature data collected with the reference thermocouple are utilized. Thus the expected accuracy of the cold-wire measurement is expected to be better than 1 °C.**

**Cold-wire calibration is conducted with the following procedure:**

- 1. Electrical power to the cold-wire calibrator and the FMTF flow are initiated and allowed to stabilize for 30 minutes.**
- 2. The cold-wire is positioned over the first nozzle and 2 minutes of data are collected.**
- 3. Step 2 is repeated for each nozzle.**
- 4. Mean temperature from the reference thermocouple is plotted as a function of the mean voltage output of the cold-wire in Excel® and a linear regression model is fit to the data.**
- 5. Results of the linear regression model are inputted into the IFA 300 Thermopro software for use with the calibrated cold-wire.**
- 6. The cold-wire is now ready for use in experiments.**

**The author would like to acknowledge and thank M. Desjardins for her efforts during the cold wire calibrator development.**

## **APPENDIX B**

### **EQUIPMENT AND SETTINGS UTILIZED FOR REFLECTANCE CALIBRATION EXPERIMENTS**

The following is a listing of equipment and equipment settings utilized in the development and application of the optical infrared reflectance condensate measurement technique,

**Inframetrics 600L infrared camera**

**Emissivity set to 1.0**

**Ambient temperature adjusted to match environment (typically ~22.5 °C)**

**Temperature range - 50 °C (typically 0 °C to 50 °C was utilized)**

**External optics: NONE**

**For.A VTG-33 video timer**

**75 ohm switch- ON**

**Sony Trinitron Monitor**

**Panasonic AG-2400 Video cassette recorder**

**Image Pro Plus - v.4.1**

**Brightness Setting- 37**

## **Contrast Setting- 55**

**Image averaging - acquire 9 images and divide by 9.**

**A 5.0 liter/minute airflow meter (Cole Parmer) is utilized to regulate the chilled nitrogen airflow to the copper heat sink. The flow rate is set at 4 liters/minute. The nitrogen airflow is chilled by circulation in a copper tube heat exchanger (manufactured in the laboratory) submerged in a dewar filled with liquid nitrogen.**

**A Hewlett Packard HP-6645A power supply connected to an Omega Engineering OmegaLux SRFG 305/10 heater. The heater is thermally bonded (Omega OT-201 thermal paste) to a 0.030" thick aluminum plate that has been painted black. The heater and the aluminum plate are 3" x 5".**

**A BK Precision 1730 DC supply connected to a Tellurex Corporation CZ-1.0-127-1.27 Peltier device. The system is allowed to cool for 4 to 5 minutes with only the nitrogen airflow. Then 0.5 amps were provided to the Peltier device. The temperature of the aluminum target was monitored by a thermocouple mounted to the surface of the mechanical holder. This temperature was monitored to insure that the surface did not reach the freezing point (0 °C).**

**The aluminum calibration target was then dropped in to a 22 ml headspace vial and saved for future analysis with the HS-GC-FID technique outlined in Chapter 6.**

## **APPENDIX C**

### **CONTROL SETTINGS UTILIZED FOR HS-C-GC-FID.**

A Perkin-Elmer Autosystem gas chromatograph (Perkin-Elmer Corporation, Norwalk, Conn.) with an integrated flame ionization detector was utilized for all gas chromatography measurements performed. The GC-FID system was interfaced with a computer running PE-Nelson Turbochrom 4.1 (Perkin-Elmer Corp.) chromatography data-acquisition and control software. All peak area measurements were performed with this software.

The control settings and equipment configuration for the GC-FID system utilized for all measurements are presented below:

<b>Sample temperature</b>	<b>Ambient ~ 22 °C</b>
<b>Isothermal Time 1</b>	<b>4 min</b>
<b>Oven temperature</b>	<b>40 °C</b>
<b>Injection volume</b>	<b>25 µL</b>
<b>Injection port temperature</b>	<b>250 °C</b>
<b>FID detector temperature</b>	<b>250 °C</b>
<b>Column</b>	<b>PE-624 - 30m x 0.53 mm megabore</b>
<b>column</b>	
<b>H<sub>2</sub> Supply Pressure</b>	<b>41.5 psi</b>
<b>Air supply pressure</b>	<b>60 psi</b>
<b>Carrier gas (N<sub>2</sub>) supply pressure</b>	<b>90 psi</b>
<b>Carrier gas (N<sub>2</sub>) flow rate</b>	<b>10 mL/min</b>

Manual injection was performed using a 100  $\mu\text{L}$  Pressure-Lok<sup>®</sup> precision analytical syringe (Precision sampling, Inc. Baton Rouge, LA.). The syringe and an example of the 22 mL headspace vials utilized are presented in Figure C.1.

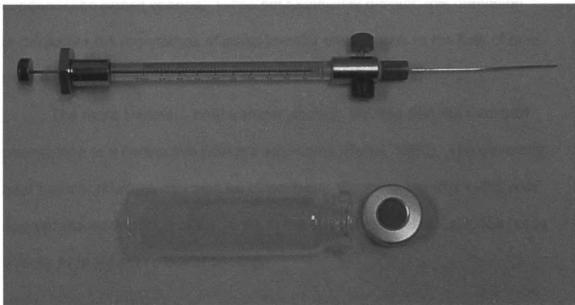


**Figure C.1.** Analytical syringe and 22 mL headspace vial and crimp cap utilized for chromatography experiments.

Calcium carbide ( $\text{CaC}_2$ ) was added to every sample to convert the water present to acetylene ( $\text{C}_2\text{H}_2$ ) as detailed in Chapter 6. This gas in the headspace of the vial was then sampled with the syringe and injected into the port on the PE Autosystem gas chromatography machine. Sample volumes of 25  $\mu\text{L}$  were found to optimize the dynamic range of the system for the concentrations utilized.

## **APPENDIX D**

### **COMPARISON OF THE HEAT TRANSFER ASSOCIATED WITH THE PHASE CHANGE EVENT TO THE SENSIBLE HEAT TRANSFER**

The following is a derivation of the heat transfer associated with condensation phase change. While not technically difficult, this derivation underscores the importance of mass transfer phenomena to the field of heat transfer and is therefore included for completeness.

The mass transfer - heat transfer analogy dictates that the transport phenomena in a convective flow are equivalent [Bejan, 1995]. The governing heat transfer relations can also be extended to the mass transfer event with appropriate modification of the terms in the equations. This substitution leads directly from Newton's law of cooling,

$$q'' = h\Delta T, \quad (D.1)$$

to Fick's law of mass diffusion,

$$j'' = h_m \Delta C. \quad (D.2)$$

. This equivalence leads to the following relationship between the heat transfer coefficient ( $h$ ) and the mass transfer coefficient ( $h_m$ ) [Incorpera and Dewitt, 1990]:

$$\frac{h}{h_m} = \frac{k}{D_{AB} Le^n} = \rho c_p Le^{1-n}, \quad n \sim \frac{1}{3}. \quad (D.3)$$

For a phase change event with water vapor in air, the Lewis Number ( $Le = \alpha/D$ ), thermal conductivity ( $k$ ) and the diffusivity ( $D_{AB}$ ) are approximately equal to 0.82, 0.025 W/(mK) and  $2.52 \times 10^{-5} \text{ m}^2/\text{s}$  respectively. This results in a mass transfer coefficient approximately of  $1/1000^{\text{th}}$  of the numerical value of the heat transfer coefficient. That is, if the heat transfer coefficient is approximately 40 W/(m<sup>2</sup>K), the mass transfer coefficient would be 0.040 m/s. Note that the term on the relation on the right hand side of Equation (D.3) is not dimensionless.

The latent heat ( $L$ ) released or absorbed during a mass transfer process can then be utilized to calculate the heat transfer associated with the mass transfer.

$$q_m'' = Lj'' = Lh_m \Delta C \quad (D.4)$$

The concentration difference in the flow can be driven by several factors including the temperature gradient, chemical absorption, or flow stratification. The temperature gradient is responsible for the concentration difference in the windshield defroster/demister application and in the experiments conducted in the Ford-MSU test facility. Therefore, the water concentration in the wall jet and

at the thermally active test surface must be calculated from the relative humidity and the temperature gradient present in the flow field.

The concentration of the wall jet is calculated directly from the measured jet temperature and relative humidity (%Rh or  $\phi$ ). The concentration at the surface of the thermally active test section is inferred based on the assumption of thermodynamic equilibrium and the measured surface temperature. Initially, the saturation pressure is calculated utilizing the Clausius-Clapeyron relationship [Çengal and Boles, 1994]

$$P_{2\text{ sat}} = P_{\text{ref}} e^{\left( \frac{h_{fg}}{R} \left( \frac{1}{T_{\text{Ref}}} - \frac{1}{T_2} \right) \right)} \quad (\text{D.5})$$

Once the saturation pressure is calculated, the specific humidity ( $\omega$ ) is calculated:

$$\omega = \frac{0.622 \% \text{Rh } P_{\text{sat}}}{P_{\text{Tot}} - P_{\text{sat}}} \quad (\text{D.6})$$

Note that the relative humidity for the jet is measured directly in the experiment and assumed to be equal to 100% at the wall surface during active condensation. The specific humidity provides the concentration in units of



kg(H<sub>2</sub>O)/kg(air) and thus the concentration in the units kg/m<sup>3</sup> can be obtained by multiplying by the local density.

The concentration difference in the flow ( $\Delta C$ ) can then be written by combining Equation (D.5) and Equation (D.6):

$$\Delta C = (\omega \rho)_j - (\omega_s \rho)_s =$$

$$= 0.622 P_{\text{Ref}} \left( \frac{\rho_j \% R h_j e^{\left( \frac{h_{fg}}{R} \left( \frac{1}{T_{\text{Ref}}} - \frac{1}{T_j} \right) \right)}}{P_{\text{Tot}} - P_{\text{Ref}} e^{\left( \frac{h_{fg}}{R} \left( \frac{1}{T_{\text{Ref}}} - \frac{1}{T_j} \right) \right)}} - \frac{\rho_s e^{\left( \frac{h_{fg}}{R} \left( \frac{1}{T_{\text{Ref}}} - \frac{1}{T_s} \right) \right)}}{P_{\text{Tot}} - P_{\text{Ref}} e^{\left( \frac{h_{fg}}{R} \left( \frac{1}{T_{\text{Ref}}} - \frac{1}{T_s} \right) \right)}} \right) \quad (\text{D.7})$$

The density can be calculated from the local temperature utilizing the ideal gas law. The Clausius-Clapeyron equation is not exact however and slight error is included in its application. This error becomes evident when the ideal gas law is combined with Equation (D.7) and the concentration difference is small (for example, at the onset of condensation). In these circumstances, the average density of the flow was utilized to maintain consistently positive (>0) concentration difference. The acceptability of this application is drawn from the fact that often condensation was observed to form even when Equation (D.7) and the ideal gas law indicated negative concentration difference.

## **APPENDIX E**

### **CATALOG OF CONDENSATION AND MASS TRANSFER MEASUREMENTS OBTAINED WITH THE OPTICAL INFRARED REFLECTANCE TECHNIQUE.**

The following figures contain the condensate thickness and temperature data and the resulting Sherwood number calculations for the transient condensation experiments conducted in the Ford-MSU test facility. Note that the specific conditions of each test varied slightly and certain experimental features could not be reproduced between experiments (such as the temperature of the thermally active test surface). In spite of this test to test variation, the condensate thickness measurements between experiments present consistent development patterns. The condensate thickness development rates differ by less than 5% for experiments with similar wall jet temperature and humidity levels. This repeatability is further demonstrated when the Sherwood number results for different tests are overlaid. Specifically Figure 7.9, which compares Sherwood number results obtained on different (but overlapping) sections of the thermally active test surface.

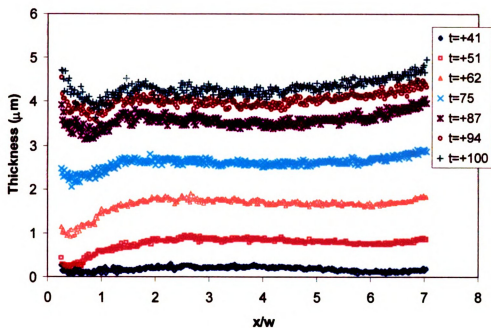


**Figure E.1.** Thickness results for  $Re_w = 6560$  test  
(11 June 2001. Experiment #2).

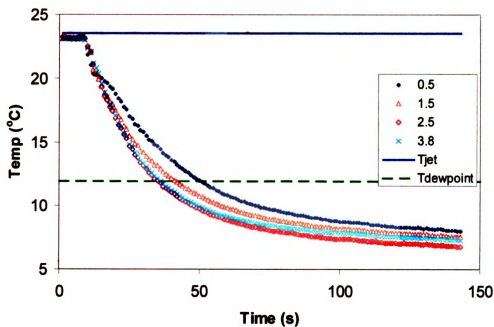


**Figure E.2.** Temperature log for  $Re_w = 6560$  test (11 June 2001. Experiment #2).

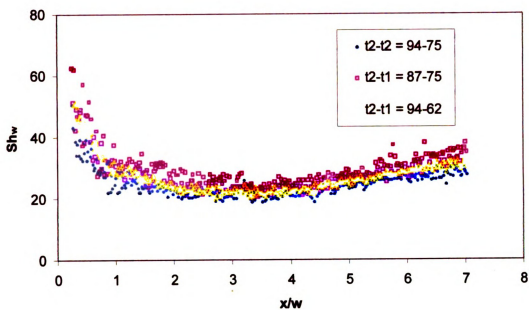


**Figure E.3.** Sherwood number results for  $Re_w = 6560$  test (11 June 2001, Experiment #2).

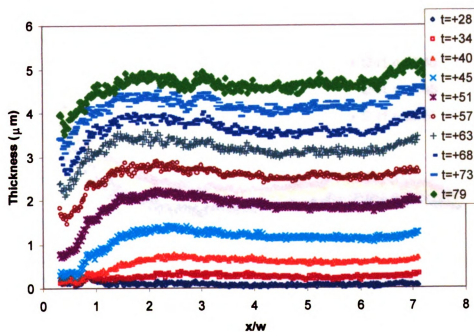


**Figure E.4.** Thickness results for  $Re_w = 8400$  test (15 June 2001, Experiment #4).

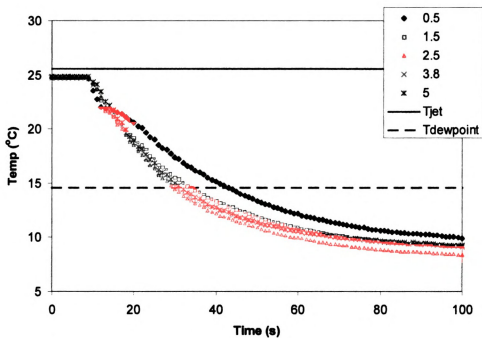


**Figure E.5.** Temperature log for  $Re_w = 8400$  test (15 June 2001. Experiment #4).

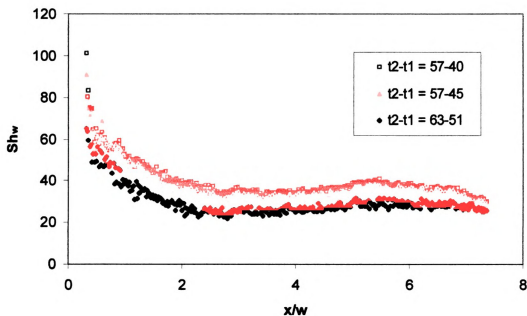


**Figure E.6.** Sherwood number results for  $Re_w = 8400$  test  
(15 June 2001. Experiment #4).

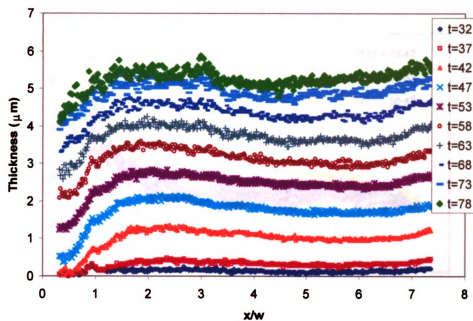


**Figure E.7.** Thickness results for  $Re_w = 10200$  test  
(15 June 2001. Experiment #3).

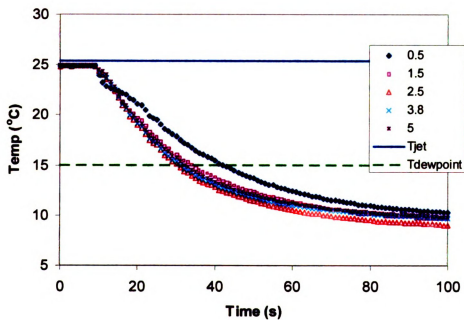


**Figure E.8.** Temperature log for  $Re_w = 10200$  test (15 June 2001. Experiment #3).



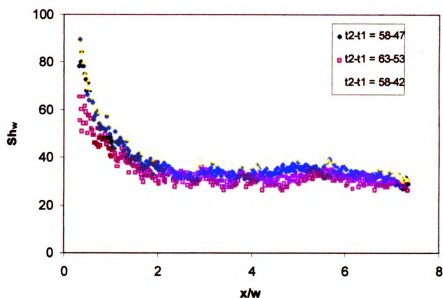


**Figure E.9.** Sherwood number results for  $Re_w = 10200$  test (15 June 2001.  
Experiment #3).

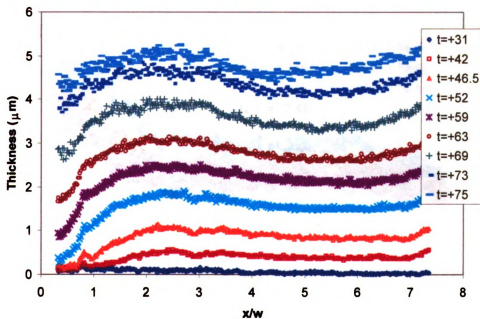


**Figure E.10.** Thickness results for  $Re_w = 13300$  test  
(15 June 2001. Experiment #2).





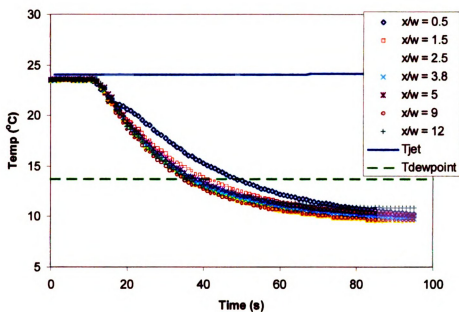


**Figure E.11.** Temperature log for  $Re_w = 13300$  test  
(15 June 2001. Experiment #2).

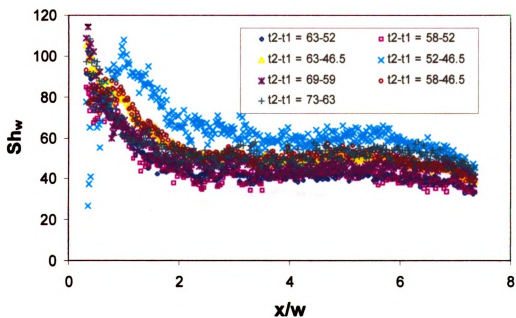


**Figure E.12.** Sherwood number results for  $Re_w = 13300$  test (15 June 2001.  
Experiment #2).

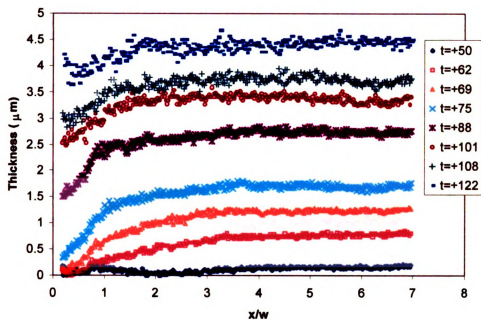


**Figure E.13.** Thickness results for  $Re_w = 13300$  test

(5 June 2001. Experiment #1).

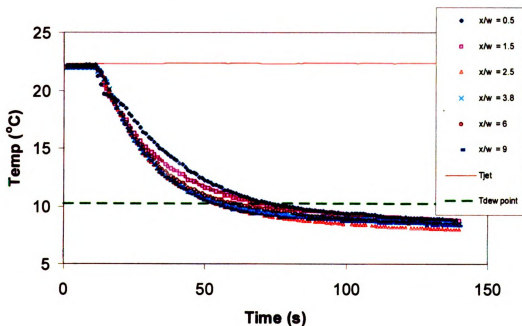


**Figure E.14.** Temperature log for  $Re_w = 13300$  test

(5 June 2001. Experiment #1).

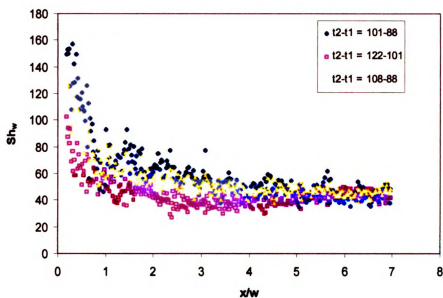


**Figure E.15.** Sherwood number results for  $Re_w = 13300$  test  
(5 June 2001. Experiment #1).

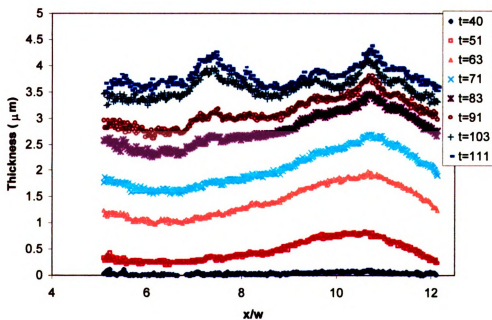


**Figure E.16.** Thickness results for  $Re_w = 13300$  test  
(20 June 2001. Experiment #1).

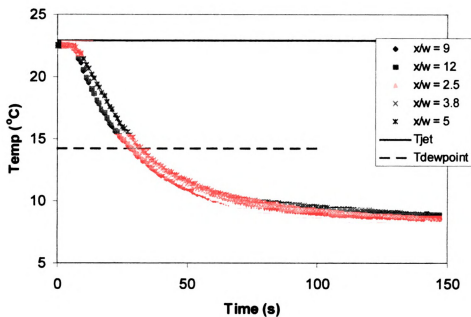


**Figure E.17.** Temperature log for  $Re_w = 13300$  test  
(20 June 2001. Experiment #1).

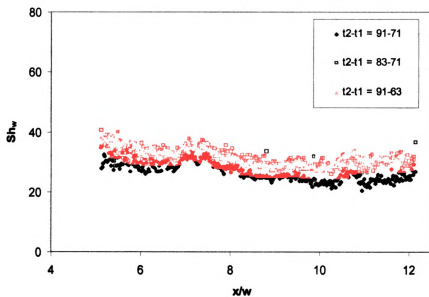


**Figure E.18.** Sherwood number results for  $Re_w = 13300$  test (20 June 2001.  
Experiment #1).

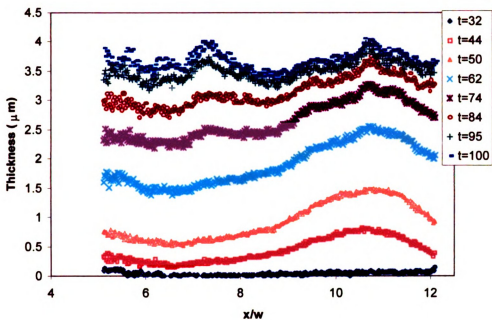


**Figure E.19.** Thickness results for  $Re_w = 13300$  test (20 June 2001, Experiment #2).

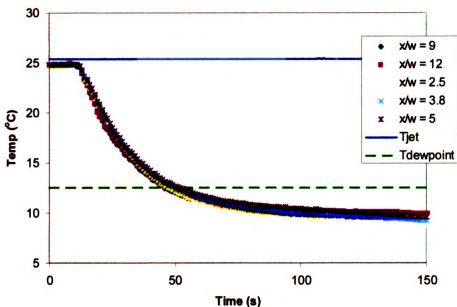


**Figure E.20.** Temperature log for  $Re_w = 13300$  test (20 June 2001, Experiment #2).



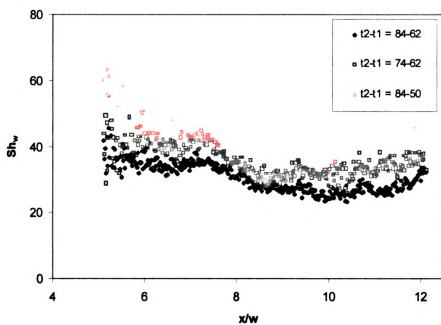


**Figure E.21.** Sherwood number results for  $Re_w = 13300$  test (20 June 2001. Experiment #2).



## APPENDIX G

### ERROR ANALYSIS IN THE SHERWOOD NUMBER DETERMINED WITH THE OPTICAL INFRARED REFLECTANCE TECHNIQUE.

The following program written in Mathematica<sup>®</sup> was utilized to calculate the uncertainty in the Sherwood number. The uncertainty is the result obtained with the optical infrared reflectance technique for the test conditions utilized on 15 June, 2001. That experiment was typical of the conditions utilized for tests contained in this thesis. Statements have been added to clarify the input to and output from the program.

```
Clear[Sh, w, Dif, Ptot, Psatj, Psatw, Wj, Ww, Rair, Rwater, Tj, Tw, hm, Pref,
      Tref, Rhj, Delt, T2, T1]
Psatj[Tj_] = Pref * e^((hfg/.461) * (1 / Tref - 1 / Tj));
Psatw[Tw_] = Pref * e^((hfg/.461) * (1 / Tref - 1 / Tw));
Wj[Psatj_, Rhj_] = 0.622 * Rhj * Psatj[Tj] / (Ptot - Rhj * Psatj[Tj]);
Ww[Psatw_] = 0.622 * Psatw[Tw] / (Ptot - Psatw[Tw]);
Cj[Wj_, Psatj_, Tj_] = (Wj[Psatj, Rhj] * (Ptot - Psatj[Tj])) / (Rair * Tj);
Cw[Ww_, Psatw_, Tw_] = (Ww[Psatw] * (Ptot - Psatw[Tw])) / (Rair * Tw);
hm[T1_, T2_, Delt_, Cj_, Cw_] =
  (T2 - T1) * r / ((Cj[Wj, Psatj, Tj] - Cw[Ww, Psatw, Tw]) * Delt);

Sh[hm_, Dif_, w_] =
  hm[T1, T2, Delt, Cj[Wj[Psatj, Rhj], Psatj[Tj], Tj],
    Cw[Ww[Psatw], Psatw[Tw], Tw]] * w / Dif;
Sh[hm, Dif, w]
```

**The resulting form of the Sherwood number:**

$$\left( (-T_1 + T_2) w \rho \right) / \left( \text{Delt Dif} \right. \\ \left. \left( \left( 0.622 e^{2.1692 hfg \left( -\frac{1}{T_j} + \frac{1}{T_{ref}} \right)} P_{ref} \left( -e^{2.1692 hfg \left( -\frac{1}{T_j} + \frac{1}{T_{ref}} \right)} P_{ref} + P_{tot} \right) \right. \right. \right. \\ \left. \left. \left. Rhj \right) / \left( R_{air} \left( P_{tot} - e^{2.1692 hfg \left( -\frac{1}{T_j} + \frac{1}{T_{ref}} \right)} P_{ref} Rhj \right) T_j \right) - \right. \right. \\ \left. \left. \frac{0.622 e^{2.1692 hfg \left( \frac{1}{T_{ref}} - \frac{1}{T_w} \right)} P_{ref}}{R_{air} T_w} \right) \right) \right)$$

**The various sensitivity coefficients are then calculated:**

**(\*\* Error analysis in the Sherwood calculation \*\*)**

**(\*\* Sensitivity Coefficients \*\*)**

**STj[Tw\_] = D[Sh[hm, Dif, w], Tj];**

**STw[Tw\_] = D[Sh[hm, Dif, w], Tw];**

**SRhj[Tw\_] = D[Sh[hm, Dif, w], Rhj];**

**Sw[Tw\_] = D[Sh[hm, Dif, w], w];**

**SDif[Tw\_] = D[Sh[hm, Dif, w], Dif];**

**ST1[Tw\_] = D[Sh[hm, Dif, w], T1];**

**ST2[Tw\_] = D[Sh[hm, Dif, w], T2];**

**SDelt[Tw\_] = D[Sh[hm, Dif, w], Delt];**

The following is the output for sensitivity coefficient for the jet temperature (T<sub>j</sub>):

$$\begin{aligned}
 & \left( \begin{aligned} & (-T_1 + T_2) \\ & \left( \frac{1.34924 e^{4.33839 hfg \left( -\frac{1}{T_j} + \frac{1}{T_{ref}} \right)} hfg Pref^2 \left( -e^{2.1692 hfg \left( -\frac{1}{T_j} + \frac{1}{T_{ref}} \right)} Pref + P_{tot} \right) Rhj^2}{Rair \left( P_{tot} - e^{2.1692 hfg \left( -\frac{1}{T_j} + \frac{1}{T_{ref}} \right)} Pref Rhj \right)^2 T_j^3} \right. \\ & \frac{1.34924 e^{4.33839 hfg \left( -\frac{1}{T_j} + \frac{1}{T_{ref}} \right)} hfg Pref^2 Rhj}{Rair \left( P_{tot} - e^{2.1692 hfg \left( -\frac{1}{T_j} + \frac{1}{T_{ref}} \right)} Pref Rhj \right) T_j^3} + \\ & \frac{1.34924 e^{2.1692 hfg \left( -\frac{1}{T_j} + \frac{1}{T_{ref}} \right)} hfg Pref \left( -e^{2.1692 hfg \left( -\frac{1}{T_j} + \frac{1}{T_{ref}} \right)} Pref + P_{tot} \right) Rhj}{Rair \left( P_{tot} - e^{2.1692 hfg \left( -\frac{1}{T_j} + \frac{1}{T_{ref}} \right)} Pref Rhj \right) T_j^3} \\ & \left. \frac{0.622 e^{2.1692 hfg \left( -\frac{1}{T_j} + \frac{1}{T_{ref}} \right)} Pref \left( -e^{2.1692 hfg \left( -\frac{1}{T_j} + \frac{1}{T_{ref}} \right)} Pref + P_{tot} \right) Rhj}{Rair \left( P_{tot} - e^{2.1692 hfg \left( -\frac{1}{T_j} + \frac{1}{T_{ref}} \right)} Pref Rhj \right) T_j^2} \right) w_p \Bigg/ \\ & \left( \begin{aligned} & \text{Delt Dif} \left( \frac{0.622 e^{2.1692 hfg \left( -\frac{1}{T_j} + \frac{1}{T_{ref}} \right)} Pref \left( -e^{2.1692 hfg \left( -\frac{1}{T_j} + \frac{1}{T_{ref}} \right)} Pref + P_{tot} \right) Rhj}{Rair \left( P_{tot} - e^{2.1692 hfg \left( -\frac{1}{T_j} + \frac{1}{T_{ref}} \right)} Pref Rhj \right) T_j} \right. \\ & \left. \frac{0.622 e^{2.1692 hfg \left( \frac{1}{T_{ref}} - \frac{1}{T_w} \right)} Pref}{Rair T_w} \right)^2 \end{aligned} \right)
 \end{aligned}
 \end{aligned}$$

**The following is the output for sensitivity coefficient for the surface temperature ( $T_w$ ):**

$$\begin{aligned}
 & - \left( (-T_1 + T_2) \left( \frac{1.34924 e^{2.1692 hfg \left( \frac{1}{T_{ref}} - \frac{1}{T_w} \right)} hfg Pref}{R_{air} T_w^3} + \frac{0.622 e^{2.1692 hfg \left( \frac{1}{T_{ref}} - \frac{1}{T_w} \right)} Pref}{R_{air} T_w^2} \right) w \rho \right) / \\
 & \left( \text{Delt Dif} \left( \frac{0.622 e^{2.1692 hfg \left( -\frac{1}{T_j} + \frac{1}{T_{ref}} \right)} Pref \left( -e^{2.1692 hfg \left( -\frac{1}{T_j} + \frac{1}{T_{ref}} \right)} Pref + P_{tot} \right) Rh_j}{R_{air} \left( P_{tot} - e^{2.1692 hfg \left( -\frac{1}{T_j} + \frac{1}{T_{ref}} \right)} Pref Rh_j \right) T_j} - \right. \right. \\
 & \left. \left. \frac{0.622 e^{2.1692 hfg \left( \frac{1}{T_{ref}} - \frac{1}{T_w} \right)} Pref}{R_{air} T_w} \right)^2 \right)
 \end{aligned}$$

**The following is the output for sensitivity coefficient for the jet slot width (% $Rh_j$ ):**

$$\begin{aligned}
 & - \left( (-T_1 + T_2) \left( \frac{0.622 e^{4.33839 hfg \left( -\frac{1}{T_j} + \frac{1}{T_{ref}} \right)} Pref^2 \left( -e^{2.1692 hfg \left( -\frac{1}{T_j} + \frac{1}{T_{ref}} \right)} Pref + P_{tot} \right) Rh_j}{R_{air} \left( P_{tot} - e^{2.1692 hfg \left( -\frac{1}{T_j} + \frac{1}{T_{ref}} \right)} Pref Rh_j \right)^2 T_j} + \right. \right. \\
 & \left. \left. \frac{0.622 e^{2.1692 hfg \left( -\frac{1}{T_j} + \frac{1}{T_{ref}} \right)} Pref \left( -e^{2.1692 hfg \left( -\frac{1}{T_j} + \frac{1}{T_{ref}} \right)} Pref + P_{tot} \right)}{R_{air} \left( P_{tot} - e^{2.1692 hfg \left( -\frac{1}{T_j} + \frac{1}{T_{ref}} \right)} Pref Rh_j \right) T_j} \right) w \rho \right) / \\
 & \left( \text{Delt Dif} \left( \frac{0.622 e^{2.1692 hfg \left( -\frac{1}{T_j} + \frac{1}{T_{ref}} \right)} Pref \left( -e^{2.1692 hfg \left( -\frac{1}{T_j} + \frac{1}{T_{ref}} \right)} Pref + P_{tot} \right) Rh_j}{R_{air} \left( P_{tot} - e^{2.1692 hfg \left( -\frac{1}{T_j} + \frac{1}{T_{ref}} \right)} Pref Rh_j \right) T_j} - \right. \right. \\
 & \left. \left. \frac{0.622 e^{2.1692 hfg \left( \frac{1}{T_{ref}} - \frac{1}{T_w} \right)} Pref}{R_{air} T_w} \right)^2 \right)
 \end{aligned}$$

**The following is the output for sensitivity coefficient for the jet slot width (w):**

$$\left( (-T_1 + T_2) \rho \right) /$$

$$\left( \text{Delt Dif} \left( \frac{0.622 e^{2.1692 hfg \left( -\frac{1}{T_j} + \frac{1}{T_{ref}} \right)} Pref \left( -e^{2.1692 hfg \left( -\frac{1}{T_j} + \frac{1}{T_{ref}} \right)} Pref + P_{tot} \right) Rh_j}{Rair \left( P_{tot} - e^{2.1692 hfg \left( -\frac{1}{T_j} + \frac{1}{T_{ref}} \right)} Pref Rh_j \right) T_j} \right. \right.$$

$$\left. \left. \frac{0.622 e^{2.1692 hfg \left( \frac{1}{T_{ref}} - \frac{1}{T_w} \right)} Pref}{Rair T_w} \right) \right)$$

**The following is the output for sensitivity coefficient for the Diffusivity (Dif or D):**

$$- \left( (-T_1 + T_2) w \rho \right) /$$

$$\left( \text{Delt Dif}^2 \left( \frac{0.622 e^{2.1692 hfg \left( -\frac{1}{T_j} + \frac{1}{T_{ref}} \right)} Pref \left( -e^{2.1692 hfg \left( -\frac{1}{T_j} + \frac{1}{T_{ref}} \right)} Pref + P_{tot} \right) Rh_j}{Rair \left( P_{tot} - e^{2.1692 hfg \left( -\frac{1}{T_j} + \frac{1}{T_{ref}} \right)} Pref Rh_j \right) T_j} \right. \right.$$

$$\left. \left. \frac{0.622 e^{2.1692 hfg \left( \frac{1}{T_{ref}} - \frac{1}{T_w} \right)} Pref}{Rair T_w} \right) \right)$$

**The following is the output for sensitivity coefficient for the condensate thickness at  $t_1$  (T1):**

$$- (w \rho) /$$

$$\left( \text{Delt Dif} \left( \frac{0.622 e^{2.1692 hfg \left( -\frac{1}{T_j} + \frac{1}{T_{ref}} \right)} Pref \left( -e^{2.1692 hfg \left( -\frac{1}{T_j} + \frac{1}{T_{ref}} \right)} Pref + P_{tot} \right) Rh_j}{Rair \left( P_{tot} - e^{2.1692 hfg \left( -\frac{1}{T_j} + \frac{1}{T_{ref}} \right)} Pref Rh_j \right) T_j} \right. \right.$$

$$\left. \left. \frac{0.622 e^{2.1692 hfg \left( \frac{1}{T_{ref}} - \frac{1}{T_w} \right)} Pref}{Rair T_w} \right) \right)$$

**The following is the output for sensitivity coefficient for the condensate thickness at  $t_3$  (T2):**

$(w\rho) /$

$$\left( \text{Delt Dif} \left( \frac{0.622 e^{2.1692 hfg \left( -\frac{1}{T_j} + \frac{1}{T_{ref}} \right)} Pref \left( -e^{2.1692 hfg \left( -\frac{1}{T_j} + \frac{1}{T_{ref}} \right)} Pref + P_{tot} \right) Rhj}{Rair \left( P_{tot} - e^{2.1692 hfg \left( -\frac{1}{T_j} + \frac{1}{T_{ref}} \right)} Pref Rhj \right) Tj} - \frac{0.622 e^{2.1692 hfg \left( \frac{1}{T_{ref}} - \frac{1}{T_w} \right)} Pref}{Rair Tw} \right) \right)$$

**The following is the output for sensitivity coefficient for the time between condensate thickness measurements (Delt):**

$-((-T1 + T2) w\rho) /$

$$\left( \text{Delt}^2 \text{Dif} \left( \frac{0.622 e^{2.1692 hfg \left( -\frac{1}{T_j} + \frac{1}{T_{ref}} \right)} Pref \left( -e^{2.1692 hfg \left( -\frac{1}{T_j} + \frac{1}{T_{ref}} \right)} Pref + P_{tot} \right) Rhj}{Rair \left( P_{tot} - e^{2.1692 hfg \left( -\frac{1}{T_j} + \frac{1}{T_{ref}} \right)} Pref Rhj \right) Tj} - \frac{0.622 e^{2.1692 hfg \left( \frac{1}{T_{ref}} - \frac{1}{T_w} \right)} Pref}{Rair Tw} \right) \right)$$

**The following is the input of the variable values and the uncertainty associated with each):**

**(\*\* Error estimates for the parameters \*\*)**

**dT2 = .3 / 1000000;**

**dT1 = .3 / 1000000;**

**dDelt = 0.5;**

**dw = 0.0005;**

**dRhj = 0.02;**

**dDif = .0000002;**

**dTw = 0.5;**

**dTj = 0.5;**

**(\*\* Parameter values \*\*)**

**Rair = 0.287;**

**r = 1000;**

**Tref = 293.15;**

**Pref = 2.339;**

**hfg = 2454.1;**

**Dif =  $1.87 * 10^{(-7)} * (Tj + Tw) / 2 - 2.96 * 10^{(-5)}$**

**Tj = 273.15 + 24.6;**

**Tw = 273.15 + 11.1;**

**Rhj = 0.46;**

**w = 0.02;**

**Delt = 10;**

**T2 = 3.90 / 1000000;**

**T1 = 1.98 / 1000000;**

**Ptot = 101;**

**The following is the output for the uncertainty in the Sherwood number and the graphical representation of the result of the calculation:**

**(\*\* Potential Error in Sherwood number calculation \*\*)**

**dSh =**

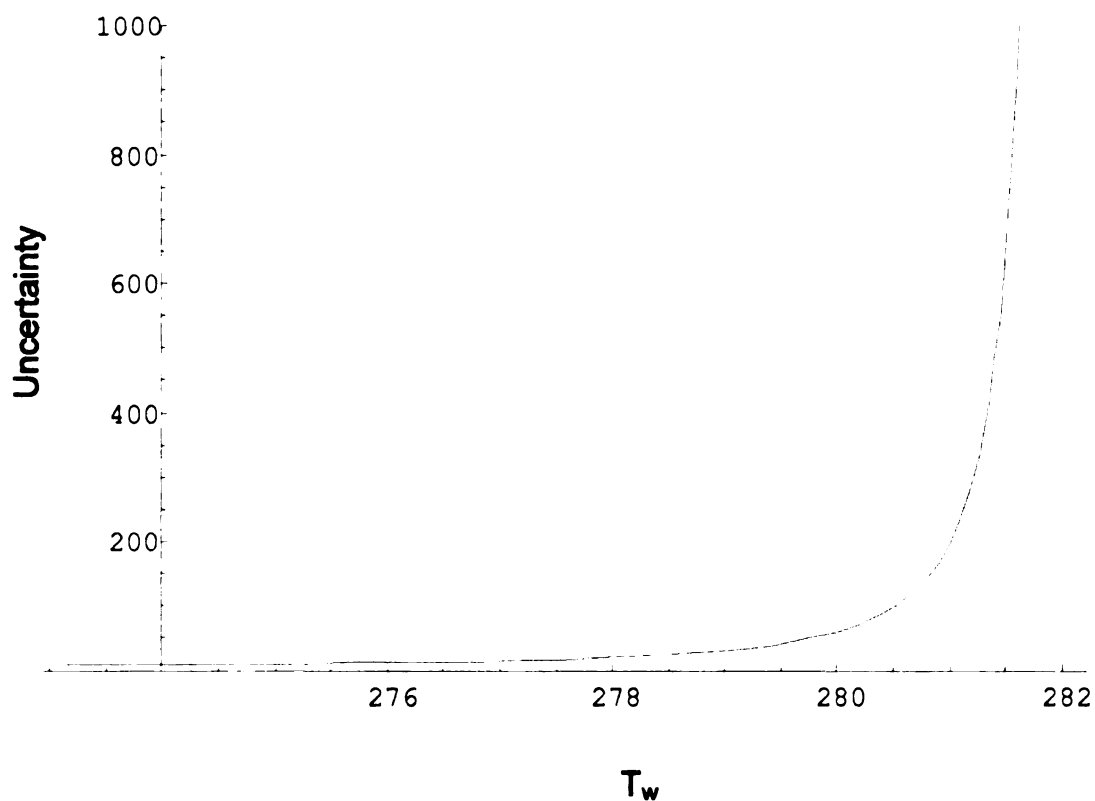
$$((STj * dTj)^2 + (STw * dTw) + (SRhj * dRhj)^2 + (Sw * dw)^2 + (SDif * dDif)^2 + (ST1 * dT1)^2 + (ST2 * dT2)^2 + (SDelt * dDelt)^2)^{0.5}$$

**The equation representing the uncertainty in the Sherwood number can be calculated with:**

$$\left( \frac{5.89824 \times 10^{-25}}{\left( 0.00880709 - \frac{5.06919e^{5323.43 \left( 0.00341122 - \frac{1}{Tw} \right)}}{Tw} \right)^2 (-0.0000296 + 9.35 \times 10^{-8} (295.15 + Tw))^4} + \frac{2.44594 \times 10^{-18}}{\left( 0.00880709 - \frac{5.06919e^{5323.43 \left( 0.00341122 - \frac{1}{Tw} \right)}}{Tw} \right)^4 (-0.0000296 + 9.35 \times 10^{-8} (295.15 + Tw))^2} - \frac{3.6608 \times 10^{-13}}{\left( 0.00880709 - \frac{5.06919e^{5323.43 \left( 0.00341122 - \frac{1}{Tw} \right)}}{Tw} \right)^2 (-0.0000296 + 9.35 \times 10^{-8} (295.15 + Tw))^2} + 9.6 \times 10^{-7} \left( -\frac{26985.5e^{5323.43 \left( 0.00341122 - \frac{1}{Tw} \right)}}{Tw^3} + \frac{5.06919e^{5323.43 \left( 0.00341122 - \frac{1}{Tw} \right)}}{Tw^2} \right) \right)^{0.5}$$



**The graphical representation of the uncertainty in the Sherwood number follows:**



**Note that the variable names utilized in the Mathematica<sup>®</sup> program do not necessarily match the variable names utilized in the remainder of this document. A list of the Mathematica<sup>®</sup> variables and the counterpart in the document is provided in Table F.1 below.**

**Table F.1. Mathematica<sup>®</sup> variable names and corresponding variables in document.**

Mathematica variable name	Standard Variable
Dif	D
hm	$h_m$
Pref	$P_{ref}$
Rhj	$Rh_j$
Delt	$\Delta t$
$\omega_w$	$\omega_w$
Rair	$R_{air}$
Rwater	$R_w$
Tj	$T_j$
Tw	$T_s$
Cj	$C_j$
Cw	$C_s$
T1	$T(t_1)$
T2	$T(t_2)$

## **APPENDIX G**

### **PUBLICATIONS ASSOCIATED WITH THIS WORK**

Hoke, P. B., Wang, Q., and McGrath J. J., AbdulNour, B. S., 1999, *Experimental and Numerical Study of a Condensing Flow in a Developing Wall Jet*, Proceedings of the First International Turbulence and Shear Flow Phenomena Conference, September, pp. 391 - 396.

Hoke, P. B., Kinnen, A. R., McGrath, J. J., AbdulNour, B. S., 2000, *Experimental Measurement and Numerical Prediction of Condensation in a Developing Wall Jet Flow*, 9<sup>th</sup> (Millennium) International Symposium on Flow Visualization 2000, Edinburgh Scotland, pp.134-1 - 134-10.

Hoke, P. B., Loconto, P. R., McGrath, J. J., *Calibration of an Optical Condensate Measurement Technique Utilizing Indirect Headspace Gas Chromatography*, The Journal of Chromatographic Science – Submitted March 2001.

Paul B. Hoke, John J. McGrath and Paul R. Loconto, *Quantitative Analysis by Indirect and Reactive Static Headspace GC: Determination of a Thin Film of Water Deposited on an Aluminum Surface; Calibration Considerations*, American Laboratory, Submitted July 2001.

Other proposed publications:

Hoke, P.B., McGrath, J. J., *Measurement of Condensate Film Thickness on Reflective Surfaces with Infrared Thermography*, Measurement Science and Technology, Proposed submission September 2001.

## **BIBLIOGRAPHY**

## **Bibliography**

- AbdulNour, R. S., Willenborg, K., McGrath, J. J., Foss, J. F., and AbdulNour, B. S., 1997, *Measurements of the Convective Heat Transfer Coefficient for a Two-Dimensional Wall Jet: Uniform Temperature and Uniform Heat Flux Boundary Conditions*, HTD-Vol. 353, Proceedings of the ASME Heat Transfer Division, Volume 3, pp. 109-116.
- AbdulNour, B. S., 1999, *CFD Prediction of Automotive Windshield Defrost Pattern*, Paper No. 1999-01-1203, Society of Automotive Engineering, International Congress & Exposition, Detroit, MI, p. 1-9.
- Akfirat, J. C., 1966, *Transfer of Heat From an Isothermal Flat Plate to a Two-Dimensional Wall Jet*, Proceedings of the Third International Heat Transfer Conference, (2), pp. 274-279.
- Alenezi, G. A., and Abdo, M. S. E., 1991, *Mass-Transfer Measurements Around a Single Cylinder in a Cross Flow at Low Reynolds Numbers*, Chemie Ingenieur Technik, Vol. 63, pp. 381-384.
- Anderson, K.F., Carlson C., and Wells, H., 1996, *Infrared Water-Film Monitor for Hydroponic Systems*. NASA Tech Briefs, Vol. 20, October, No. 10.
- Bearman, G. H., Biswas, A., Chrien, T. G., Green, P., and Green, R. O., 1998, *Optical Remote Detection of Ice on Aircraft Surfaces*, NASA Tech Briefs, NPO19929, Vol. 22, No. 9, pp. i, 1-7.
- Bejan, A., 1995, Convective Heat Transfer, John Wiley and Sons, New York, pp. 46-51, 403-412, 466-477.
- Bradshaw, P. and Gee, M. T., 1960, *Turbulent Wall Jets With and Without an External Stream*, Aero. Res. Council, R&M 3252.
- Çengel, Y. A., and Boles, M. A., 1989, Thermodynamics: An Engineering Approach, McGraw-Hill Inc., New York, pp. 639, 874.
- Chui, Boon Keat, 2000, Personal Communication.

- Cloud, Gary, 1998, Optical Methods of Engineering Analysis, Cambridge University Press, New York, pp. 180, 416.
- Davies, T. W., Patrick, M., and Tanyildizi, V., 1990, *Local Evaporation Rates in the Impingement Zone of a Free Air Jet*, Proc. 18<sup>th</sup> Australasian Chem. Eng. Symp., Auckland, New Zealand, 1(13), pp. 408-414.
- Davies, T. W., Patrick, M. A., Balint, T., Balint, T. S., and Tanyildizi, V., 1991, *Distribution of Local Mass Transfer Rates in Obstructed Duct Flows*, Proc. Symp. On Heat Transfer, IchemE, Nottingham, UK.
- DeBecker, B., Duby, P., Modi, V., West, and A. C., 1995, *Mass-Transfer to a Line Electrode in Presence of a Periodic Fluid-Flow*, Journal of the ElectroChemical Society, Vol. 142, September, pp. 3001-3007.
- Desjardins, M., 2001, Personal communication.
- Eriksson, J. G., Karlsson, R. I., and Persson, J., 1998, *An Experimental Study of a Two-Dimensional Plane Turbulent Wall Jet*, Experiments in Fluids, Vol. 25, pp. 50-60.
- Fedorov, A. G., Viskanta, R. and Mohamad, A. A., 1997, *Turbulent Heat and Mass Transfer in an Asymmetrically Heated, Vertical Parallel-Plate Channel*, International Journal of Heat and Fluid Flow, Vol. 18, No. 3, June, pp. 307-315.
- Förthmann, E., *Über turbulente strahlausbreitung*, Ing. Arch., Vol. 5, 42, 1934.
- General Eastern Instruments, 1999, M2-Plus Dew-point Monitor Operators Manual, Document No. A40212904, Rev. A.00, Massachusetts, p. 89.
- Goldstein, R. J. And Cho, H. H., 1995, *A Review of Mass-Transfer Measurements Using Naphthalene Sublimation*, Experimental Thermal and Fluid Science, Vol. 10, Iss. 4, pp. 416 – 434.
- Goldstein, R. J., 1996, Fluid Mechanics Measurement- 2<sup>nd</sup> Edition, Taylor and Francis, Washington D.C., pp. 120, 141-143.



- Gregory, C. D., (1997). MRI Artifact Gallery [Online], Available <http://chickscope.beckman.uiuc.edu/roosts/carl/artifacts.html> (December 21, 2000).
- Hassan, M. B., Petitjean, C. Deffieux, J. C. and P. Gilotte, 1999, *Windshield Defogging Simulation with Comparison to Test Data*, SAE 1999-01-1202 International Congress & Exposition, March 1999, Detroit, MI, USA, Session: Climate Control Systems (Part C&D).
- Ho, C.-M., and Huerre, P., *Perturbed Free Shear Layers*, Annual Review of Fluid Mechanics, Vol. 16, pp. 365-424.
- Hoke, P. B., 1998, *Experimental Measurement of the Slit Response Function and Corrected Thermographic Measurements*, Masters Thesis, Michigan State University, p. 43
- Hoke, P. B., Qingtian, W., McGrath, J. J., AbdulNour, B. S., 1999, *Experimental and Numerical Study of a Condensing Flow in a Developing Wall Jet*, Turbulent Shear Flow Phenomena –1 Conference, Santa Barbara CA, pp. 393-395
- Hoke, P.B., Kinnen, A. R., McGrath, J. J., AbdulNour, B. S., 2000, *Experimental Measurement and Numerical Prediction of Condensation in a Developing Wall Jet Flow*, 9<sup>th</sup> International Symposium on Flow Visualization 2000, Edinburgh Scotland, pp. 134-1 – 134-11.
- Hsiao, F., -B., and Sheu, S. -S., 1996, *Experimental Studies on Flow Transition of a Plane Wall Jet*, Aeronautical Journal, November, Vol. 100, pp.373-380.
- Incorpera, F. P., and Dewitt, D. P., 1990, Fundamentals of Heat and Mass Transfer, 3<sup>rd</sup> Edition, John Wiley and Sons, New York, pp. 353-367, 608-615, 872.
- Incorpera, F. P., and Dewitt, D. P., 1996, Fundamentals of Heat and Mass Transfer, 4<sup>th</sup> Edition, John Wiley and Sons, New York, pp. 320-322, 665-666.
- Inframetrics, Inc., 1988, *Model 600L Operators Manual, Document #05250-200 REV C*, Massachusetts, pp. A1-A12.



Kestin, J., Maeder, P. F., Wang, H. E., 1961, *Influence of Turbulence on the Transfer of Heat From Plates With and Without a Pressure Gradient*, International Journal of Heat and Mass Transfer, Vol. 3, pp. 133-154.

Kinnen, A., 2000, *Experimental Investigation of Condensation for Small Concentration Differences and Short Times*, Studienarbeit, Rheinisch-Westfälische Technische Hochschule, Aachen Germany, pp. 23-38.

Launder, B. E. and Rodi, W., 1981, *The Turbulent Wall Jet*, Progress in Aerospace Science, Vol. 19, Pergamon Press, pp. 81-128.

Legay-Desesquelles, F., and Prunet-Foch, B., 1986, *Heat and Mass Transfer with Condensation in Laminar and Turbulent Boundary Layers along a Flat Plate*, International Journal of Heat and Mass Transfer, Vol. 29, No. 1, pp. 95-105.

Loconto, P. R., Pan, Y. L., Voice, T. C., 1996, *Determination of Trace Water in Soils by Automated Indirect Headspace Gas Chromatography*. LC-GC-Magazine of Separation Science, Vol. 14, Issue 2, pp. 128-132.

Loeper, J. and R. Grob, 1988, *Indirect Method for the Determination of Water Using Headspace Gas Chromatography*, Journal of Chromatography, 1988, 457, 247-256.

Mabuchi, I., and Kumada M., 1972, *Studies on Heat Transfer to Turbulent Jets with Adjacent Boundaries*, Bulletin of the JSME, Vol. 15, no. 88, pp. 1236-1245.

Mao, Y., Besant, R. W., and Rexkallah, K. S., 1992, *Measurement and Correlations of Frost Properties with Air Flow Over a Flat Plate*, ASHRAE Transactions, 98(2).

Matuszkiewicz, A. and Vernier, Ph., 1991, *Two-Phase Structure of the Condensation Boundary Layer with a Non-Condensing Gas and Liquid Droplets*, International Journal of Multiphase Flow, Vol. 17, No. 2, pp. 213-225.

Modest, M. F., 1993, Radiative Heat Transfer, McGraw-Hill, New York, pp.442.



- Moffet, R. J., 1988, *Describing the Uncertainties in Experimental Results*, Experimental Thermal and Fluid Science, No. 1, pp. 3-17.
- Morel, T., 1977, *Design of Two-Dimensional Wind Tunnel Contractions*, Journal of Fluids Engineering, Vol. 99, pp. 371-378.
- Neter, J., Wasserman, W., and Whitmore, G. A., 1992, Applied Statistics, Allyn and Bacon, Boston, pp. 269-271.
- Noller, C., 1966, Chemistry of Organic Compounds, pp. 170-172.
- Noui-Mehidi, M. N., Salem, A., Legentilhomme, P., and Legrand, J., 1999, *Overall Mass Transfer in the Swirling Flow Induced by a Tangential Inlet Between Coaxial Cones*, Journal of Applied Electrochemistry, Vol. 29, November, pp. 1277-1284.
- Patel, R. P., 1962, *Self-preserving, Two-dimensional Turbulent Jets and Wall Jets in a Moving Stream*, Masters of Engineering Thesis, Department of Mech. Eng., McGill University, Montreal.
- Pekdemir, T., 1994, *Convective Mass Transfer from Stationary and Rotating Cylinders in a Jet Flow*, Ph.D. Thesis, No. DX185786, Exeter University, UK, pp. 24, 39, 49, 134-140, 150, 157-160.
- Pekdemir, T., and Davies, T. W., 1999, *Establishment of a new mass (heat) transfer measurement technique and its validation*, Experimental Heat Transfer, Vol. 12 (1): pp. 33-51.
- Peters, A. R., 1972, *Interior Window Fogging - An Analysis of the Parameters Involved*, Paper No. 720503, Society of Automotive Engineers, National Automotive Engineering Meeting, Detroit, pp. 1-4.
- Schlesinger, M., De Kee, D. and M. N. Godo, 1986, *Apparatus for Film-thickness Measurements of Postwithdrawal Drainage*, Review of Scientific Instruments, Vol. 57 (10), pp. 2535-2537.
- Siegel, R. and Howell, J. R., 1992, Thermal Radiation Heat Transfer, Hemisphere Publishing Corp. Washington, p. 176.



**Skoog, D. A. and Leary, J. J., 1992, Principles of Instrument Analysis, Fourth Edition, Saunders College Publishing, New York, p. 610.**

**Society of Automotive Engineers, 2000, SAE Handbook, Society of Automotive Engineers, Pennsylvania, Vol. 3, pp. 34.19 - 34.26.**

**Tailland, A., 1967, "Contribution à l'étude d'un jet plan dirigé tangentiellement à une paroi plane", Thèse de Docteur des Sciences, Univ. Claude Bernard, Lyon.**

**Tennekes, H., and Lumley, J. L., 1994, A First Course In Turbulence, The MIT Press, Massachusetts, pp. 115.**

**Thole, K. A., 1992, *High freestream turbulence effects on the transport of heat and momentum*, Ph.D. Dissertation, U.of Texas at Austin, pp. 50-61.**

**TSI Incorporated, 1997, IFA 300 Constant Temperature Anemometer System, Instruction Manual, Minnesota, pp. 1-1, 7-19**

**Utton, D. B., and Sheppard, M. A., 1985, *The Determination of Convective Heat Transfer Using a New Optical Technique*, Proc. Int. Conf. For Heat and Mass Transfer, Hemisphere, Washington DC. Vol.18, pp. 155-166**

**Zhao, W., and Trass, O., 1997, *Electrochemical Mass Transfer Measurements in Rough Surface Pipe Flow: Geometrically Similar V-shaped Grooves*, International Journal of Heat and Mass Transfer, Vol. 40, no. 12, pp. 2785-2797.**



MICHIGAN STATE LIBRARIES



3 1293 02177 3985